

**Investigation of the Dislocation Activity and Texture
Development in Magnesium Alloy Sheets Containing
Zinc, Neodymium, and Calcium**

Doctoral Thesis

(Dissertation)

to be awarded the degree

Doctor of Engineering (Dr.-Ing.)

submitted by

Changwan Ha

from Daegu / Republic of Korea

approved by the

Faculty of Natural and Materials Science

Clausthal University of Technology

Date of oral examination

09. July 2021

Dean

Prof. Dr. -Ing. habil. Joachim Deubener

Chairperson of the Board of Examiners

Supervising tutor

apl. Prof. Dr. rer. nat. Dr. -Ing. habil. Heinz-Günter Brokmeier

Reviewer

Prof. Dr. -Ing. habil. Karl Ulrich Kainer

Acknowledgments

The work was financially supported by Deutsche Forschungsgemeinschaft (German Research Foundation) through project No. Grant. BO 2461/4-1, Yi 103/2-1, and BR 961/7-1, and carried out from June 2015 to June 2019. This dissertation has been submitted in partial fulfillment of the requirements for a doctoral degree in the Faculty of Natural and Materials Science of Clausthal University of Technology in Germany.

The work presented in this dissertation has been done in a fruitful collaboration with the department of the TEXMAT at the Institute of Materials Science and Engineering (IWW in German), Clausthal University of Technology. I acknowledge that the beamtime is sponsored at P07B (PETRA III of DESY at Hamburg in Germany) for X-ray diffraction experiments at a synchrotron.

First of all, I wish to thank my supervisors, Dr. Sangbong Yi and Dr. Jan Bohlen, for inspiring, active guidance and support during my study and Dr. Dietmar Letzig for providing me an excellent opportunity to study at the Magnesium Innovation Centre (MagIC) of Helmholtz-Zentrum Geesthacht.

My special thanks go to Prof. Dr. Karl Ulrich Kainer and Prof. Dr. Heinz-Günter Brokmeier for their generous support and guidance. I also thank all my colleagues and technicians at the department of Wrought Magnesium Alloys (WZW in German), MagIC. This dissertation would not have been possible without all of your supports. I am also grateful to Prof. Dr. No-Jin Park for giving me the kind encouragement to graduate in Germany.

Last but not least, I am heartily thankful to my family and persons close to my heart for their kindness, help, support, and encouragement. Without all of you, I could not have come so far. Thank you once again for everything you have done.

Abstract

This work investigates the interrelationship among the crystallographic texture, microstructure, and deformation mechanisms, especially dislocation slip activities, in the Mg alloys accompanying the different texture formations after thermomechanical treatments. The rare-earth (RE) elements are generally known as a tailored element to texture modifying in Mg alloys. The addition of Zn combined with the RE elements exhibits a more pronounced texture modification. The Ca is regarded as a promising element that could partially replace RE elements. It has been usually noted that various recrystallization mechanisms ascribe to the texture weakening in the Mg alloys. The various recrystallization mechanisms require nucleation with grain rotation towards random orientations, which are relevantly correlated to the deformation mechanisms. A systematic investigation is emphasized to understand the influence of alloying elements, the active dislocation slip activities, and their contribution to the microstructure on the texture development based on the fact that the texture reflects the deformation mechanisms.

In this work, the Mg alloys were successfully investigated by using *in-situ* experiments at a synchrotron for tracking texture development and change of diffraction patterns under mechanical testing at different temperatures. The obtained results were evaluated using convolutional multiple whole profiles (CMWP) analysis and electron backscattered diffraction (EBSD) measurement in terms of texture development, dislocation slip activities, and microstructure evaluations. The mutual influences between active deformation modes and recrystallization behavior at ambient and elevated temperatures were discussed.

The higher activations of non-basal $\langle a \rangle$ and pyramidal $\langle c+a \rangle$ dislocations in the Nd or Ca containing Mg alloys compared to the Mg-Zn alloy were found in the CMWP analysis. The former is enhanced by the addition of Zn combined with Nd or Ca. In-grain misorientation axes (IGMA) distributions obtained from the EBSD measurement confirms that the predominant prismatic $\langle a \rangle$ slip contributes to the higher activations of non-basal $\langle a \rangle$ dislocation. The texture evolution shows an obvious feature for all examined sheets, which is a broadening of the basal pole perpendicular to the loading direction and a strengthening of the $\langle 10\bar{1}0 \rangle$ pole at the loading direction. The Zn addition in combination with the Nd or Ca shows a pronounced evolution of texture, compared to a sole addition of Nd or Ca. The Zn addition without Nd or Ca shows a less pronounced texture development.

At elevated temperatures, the enhanced activation of non-basal $\langle a \rangle$ dislocations is observed in the ZK10 deformed at 100°C. The serrated grain boundaries and fine grains at the grain boundaries, i.e. the onset of dynamic recrystallization, are observed in the ZK10 deformed at 200°C. In contrast, the uniform deformation and the retardation of the thermally activated processes, e.g. dynamic recovery and dynamic recrystallization, are observed in the other alloys. This retardation is more pronounced with the simultaneous addition of Zn with Nd or Ca.

Zusammenfassung

In dieser Arbeit wurde der Zusammenhang zwischen der Textur, der Mikrostruktur und den Verformungsmechanismen (insbesondere der Aktivität der Versetzungsgleitung) von Mg-Legierungen untersucht, die nach thermomechanischen Behandlungen zu unterschiedlichen Texturentwicklungen führt. Seltene Erdelemente (SE) sind allgemein als geeignete Elemente für eine Texturmodifizierung in Mg-Legierungen bekannt. Die Zugabe von Zn in Kombination mit den SE-Elementen zeigt eine ausgeprägte Texturmodifikation. Das Ca ist ein vielversprechendes Element, das RE-Elemente teilweise ersetzen könnte. Als Grund für die Texturabschwächung werden normalerweise verschiedene Rekristallisations-mechanismen benannt. Diese verschiedenen Rekristallisationsmechanismen erfordern eine Keimbildung mit Kornrotation in zufällige Ausrichtungen, welche in Beziehung zu den Verformungsmechanismen stehen. Es wurde eine systematische Untersuchung durchgeführt, um den Einfluss der Legierungselemente, der aktiven Verformungsmodi und deren Beitrag auf die Mikrostruktur- und Texturentwicklung zu verstehen, basierend auf der Tatsache, dass die Textur die Aktivität der Verformungsmechanismen widerspiegelt.

Die Mg-Legierungen wurden in dieser Arbeit erfolgreich unter Verwendung von *In-situ* Experimenten am Synchrotron untersucht, um die Texturentwicklung und die Veränderung der Diffraktionsdiagramme unter mechanischen Tests bei verschiedenen Temperaturen zu verfolgen. Die erhaltenen Messergebnisse wurden unter Verwendung einer CMWP-Analyse und von EBSD-Messungen im Hinblick auf Texturentwicklung, Aktivität der Verformungsmodi und Mikrostrukturbewertungen ausgewertet. Die gegenseitigen Einflüsse zwischen aktiven Verformungsmodi und dem Rekristallisationsverhalten bei Umgebungs- und erhöhter Temperaturen wurden diskutiert.

Die CMWP Analyse zeigte, dass in den Nd- oder Ca-haltigen Mg Legierungen eine höhere Aktivierung von nicht-basal $\langle a \rangle$ und pyramidal $\langle c+a \rangle$ Versetzung als in der Mg-Zn Legierung stattfindet. Erstere wird durch Zugabe von Zn in Kombination mit Nd oder Ca verstärkt. IGMA-Verteilungen, die aus den EBSD-Messungen gewonnen wurden, bestätigen, dass die dominierende prismatische $\langle a \rangle$ Gleitung zur höheren Aktivierung der nicht-basal $\langle a \rangle$ Versetzung beiträgt. Die Texturentwicklung zeigt ein offensichtliches Charakteristikum für alle untersuchten Bleche, nämlich eine Verbreiterung des basalen Pols senkrecht zur Verformungsrichtung und eine Verstärkung des $\langle 10\bar{1}0 \rangle$ Pols in Verformungsrichtung. Die Zn-Zugabe in Kombination mit Nd oder Ca zeigt eine ausgeprägtere Texturentwicklung im Vergleich zu einer alleinigen Zugabe von Nd oder Ca. Die Zugabe von Zn ohne Nd oder Ca zeigt eine weniger ausgeprägte Texturentwicklung.

Bei erhöhten Temperaturen wird bei dem bei 100°C deformierten ZK10 eine verstärkte Aktivierung nicht-basaler $\langle a \rangle$ Versetzungen beobachtet. Gewölbte Korngrenzen und feinere Körner an den Korngrenzen, also der Beginn der dynamischen Rekristallisation, werden bei dem bei 200°C verformten ZK10 beobachtet. Im Gegensatz dazu werden die gleichmäßige Verformung und die Verzögerung der thermisch aktivierten Prozesse, z.B. eine dynamische Erholung und eine dynamische Rekristallisation, in den anderen Legierungen beobachtet. Diese Verzögerung ist durch die Zugabe von Zn mit Nd oder Ca stärker ausgeprägt.

Contents

1 Introduction and aims	1
1.1 Introduction	1
1.2 Aims	3
2 Theoretical background	5
2.1 Crystallography in magnesium	5
2.2 Deformation mechanisms in Mg alloys	6
2.2.1 Dislocation slip in Mg alloys	6
2.2.2 Deformation twin	10
2.3 Texture development in Mg alloys	12
2.3.1 General description about texture	12
2.3.2 Texture development in HCP metals, especially in Mg alloys	14
3 Dislocation and texture evaluations with synchrotron radiation	18
3.1 Introduction of synchrotron radiation	19
3.2 Line profile analysis using X-ray diffraction	20
3.2.1 Convolutional Multiple Whole Profile (CMWP) fitting method	23
3.3 Texture measurement using synchrotron radiation	28
4 Experimental materials and methods	31
4.1 Experimental materials	31
4.2 <i>In-situ</i> experiments under tensile loading	32
4.2.1 Tensile tests	32
4.2.2 <i>In-situ</i> texture measurement using synchrotron radiation	35
4.2.3 Line profile analysis using the CMWP fitting procedure	35
4.3 Microstructure and EBSD observations	36
4.3.1 IGMA analysis	37

5 Results and discussion	39
5.1 Initial microstructure and texture for examined sheets.....	39
5.2 Texture development and dislocation activity in different Mg sheets	42
5.2.1 Results: <i>in-situ</i> texture measurement under tension	43
5.2.2 Results: variation of dislocation activities.....	49
5.2.3 Discussion: deformation modes for texture development	58
5.2.4 Discussion: effect of initial texture on dislocation activity	62
5.2.5 Discussion: effect of alloying elements on dislocation activity	63
5.3 Dislocation activities at elevated temperature.....	65
5.3.1 Results: <i>in-situ</i> texture measurements under tensile loading.....	65
5.3.2 Results: dislocation activities at elevated temperatures	71
5.3.3 Discussion: effect of deformation temperature on dislocation activity .	82
6 Summary and outlook	93
6.1 General remarks	93
6.2 Outlook	94
References.....	96
Appendix	103
List of symbols and abbreviations.....	103
Stress-strain curves acquired from the two <i>in-situ</i> experiments at RT	107
Phase diagrams	108
Dislocation activities obtained from the CMWP analysis.....	111

1 Introduction and aims

1.1 Introduction

Magnesium (Mg) and its alloys, the lightest metallic engineering materials, are attractive materials to the transportation industry for high performance and environmentally friendly materials. They have great potential to fulfill the requirements of many applications in the automobile and aerospace industries [1, 2]. For this reason, Mg research is still extensively in the focus of interest due to the low density and high damping capacity of the materials. The Mg is often compared to aluminum (Al) with low density ($\rho_{Al} = 2.7g \cdot cm^{-3}$ and $\rho_{Mg} = 1.7g \cdot cm^{-3}$). The Al is already successfully used in the industry, while the Mg is still somewhat lacking competitiveness due to higher production costs and poor formability at ambient or relatively low temperatures [2-4].

The poor formability of the Mg is mainly due to a hexagonal close-packed (HCP) lattice with the insufficiency of independent deformation modes [5] with developing the specific crystallographic textures during the thermomechanical processes such as rolling, extrusion, or annealing [6-9]. The distinct strain anisotropy with preferred specific texture development, which is basal planes orientated parallel to the sheet plane, is also one of the mechanical behavior issues. The most effective way to overcome these issues is texture modification that has been studied with intense attention in the last decades. It was reported that the texture randomization or modification significantly influences mechanical properties and formability in numerous researches.

It is generally known that alloying additions of rare earth (RE) elements such as yttrium (Y), cerium (Ce), lanthanum (La), neodymium (Nd), or gadolinium (Gd) into Mg alloy can contribute to modify the texture, which is developed by basal planes spread out from the normal direction (ND) towards rolling or transverse direction (RD or TD) [10-15]. Other elements with larger atomic size, such as Ca, are also reported for texture modification [16-18]. A sole addition of RE or Ca element into Mg as a binary Mg alloy mostly shows a weak texture with basal planes spread towards the RD, compared to classical addition of alloying elements such as Al, Zn, or Mn, which shows the basal planes parallel to the sheet plane, i.e. typical basal type texture. On the other hand, the addition of RE or Ca combined with Zn into Mg leads to the specific formation of texture

with basal pole spread towards the TD, differing from the sole addition of RE or Ca [16, 17, 19]. Other approaches for texture modification are to control processing parameters, e.g. changed thickness reduction, temperature, and time [20].

Such texture modification plays an important role in improving the formability of Mg alloys to some extent [6, 8, 10, 11, 17, 20-24]. In other words, the formability of Mg alloys is laid on the fact that the active deformation systems are strongly dependent on the texture. Furthermore, the deformation texture development is associated with the activation of specific deformation systems [14, 25]. Agnew et al. demonstrated that the basal pole split toward the RD is related to the activation of pyramidal $\langle c+a \rangle$ slip during deformation [6, 26]. It was reported that the basal pole broadening toward the TD is associated with different twins, causing changes of orientation in the matrix grains to the corresponding orientations [22, 27], as well as with the active prismatic $\langle a \rangle$ slip in ternary Mg-Zn-RE alloys [28-30].

In addition to the deformation texture, the texture modification is more complex as it develops due to the various influences of static and/or dynamic recrystallization mechanisms, e.g., by particle-simulated nucleation (PSN) [10, 31], grain nucleation in shear bands [13, 32], solute drag or boundary pinning [11, 33, 34]. Recrystallization mechanisms are likely to lead to texture modification by new grain nucleation in the shear bands and around the particles or by restricting grain growth at the precipitates. However, these recrystallization mechanisms on the texture modification depend on the massive deformation of the samples by operating deformation mechanisms associated with changing grain rotations during the processing, such as the rolling or extrusion of materials. In this context, a more extended knowledge is still necessary for particular deformation mechanisms and their interaction with active softening mechanisms, i.e. recovery and recrystallization, in dictating texture modification.

In this work, advanced experimental techniques were applied to investigate tracking the texture development and the dislocation structure in real-time under tensile tests at different temperatures in the Mg alloys. Hard X-ray diffraction at a synchrotron was applied by which the texture can be measured in situ during deformation. The synchrotron radiation with high brilliance provides a possibility to obtain extensive Debye-Scherrer rings or complete pole figures in a relatively short exposure time due to the applied transmission geometry by employing an area detector. Thus, the *in-situ* diffraction

experiment using synchrotron radiation ensures to track continuous texture development and the change of diffraction peak profiles of a selected sample volume without deterioration of the experimental result. Furthermore, an analysis using electron backscattered diffraction (EBSD) provides important information about the microstructure accompanying the active deformation and recrystallization mechanisms. The active deformation mechanisms within the deformed grains are evaluated based on an in-grain misorientation axes (IGMA) analysis, which allows determining the activity of dominating slip mechanisms via the preferable axis (Taylor axis) of rotation between neighbored measured points in EBSD measurement. The obtained data sets of various experimental analysis methods will be used for investigating interrelationship among the texture development, the predominant deformation mechanisms, and the recrystallization behaviors at applied experimental conditions.

1.2 Aims

The main aim of this work is a systematic investigation of the interrelationship among the active deformation mechanisms, especially dislocation slip activity, and the texture development in real-time during deformation in Mg alloys. Since the texture development reflects the deformation history, including the deformation mechanisms activated during deformation, the investigation of the texture development in real-time under applied load can provide meaningful information in different Mg alloys. Concurrent with the investigation of the texture development, the analyses of convolutional multiple whole profile (CMWP) and in-grain misorientation axes (IGMA) can provide important information on the deformation modes. To investigate the dislocation activities resulting in different texture developments in dependence on the alloy elements, binary Mg-Nd and Mg-Ca alloys and their counterpart ternary Mg alloys combined with Zn were designed in this work. For attaining systematically to the extensive goal, the general topic was addressed as follows:

- The advanced diffraction technique using hard X-rays at synchrotron was applied to track the *in-situ* texture evolution and diffraction peak (line) profiles experimentally during the deformation and to compare the differences between the Mg alloys.

- Based on the experimental results from CMWP and IGMA analyses, the relationship between the texture evolution and dislocation slip activity in different Mg alloys was interpreted with respect to the influences of initial textures and alloying elements.
- The influence of deformation temperature on the active deformation mechanisms concerning the thermally activated procedures, like dynamic recovery and dynamic recrystallization, is investigated with the texture and microstructure evolutions during deformation at elevated temperatures. The experimental results at different temperatures were interpreted in terms of the interrelationship among the deformation texture, dislocation slip activities, and recrystallization behaviors.

The knowledge obtained from this work provides an understanding of the deformation and recrystallization mechanisms that contribute to the texture evolutions in Mg alloys. Moreover, this work can assist in optimizing texture modification, microstructure development, and mechanical properties as well as the formability improvement of Mg alloys for industrial applications.

2 Theoretical background

2.1 Crystallography in magnesium

Magnesium (Mg) has the hexagonal close-packed (HCP) structure with lattice parameters, $a = 0.321$ nm and $c = 0.521$ nm, and corresponding interaxial angles $\alpha = \beta = 90^\circ$ and $\gamma = 120^\circ$ as shown in Fig. 2.1.1 (a). The lattice parameter, a , consists of the three equal long axes, a_1 , a_2 , and a_3 , parallel to the basal plane marked in Fig. 2.1.1 (a), and c -axis, which is perpendicular to the basal plane. In the four-axis coordinate system, the directions and planes in the HCP structure are commonly notated by the Miller-Bravais index [35]. Miller-Bravais notation is based on the unit vectors, a_1 , a_2 , and a_3 and c . Crystallographic directions and planes are respectively given by $[u\ v\ t\ w]$ and $(h\ k\ i\ l)$, where i is $-(h + k)$. An atomic packing factor and a coordination number of the HCP structure are the same values with a face-centered cubic (FCC) structure of 0.74 and 12, respectively. However, FCC and HCP structures are distinguished in the stacking sequence of the close-packed plane. The FCC has a sequence of ‘ABCABC...’, but the HCP has ‘ABABAB...’ [36]. The atomic position in the HCP structure is shown in Fig. 2.1.1 (b).

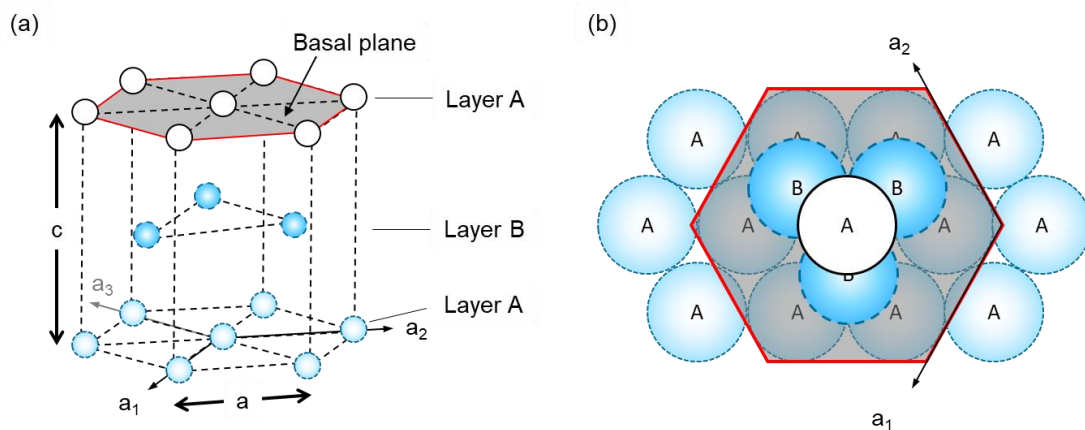


Fig. 2.1.1 (a) Hexagonal close-packed crystallographic structure and (b) atomic position in a projection of the basal plane [37]

2.2 Deformation mechanisms in Mg alloys

The basic mechanisms of plastic deformation in metallic materials are the deformation slip systems and deformation twin. The Mg having the HCP structure exhibits a relatively less number of deformation slip systems activated at ambient temperature than materials having the cubic structures. The basal $\langle a \rangle$ slip, an easy slip system with a lower value of the critical resolved shear stress (CRSS), provides only two independent slip systems. The basal $\langle a \rangle$ slip cannot accommodate the deformation along the c -axis of the HCP structure. For this reason, the homogeneous plastic deformation of the Mg and its alloys requires additional deformation slip systems and/or their combinations with the deformation twin. It has generally presented that prismatic $\langle a \rangle$, pyramidal $\langle a \rangle$, and pyramidal $\langle c+a \rangle$ slip systems are additional dislocation slip systems. However, the activation of other slip systems requires a higher value of the CRSS than basal $\langle a \rangle$ slip.

2.2.1 Dislocation slip in Mg alloys

The dislocation slip is realized by the dislocation motions. The Burgers vector, \vec{b} , represents the magnitude and direction of slip. One slip system generally consists of the close-packed plane and close-packed direction. When the external stress applies to the material, the slip systems are acted by a resolved shear stress (RSS) in the slip plane along the slip direction. The RSS is closely related to the relationship between the loading direction and grain orientation applied on the slip plane for activating the slip systems. The grain orientation depends on the Schmid factor associated with the relationship between angles among the slip direction, the normal direction of the slip plane, and the loading direction. Fig. 2.2.1 describes the geometric relationship between the RSS and Schmid factor, as following by

$$\tau (RSS) = \frac{F}{S_0} \cdot m = \sigma \cdot m = \sigma \cdot \cos \xi \cdot \cos \emptyset \quad (eq.2.2.1)$$

where τ is the RSS, σ is the external stress, S_0 is the cross-sectional area, ξ_S is the angle between the slip direction and the loading direction, ϕ is the angle between the normal axis of the slip plane and the applied load direction. The Schmid factor, m , is given by $\cos \xi \cdot \cos \phi$. The ideal slip direction for activation of the slip system is when $\xi_S = \phi = 45^\circ$. Hence, the activation of dislocation slip systems certainly depends on the Schmid factor and the CRSS, τ_c , on the slip plane along the slip direction, i.e. when the RSS exceeds a critical value.

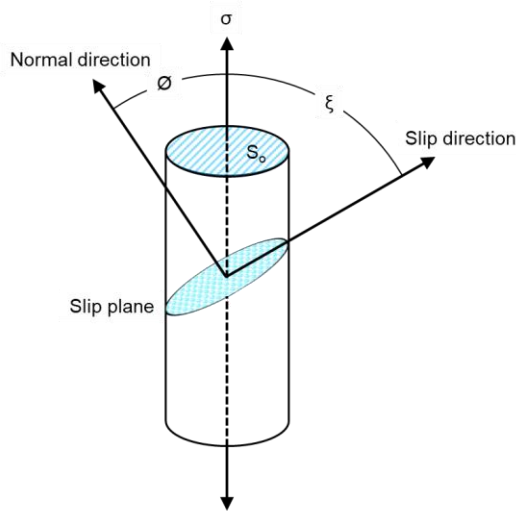


Fig. 2.2.1 Schematic illustration for the relationship between the resolved shear stress (RSS) and the Schmid factor in a single crystal [37, 38]

The CRSS for activating the slip systems, especially non-basal slip systems, usually keeps constant during the plastic deformation, i.e. the Schmid factor, m , does not change the CRSS [39]. However, the deformation temperature strongly varies the CRSS [40, 41]. Barnett et al. [42] reported that the CRSS for the basal, prismatic, and pyramidal slip systems in the Mg alloys depends on the deformation temperatures. Its dependence is shown in Fig. 2.2.2. The CRSS for the basal slip system does not change with increasing deformation temperature, while the CRSS for the non-basal slip systems significantly decreases. In addition to the deformation temperature, it is reported that the alloying elements such as Al, Zn, Li, and, Y as well as their combination, such as Zn-Y, significantly affect to decrease of the CRSS for non-basal slip systems [6, 21, 40, 43].

The slip plane is continuously changed by fixed external deformation axes during plastic deformation, thereby occurring the crystal rotation, i.e. changed Schmid factor, as shown

in Fig. 2.2.3. The Schmid factor by rotating the slip planes influences the texture development [44, 45], consequently correlating to slip system activations. Accordingly, it is a meaningful point to adjust the changes of the Schmid factor and the CRSS, affecting the deformation mechanisms in the Mg and its alloys.

It is essential to combine deformation slip systems and/or deformation twin due to the geometrical requirement of the 5 independent slip modes in polycrystalline deformation (so-called the von Mises criterion) in order to realize homogeneous deformation without cracks [46]. The deformation slip systems in the HCP structure, including the Mg, are

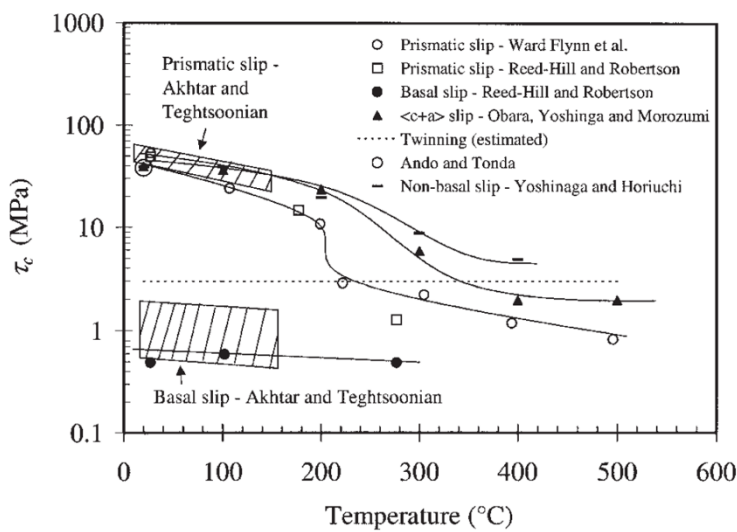


Fig. 2.2.2 Influence of deformation temperature on the critical resolved shear stress (CRSS) according to the model determined from experiments in [42]

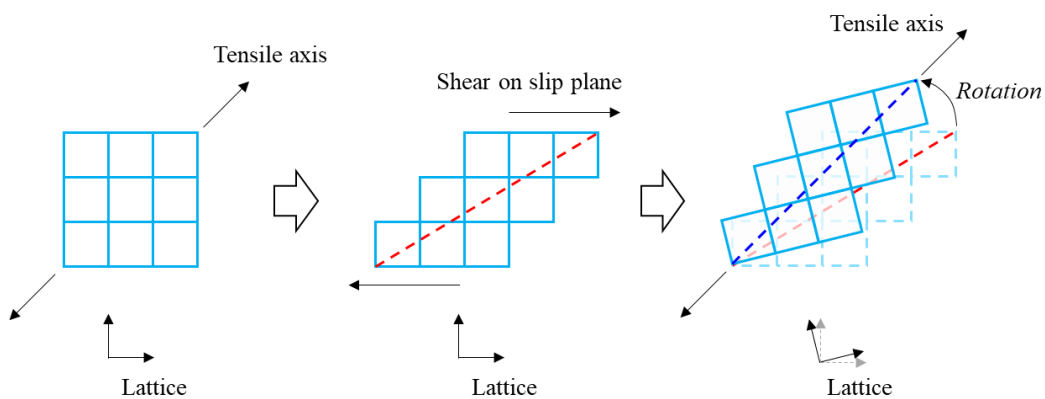


Fig. 2.2.3 Schematic illustration of the slip plane changing via crystal rotation under uniaxial tensile deformation [25]

summarized in Table 2.2.1 and are schematically illustrated in Fig. 2.2.4 [38, 47]. Because of the energetic point of view in perfect or partial dislocations depending on the planar density, the $\langle a \rangle$ dislocations should be the most favorable. The activation of the three types of the $\langle a \rangle$ dislocations can assist in fulfilling the von Mises criterion [46]. However, those activations cannot still accommodate the deformation along the c -axis of the HCP structure. The deformation along the c -axis requires the other deformation modes. The twin can be easily activated due to having a lower CRSS than the basal $\langle a \rangle$ slip about deformation along the c -axis. Another possibility is the pyramidal $\langle c+a \rangle$ slip, but this slip is known to be difficultly activated due to a relatively high CRSS, compared to the basal $\langle a \rangle$ slip [48, 49]. The CRSS for the basal $\langle a \rangle$ slip is reported as 0.5 ~ 1.2 MPa [50], and that for the non-basal slip systems is reported to be high about 4 ~ 12 times [6, 21]. The pyramidal $\langle c+a \rangle$ slip is observed to be activated, which is directly or indirectly reported in earlier studies investigated via transmission electron microscopy (TEM) investigations [51, 52], simulation works [6, 53], or X-ray evaluation [28, 54-56]. They suggested that the pyramidal $\langle c+a \rangle$ dislocation slip is activated by adjusting the CRSS value with changed alloy elements and compositions in the past. Recently, It has been reported that the addition of alloying elements modifies the stacking fault energy (SFE) on the basal and pyramidal planes, thereby, associating with the probability of the increasing pyramidal $\langle c+a \rangle$ dislocations [51, 52]. In this context, the importance of the pyramidal $\langle c+a \rangle$ slip system and/or other slip systems, e.g. the non-basal $\langle a \rangle$ slip and deformation twin are emphasized for accommodating deformation.

Table 2.2.1 Deformation slip systems in HCP including Mg and its alloys [47]

Slip systems	Slip direction	Slip plane	Crystallographic elements	Number of independent modes
Basal $\langle a \rangle$	$\langle 11\bar{2}0 \rangle$	(0001)	(0001) $\langle 11\bar{2}0 \rangle$	2
Prismatic $\langle a \rangle$	$\langle 11\bar{2}0 \rangle$	$\{10\bar{1}0\}$	$\{10\bar{1}0\}\langle 11\bar{2}0 \rangle$	2
Pyramidal $\langle a \rangle$	$\langle 11\bar{2}0 \rangle$	$\{11\bar{2}0\}$	$\{11\bar{2}0\}\langle 11\bar{2}0 \rangle$	4
Pyramidal $\langle c+a \rangle$	$\langle 11\bar{2}3 \rangle$	$\{11\bar{2}2\}$	$\{11\bar{2}2\}\langle 11\bar{2}3 \rangle$	5

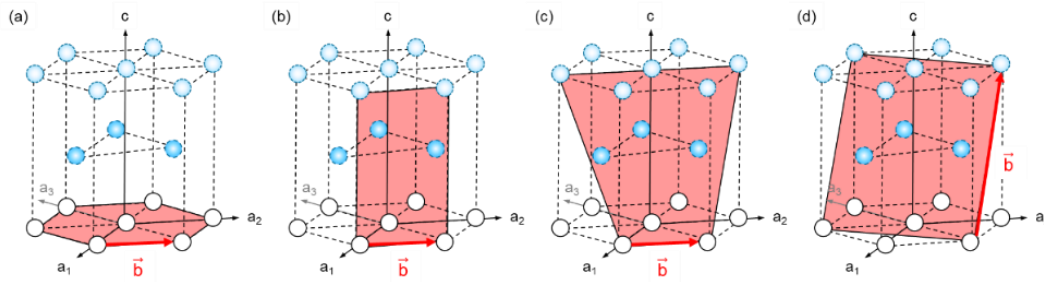


Fig. 2.2.4 Slip plane and direction for deformation slip systems in HCP, (a) basal $\langle a \rangle$ slip, (b) prismatic $\langle a \rangle$ slip, (c) pyramidal $\langle a \rangle$ slip, and (d) pyramidal $\langle c+a \rangle$ slip [38, 47]

2.2.2 Deformation twin

The deformation twin has been generally known to provide an additional deformation mode in Mg alloy to fulfill the lack of slip systems. In addition to that, if the available slip systems are restricted, the twin allows the strain accommodation along the c -axis of the HCP structure. In the classic definition, twin and matrix lattice are related, either by a mirror reflection in a defined plane or by the rotation around a defined axis. Thus, these lattice structures are equivalent but with different orientations [57]. The deformation twin has characterization as follows:

- Twin can be simply activated under only one direction of the polar mechanism.
- The plastic shear by twin is small.
- Twin has a limited contribution to plastic shear.
- Twin causes a sudden and large change in the orientation of the crystal lattice.

In the Mg, possible twin modes are related to the ratio of a and c lattices (c/a ratio) [47]. Fig. 2.2.5 shows the variations of the shear of possible twin modes as a function of the c/a ratio in HCP metals. For each twin mode, the compression twin is activated when the slope is positive according to the c/a ratio of materials. In contrast, the extension twin is activated when the slope is negative. For instance, the $\{10\bar{1}2\}\{10\bar{1}\bar{1}\}$ twin is a tension twin because of a positive slope at the c/a ratio (1.624) in the Mg, while the $\{10\bar{1}1\}\{10\bar{1}\bar{2}\}$ twin is a compression twin with a negative slope. Three types of deformation twins in Mg are summarized in Table 2.2.2. The $\{10\bar{1}2\}$ tension twin is a predominant twin mode with the smallest shear stress. As shown in Fig. 2.2.5, the twin of the Mg alloys has relatively

lower shear stress. However, the twin is restricted due to the typical basal type texture, exhibiting the alignment of the c -axis parallel to the ND on the sheet by the rolling process in Mg alloy sheets. This means that the tension and compression twin can be activated only in the deformation along the ND. The twin can accommodate the amount of strain directly proportional to the volume fraction of crystal that has twinned, and its amount of strain accommodation is limited, even under ideal circumstances. Under a theoretical tensile strain, the limited amount is known as a maximum $\varepsilon = 6.5\%$, not including secondary twin [58]. However, the twin activation is rather influential in an aspect of role in the reorientation of unfavorably oriented crystals to favorable orientations to activate various slip systems, even if their amount is limited [25].

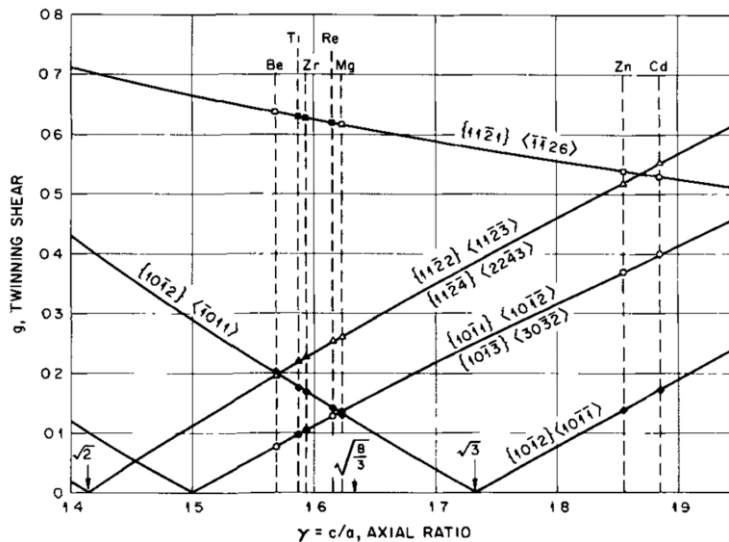


Fig. 2.2.5 Variation of twin shear as a function of the c/a ratio in HCP [47]

Table 2.2.2 Deformation twin modes observed in the Mg and its alloys

Twin mode	Shear direction	Orientation angle	Shear stress parallel to the c -axis
$\{10\bar{1}2\}$ Tension twin	$\langle 10\bar{1}1 \rangle$	86°	Tension
$\{10\bar{1}1\}$ Compression twin	$\langle 10\bar{1}2 \rangle$	56°	Compression
$\{10\bar{1}2\}$ - $\{10\bar{1}1\}$ Double twin	$\langle 10\bar{1}2 \rangle$ - $\langle 10\bar{1}1 \rangle$	38°	Compression

2.3 Texture development in Mg alloys

2.3.1 General description about texture

Both natural and processed polycrystals of all metallic materials show the anisotropy in the physical, chemical, and mechanical properties as a single crystal if the polycrystalline is predominantly oriented in one direction or similar directions, namely crystallographic texture or texture [25, 59, 60]. This case is called a strong texture development. The preferred orientation of the crystallites in a specific sample direction correlates directly to the beneficial or harmful material property [25, 38]. Contrarily, the random orientation exhibits isotropic material properties. This case is called a random or a weak texture. The texture is one of the critical points in materials science to optimize the material properties of final products. The texture can be controlled by thermomechanical treatments or alloying elements [9, 61].

Generally, the texture description is represented as the orientation distributions of crystallites concerning a given sample coordinate system [60]. Two coordinate systems, which are a sample coordinate system and a crystal coordinate system, are required, as shown in Fig. 2.3.1 (a). As the sample coordinate system, K_A , the external shape of a sample, e.g. normal, rolling, and transverse directions (ND, RD, and TD, respectively) in the case of a rolled sheet, is used. The crystal coordinate system, K_B , is defined according to the crystal symmetry, e.g. $[10\bar{1}0]$, $[0001]$, and $[11\bar{2}0]$ in the HCP structure [25, 60]. The relationship between both coordinate systems are expressed as the orientation, g , as followed:

$$K_B = g \cdot K_A \quad (K_A - g \rightarrow K_B) \quad (eq. 2.3.1)$$

This equation means the K_A is transformed by g (orientation) into the K_B . The orientation, g , is presented in various methods, for example, by Miller-indices with $(hkil)[uvtw]$ or by Euler angles with $\{\varphi_1, \Phi, \varphi_2\}$. Both methods are frequently used in texture representation. The Miller-indices with the indices $(hkil)$ and $[uvtw]$ is used in this work. The indices $(hkil)$ stand for a crystallographic plane oriented perpendicular to the

sheet-normal direction and $[uvw]$ is for the crystallographic direction parallel to the rolling direction, in the case of the rolled sheet.

The orientation distribution function (ODF) is calculated from the measured pole density distribution functions, $P_{hkl}(\alpha, \beta)$, pole figures. This procedure is the pole figure inversion. Fig 2.3.1 (b) ~ (d) illustrates the general concept for the pole figure, which offers information for the probability of the distribution of the lattice plane, which is placed at a specific position concerning the sample coordinate system. In order to present the distribution of the lattice plane from the reference sphere to the projection plane, a point on the surface of the reference sphere is connected to the south pole (projected pole), and it is defined as a projected point on the projection plane (a plane of pole figure) by the intersection line. This method is a stereographic projection that is applied in this work. If (0001) planes of lattice plane are located like Fig 2.3.1 (b), the (0001) planes are tilted at approximately 20° from the ND to the TD, consequently, the (0001) poles are displayed in spread poles at 20° away from the ND, Fig 2.3.1 (c). This pole intensity (or density) distribution is commonly presented as contour lines, Fig 2.3.1 (d) [25, 38, 60]. The pole intensity is given as the multiple of the random distribution (m.r.d.). In the case of fully random orientation distribution, the pole intensity will be 1 m.r.d..

The pole figures are usually measured by various diffraction techniques, e.g. X-ray diffractometer (XRD), neutron or synchrotron diffraction facilities, and electron backscatter diffraction (EBSD). The measured coverage of the pole figure is different due to the difference in the measurement method for each technique. The coverage of the pole

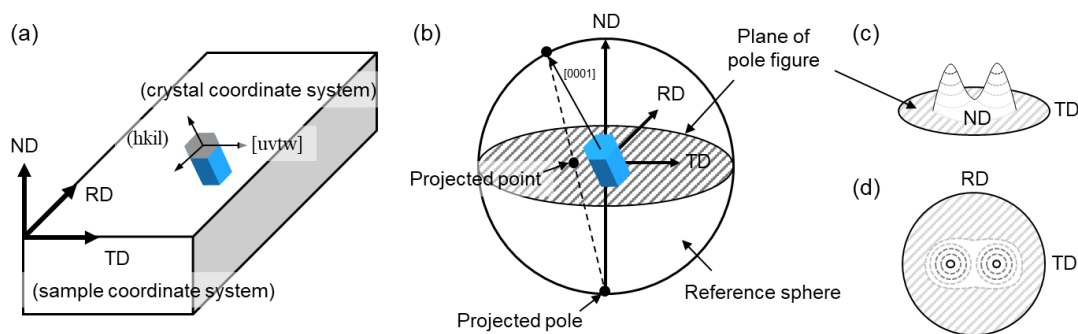


Fig. 2.3.1 (a) Schematic illustration of the sample and crystal coordinate systems, (b) the sample and crystal directions in reference sphere, (c) pole intensity (or density) distribution on the projected points, and (d) its contour plot [25]

figure measured from the XRD measurement is incomplete, while that from the synchrotron diffraction measurement is complete.

2.3.2 Texture development in HCP metals, especially in Mg alloys

Cold-rolled textures in HCP metals were generally categorized into three types according to their c/a ratio, i.e. materials with c/a ratios approximately equal to (Mg or Co), greater than (Zn or Cd), and less than (Ti or Zr) the ideal value of 1.633 in the past [9, 25, 62-64]. An experimental illustration of the cold-rolled texture expected for these categories is shown in Fig. 2.3.2. The deformation textures categorized with a close to the ideal value of 1.633 like the Mg show a typical basal type texture. Such basal texture is a direct consequence of the dominant basal slip [6-9]. Contrarily, the deformation textures categorized with a greater or less than 1.633 show that the basal planes are split towards the RD or TD, respectively. It was reported that the texture split toward the RD is interpreted by a combination of basal slip and a large amount of the twins, and the texture split toward the TD is formed by significant contributions of slip on the prismatic planes as well as twin activation, Fig. 2.3.2 (b) and (c), respectively [29, 62, 63].

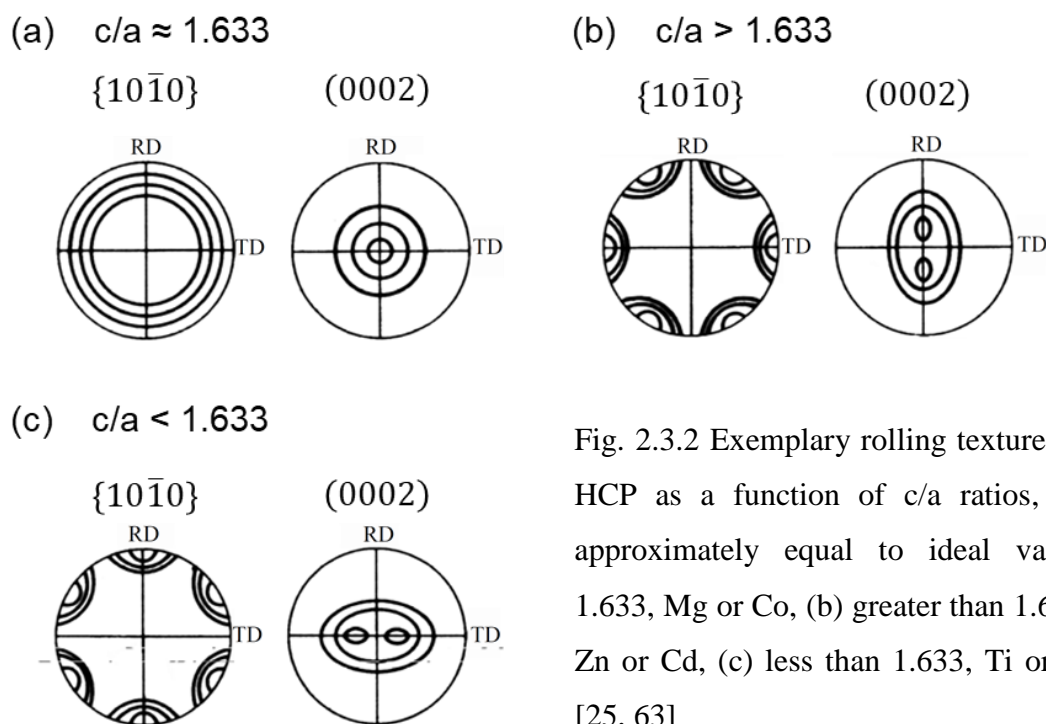


Fig. 2.3.2 Exemplary rolling textures in HCP as a function of c/a ratios, (a) approximately equal to ideal value, 1.633, Mg or Co, (b) greater than 1.633, Zn or Cd, (c) less than 1.633, Ti or Zr [25, 63]

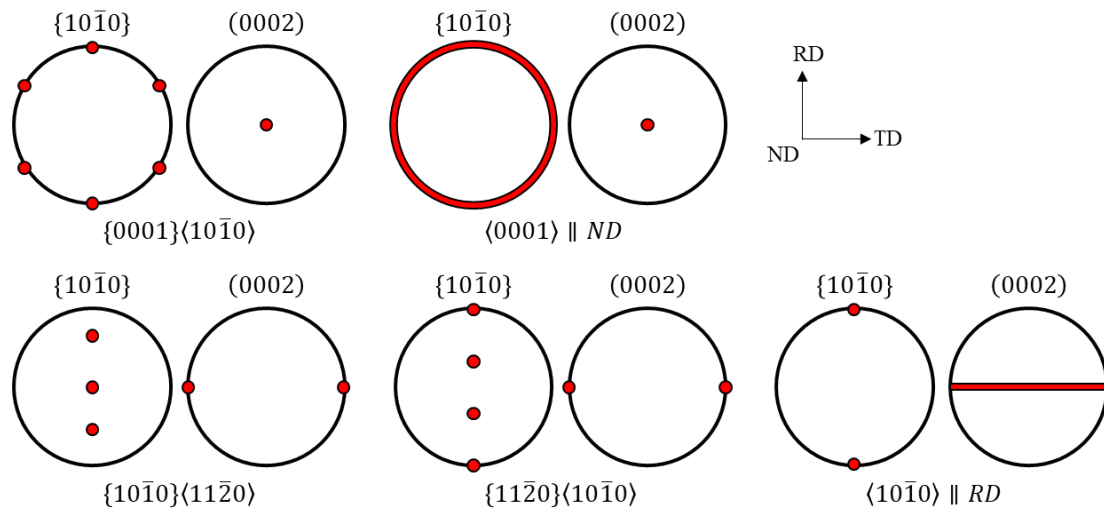


Fig. 2.3.3 Ideal texture components in the (0002) and $\{10\bar{1}0\}$ pole figures of the Mg and its alloy [65]

The basal type textures observed in the Mg and its alloys are variously interpreted as an ideal $\{hkil\}\langle uvw \rangle$ component or as a fiber component with the fiber axis $\langle uvw \rangle$ parallel to a preferred sample axis. Fig. 2.3.3 schematically shows the possible ideal components in (0002) and $\{10\bar{1}0\}$ pole figures. This description allows the expression of more detailed texture development [65].

As described in Chapter 2.2, the basal type texture exhausts the possibility to activate other slip or twin activation required to accommodate the external plastic strain. The textures weakened by adjusting various factors, e.g. alloying composition, temperature, and processing parameter, have received particular attention in Mg research for the engineering application because the textures weakened play an important role in determining the ductility and formability [8, 21, 29, 38, 62, 66].

It is known that the addition of certain alloying elements is an effective way to modify the textures. The alloying elements added to Mg play an important role in the activation of various deformation modes and the recrystallization behavior, such that the modification of the basal type texture can be achieved. The generally known effect of alloying elements, used in this work, in Mg are restrictively described as follows:

- Zinc (Zn) is one of the main alloying elements in Mg alloys. It is known that the addition of Zn leads to effective grain refinement but no texture modification [67]. The addition of over 1.5 wt.% Zn tends to form a hot crack [38].
- Zirconium (Zr) is well known as an extreme grain refining agent due to the formation of stable compounds combined with the other elements, e.g. Zn, Al, Y, and RE elements [68]. The Zr provides considerable sites for nucleation, even in small amounts added [69]. However, it is shown that Zr is not an effective element for texture modification in combination with Zn during processing [21].
- RE elements are well known as an effective alloying element for texture modification when their content is generally above 0.01 at.% [11]. The texture exhibits a non-basal type texture with relatively weak intensity, e.g. the basal poles tilted from the ND toward RD or TD in a rolled sheet. The addition of RE elements, such as Ce, Nd, and Gd as well as Y, usually leads to the formation of a non-basal type texture, in which basal poles spread from the ND towards RD after the thermomechanical processes of Mg-RE binary alloys [10, 13, 32]. Simultaneous addition of Zn or Mn with RE elements, as Mg-RE-Zn or Mg-RE-Mn alloy system, results in a distinct texture, in which the basal poles broaden from the ND towards TD [20, 21, 70].
- Calcium (Ca) is a potential element to replace the RE elements as a texture modifying alloying element. The individual addition of Ca or its combined addition with Zn or Al was also shown in the earlier works [16, 17, 71] as an effective way to modify the texture, similar to the addition of RE elements.

In addition to alloying elements, the texture modification via changing the processing conditions was reported by Yi et al.[20]. By changing the pass reduction degree during the rolling of Mg-Al-Zn-Y-Ca alloy, the texture could be significantly weakened with the widespread basal poles from the ND toward RD and TD. In this way, the deformation textures can be controllable to be developed either into the typical basal texture or non-basal type textures [7, 8, 34, 72].

An example of the texture control mentioned above is shown in Fig. 2.3.4. The tendency of formation of basal texture in three different Mg alloys, Mg-Al-Zn (AZ31), Mg-Zn-Mn (ZM21), and Mg-Zn-Ce (ZE10), is found in Fig. 2.3.4 (a) ~ (c). In some cases, the basal texture component disappears, and a distinct texture component evolves with the basal

pole spread in the RD or TD in the ZE10 sheets, Fig. 2.3.4 (d) and (e), only by changing the process conditions. It is obvious that the alloying element and thermomechanical treatments have a significant influence on the development of textures and microstructure. In particular, recovery and recrystallization processes are effective in Fig. 2.3.4 (c) ~ (e). Several different recrystallization mechanisms were discussed with regard to their effect on the development of texture in the massive forming or deformation of Mg alloys. However, there is still a lack of understanding of the mechanisms that have a major influence on the texture development of Mg alloys. The alloying elements and processing parameters influencing modified texture formation are directly or indirectly associated with the activation of deformation mechanisms. In this context, the techniques for interpreting the deformation mechanisms on the texture evolution, e.g. distinguishing predominant deformation modes and their combinations, are importantly required.

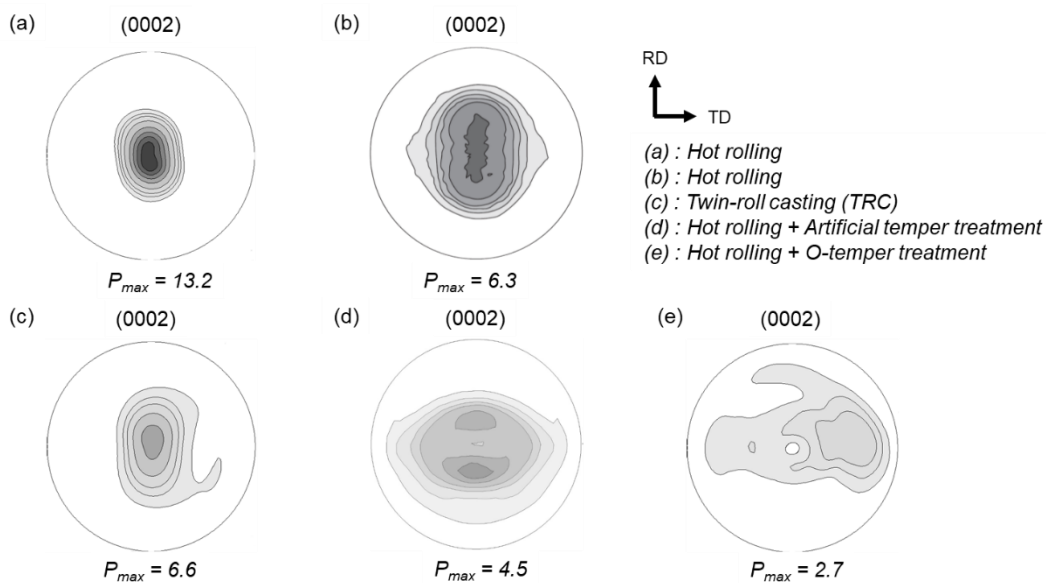


Fig. 2.3.4 (0002) pole figures developed with various thermomechanical processes on (a) AZ31, (b) ZM21, (c), (d), and (e) ZE10 [8, 21]

3 Dislocation and texture evaluations with synchrotron radiation

The need for evaluating dislocation structures, which is essential to understand the relationship between texture and slip activity, is described in full above. The dislocation structure in various metals is analyzed most commonly by providing a direct image of TEM microstructure [51, 52, 73-76]. However, the TEM analysis of complicated dislocation structures, especially with a high dislocation density in a largely deformed status, is not suitable because of the difficulties in identifying each dislocation. In addition to the sample preparation that requires extreme care, a small measurement area in a range of μm limits the application of TEM analysis to various experimental schemes, e.g. a real-time measurement and statistical analysis. A more statistically robust method is desirable in order to understand the role of dislocations to the texture development, as it usually forms at a high deformation degree.

Since the activities of a particular slip (or dislocations) manifest as a deviation of the lattice planes during the deformation [54, 77], one of the most effective methods is X-ray line profile analysis. The deviation of the lattice planes is directly measured as the changes of the diffraction patterns with a varied peak shape and peak broadening [50, 78, 79]. In addition, a decrease in the peak width also provides information about the relaxation of internal stress, i.e. recrystallization or recovery behavior, depending on temperature [80, 81]. From the early 2000s to today, X-ray sources including synchrotron radiation, modern area detectors, and proper theoretical models with fast computer technology have been rapidly developed so that a sufficient potential has been provided to analyze complicated dislocation structures with advanced experimental methods [78, 79, 82]. These techniques possess a high advantage of possible applications in a wide field of new experiments, e.g. lattice strain, texture analysis, dislocation density, dislocation character, crystallite size, and distributions, especially *in-situ* X-ray diffraction measurement combined with thermomechanical experiments [43, 54, 59, 65, 66, 80, 83-87].

3.1 Introduction of synchrotron radiation

Synchrotron radiation emits in the tangential direction to the orbit when electro-charged particles, i.e. the electrons or positrons, move close to the speed of light in the storage ring and are forced to change flight direction by a magnetic field. The brilliance and divergence of the hard X-rays at synchrotron are changed in energy ranges from meV to around 100 MeV according to the types of magnetic components in worldwide beamlines. The energy range can be chosen by adjusting the spacing of the magnetic field [59]. Thereby, it can be widely utilized for the needs of many types of research. In addition to the energy range, excellent brilliance and high penetration depth through materials in the same order as with thermal neutrons provide high resolution to material science research. Since a divergence of the synchrotron beam offers the possibility of the high orientation resolution in a range of 0.01° or even better [84], there is a great advantage to analyze the atomic scale phenomena. By the high photon energy in the range 50-200 keV, which is higher intensity compared to conventional X-ray in the laboratory (Co - K_α : 6.92 keV and Cu - K_α : 8.05 keV), high penetration depth and short-time measurement with fast read-out area detector can be achieved [25, 59]. Moreover, a short time measurement offers a possibility for *in-situ* techniques under various combinations of experimental methods, e.g. under mechanical loading and/or at different temperatures. The energy and penetration depth of synchrotron radiation is listed compared to thermal neutron and conventional X-ray in Table 3.1.1.

Table 3.1.1 Energy and penetration depth of synchrotron radiation, thermal neutron, and conventional X-ray in several materials [25]

	Energy (keV)	Wavelength (Å)	Penetration depth (mm)			
			Mg	Al	Ti	Fe
Synchrotron radiation	100	0.12	34	22	8	8
	150	0.08	42	27	13	4
Thermal neutrons	6.88	1.80	61	96	17	8
Co - K_α	8.05	1.79	0.09	0.048	0.007	0.023
Cu - K_α	6.92	1.54	0.14	0.074	0.011	0.004

3.2 Line profile analysis using X-ray diffraction

Theoretical X-ray diffraction peaks change based on the three function profiles, i.e. strain, size, and instrumental functions. Fig. 3.2.1 shows exemplarily the typical peak aberrations and their sources in the X-ray diffraction pattern. The peak broadens if lattice defects are abundantly present, e.g. dislocation density larger than about $5 \times 10^{12} \text{ m}^{-2}$, and the position of peak shifts if the internal stresses are present in the lattice structure [88]. These peak aberrations provide useful information for studying the dislocation structure, i.e. sources of strain at the irradiated area of the sample when the peak broadening is caused by the strain rather than the other functions [50, 78].

Two different methods of the X-ray line (or peak) profile analysis are generally known. One is the Breadth method, and the other is the whole (full) profile or pattern fitting methods. The Breadth method is the so-called Williamson-Hall procedure. This method is based on the different order dependence of the various physical effects causing the broadening of diffraction peak profiles in terms of a change in full width at half maximum (FWHM). In the Williamson-Hall procedure [54, 89, 90], if the strain is caused by dislocations, the strain broadening increases with K (or g , $2\sin\theta/\lambda$) and is usually

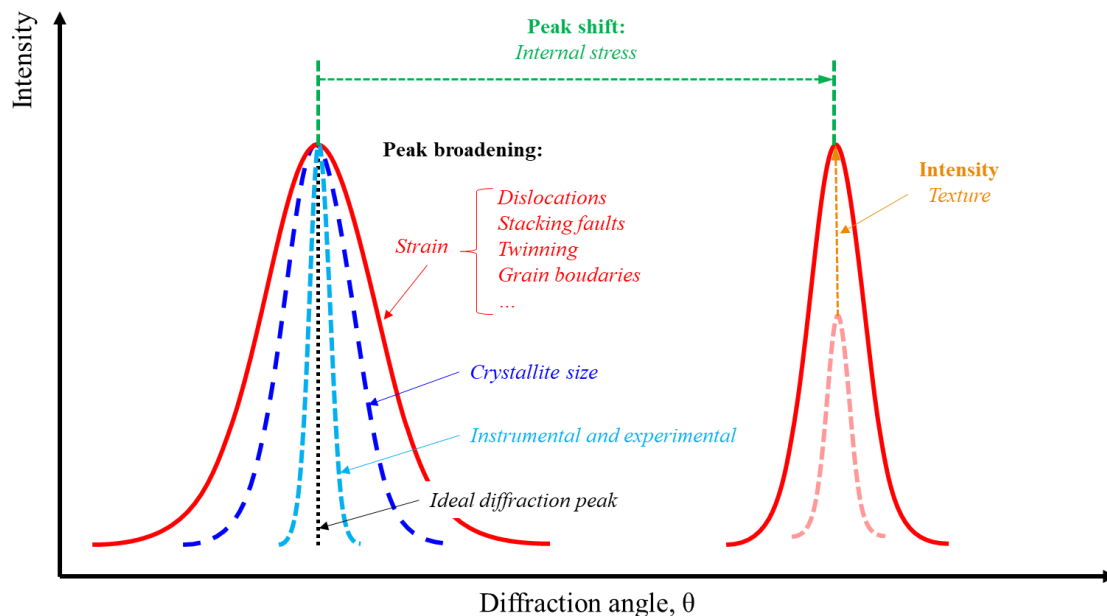


Fig. 3.2.1 An exemplary peak aberrations and their sources in the X-ray diffraction pattern [88]

anisotropic. The ΔK values defined as the FWHMs of the corresponding peaks can be plotted as a function of K , so-called the Williamson-Hall plot. This plot provides qualitative information with the slope of the curve about the peak broadening sources, which is useful for discerning the contribution of deformation types [91]. An exemplary Williamson-Hall plot is shown in Fig. 3.2.2. If the ΔK (or FWHM) is distinctly caused by the strain, the slope increases with K , Fig. 3.2.2 (b), whereas if it is caused by planar or stacking faults, the slope does not increase with K , Fig. 3.2.2 (a). In further plotting concerning dislocation contrast factors, the dislocation density of measured material can be calculated, so-called the Wilkens model or modified Williamson-Hall plot [79, 92].

Next, in the whole profile fitting method, whole peaks (reflections) are fitted simultaneously, unlike the Breadth methods in which the broadening of diffraction peak

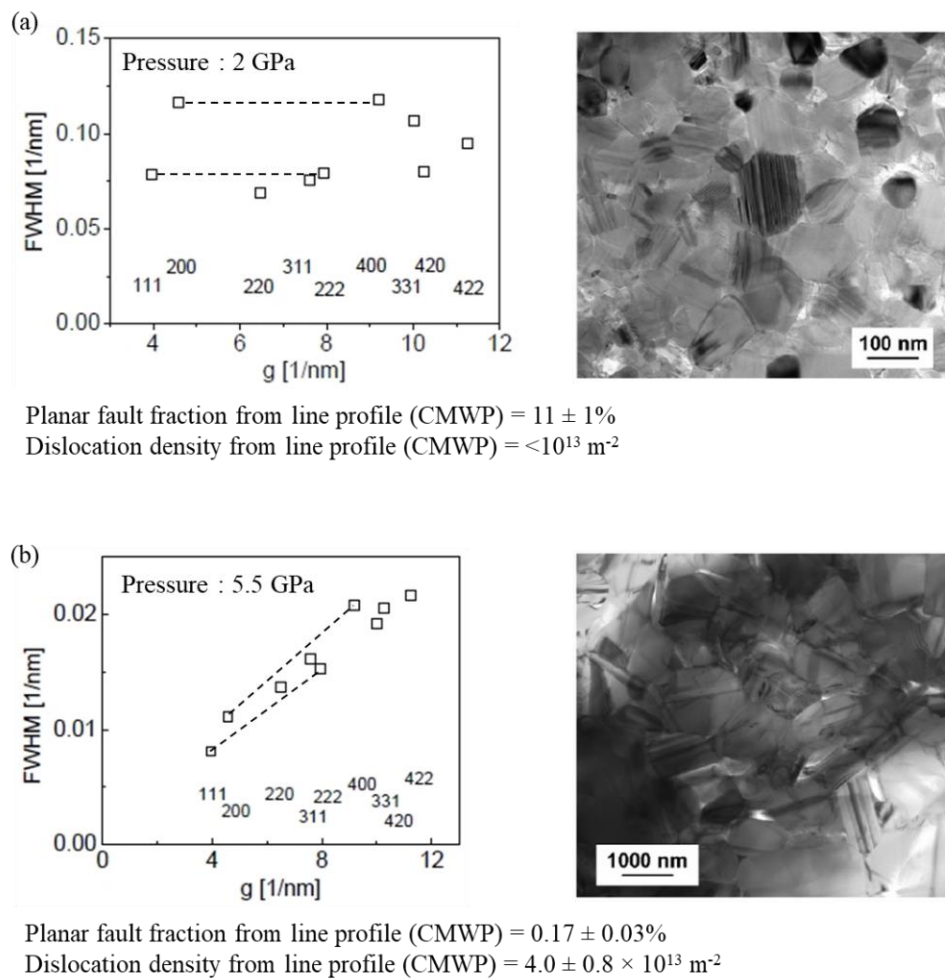


Fig. 3.2.2 The convolutional Williamson-Hall plot and TEM images measured at the pressure of 2 GPa and 5 GPa of SiC specimens sintered at 1800°C [91]

profiles is fitted according to the order of the profiles. The effect of size and strain on its profile broadening is theoretically considered as that of Breadth methods. Most full profile fitting methods are based on fitting the measured profiles by Fourier transform of analytical profile functions, e.g. Gauss, Lorentz, Voigt [93, 94]. However, these procedures have difficulties fitting the maximum intensity and the tail of the peak simultaneously in an analytical profile function. This is also the case with the Breadth method of the FWHM analysis. In order to overcome these difficulties, Convolutional Multiple Whole Profile (CMWP) fitting has been developed that can directly fit measured diffraction patterns by using fundamental physical principles without using the Fourier transform of the analytical profile functions. Fig. 3.2.3 shows an example of the comparison between fitting results by the CMWP and one of the classical line profile

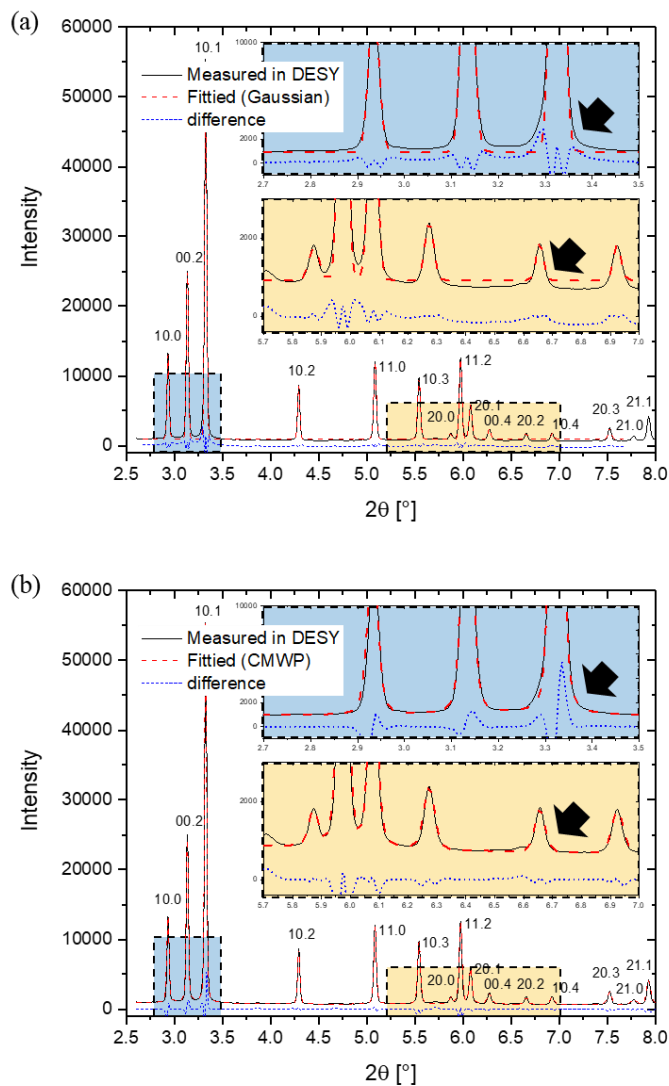


Fig. 3.2.3 The measured and fitted diffraction patterns as a function of 2θ using (a) analytical function with Gaussian and (b) the CMWP fitting procedure for examined ZN10 sheet after deformation along the rolling direction to $\varepsilon = 20\%$ at room temperature (RT)

method using an analytical function with Gaussian. As a result of comparing both line profile analysis methods, the CMWP fitting procedure clearly shows the appropriate fitting result, especially in the tail of the profiles marked as the black arrows in Fig. 3.2.3. Thus, the CMWP fitting procedure enables to evaluate X-ray diffraction patterns as a more advanced line profile method in terms of crystallite size and dislocation density. The diffraction profiles are fitted using the theoretical functions depending on the indices (hkl) and simultaneously on the microstructural parameters in the CMWP fitting procedures. The values of the microstructural parameters relating to the size distribution, dislocation density, and strain anisotropy are connected and are refined during the fitting procedure. The strain anisotropy parameters refined after the fitting procedure can be used to evaluate the dislocation characterization, such as dislocation activity. More details for the CMWP fitting procedure will be described in Chapter 3.2.1.

3.2.1 Convolutional Multiple Whole Profile (CMWP) fitting method

In the CMWP fitting method, each diffraction pattern is fitted by the sum of a background spline, and the convolution of the instrumental pattern, and the theoretical line profiles related to crystallite size, which is caused by coherently scattering domains, and dislocations [50, 54, 78, 79]. The instrumental profile has to be measured separately using a stress-free standard sample, e.g. LaB₆.

The theoretical profile functions used in the CMWP fitting procedure are calculated based on a model of the microstructure with the following 3 conditions: (1) the crystallites as a spherical shape, (2) log-normal size distribution, and (3) the strain is caused primarily by dislocations. The CMWP fitting procedure provides the dislocation density, ρ , and the parameters q_1 and q_2 that allow the evaluation to determine the fractions of dislocations in the different particular slip families.

In the CMWP fitting procedure, the strain broadening of the diffraction line profiles depending on the diffraction planes, i.e. indices (hkl), is determined by the mean-squared strain, $\langle \varepsilon_{g,L}^2 \rangle$, in the lattice for the direction of the diffraction vector, g , and the Fourier variable, L . The diffraction vector is given as:

$$g = \frac{2\sin\theta}{\lambda} \quad (\text{eq. 3.2.1})$$

where θ is the diffraction angle, and λ is the wavelength of the X-ray radiation. If dislocations cause the strain, the mean-squared strain can be given as:

$$\langle \varepsilon_{g,L}^2 \rangle \cong \frac{\overline{\rho C_{hkl} b^2}}{4\pi} f(\eta) \quad (\text{eq. 3.2.2})$$

where ρ is the average dislocation density in the measuring volume, and b is the Burgers vector. The $f(\eta)$ is Wilkens function, which implies the mean-squared strain as a function of η with eliminating the logarithmic singularity, where

$$\eta = \frac{L}{R_e} \quad (\text{eq. 3.2.3})$$

L is again the Fourier variable, and R_e is the effective outer cut-off radius of dislocation [92]. $\overline{C_{hkl}}$ is the dislocation contrast factor averaging over all the slip systems, which are populated by dislocations with weights equal to the contributions of the slip systems to the total dislocation density. In hexagonal crystals, 11 slip modes are classified from 3 different types of Burgers vectors: $\langle a \rangle$ type ($b_1 = \frac{1}{3}\langle \bar{2}110 \rangle$), $\langle c \rangle$ type ($b_2 = \langle 0001 \rangle$), and $\langle c+a \rangle$ type ($b_3 = \frac{1}{3}\langle \bar{2}113 \rangle$). Using the notation of Dragomir, the 3 groups of slip system families according to the types of Burgers vector can be considered as 4 slip systems with $\langle a \rangle$ type, 2 of $\langle c \rangle$ type, and 5 of $\langle c+a \rangle$ type, as shown in Table 3.2.1 [77].

In terms of the fraction, h , of each dislocation type, the average contrast factor, $\overline{C_{hkl} b^2}$, is expressed as:

$$\overline{C_{hki0}b^2} = b_1^2 \sum_{i=1}^{N(a)} h_i \bar{C}^{(i)} + b_2^2 \sum_{j=1}^{N(c)} h_j \bar{C}^{(j)} + b_2^2 \sum_{n=1}^{N(c+a)} h_n \bar{C}^{(n)} \quad (eq. 3.2.4)$$

where the subscript i , j , and n denote the i th, j th, and n th slip systems of each Burgers vectors in the crystal. $\bar{C}^{(i,j,n)}$ is described in terms of the strain anisotropy for hexagonal crystals [77, 86, 90] as:

$$\bar{C}_{hki0}^{(i,j,n)} = \bar{C}_{hki0}^{(i,j,n)} \left[1 + q_1^{(i,j,n)} x + q_2^{(i,j,n)} x^2 \right] \quad (eq. 3.2.5)$$

$$x = \frac{2}{3} \left(\frac{l}{ga} \right)^2$$

where $q_1^{(i,j,n)}$ and $q_2^{(i,j,n)}$ are parameters depending on the anisotropic elastic properties of the crystal and the type of dislocation slip systems. $\bar{C}_{hki0}^{(i,j,n)}$ is the average contrast factor for the slip systems corresponding to the $hki0$ reflections. The g is above the diffraction vector, l is the respective miller index, and a is the lattice constant. The theoretical values of $\bar{C}_{hki0}^{(i,j,n)}$, $q_1^{(i,j,n)}$ and $q_2^{(i,j,n)}$ for the possibility of all slip systems in the common hexagonal crystals have been calculated, according to the earlier work by Kuzel et al. [83]. The calculated theoretical values of Mg are listed in the earlier work by Dragomir et al. [77], as shown in Table 3.2.2.

Thus, the CMWP fitting procedure provides the average dislocation density, ρ , and the experimental parameters q_1^m and q_2^m as a result of the fitting of peak broadening in consideration with the background spline and instrumental pattern. For determining the density fraction of the populated dislocations, it is assumed that the theoretical values of \bar{C}_{hki0} , q_1 and q_2 are equal to the experimental values of q_1^m and q_2^m . The following equation is obtained by substitution of eqs. 3.2.4 and 3.2.5.

$$\begin{aligned}
q_1^m &= \frac{1}{P} \sum_{i=1}^{11} h_i \bar{C}_{hki0}^i b_i^2 q_1^i \\
q_2^m &= \frac{1}{P} \sum_{i=1}^{11} h_i \bar{C}_{hki0}^i b_i^2 q_2^i \\
\sum_{i=1}^{11} h_i &= 1
\end{aligned} \tag{eq. 3.2.6}$$

where $P = \sum_{i=1}^{11} h_i \bar{C}_{hki0}^i b_i^2$. There is no equation for \bar{C}_{hki0}^m , since it is a dependent parameter in the evaluation of line profiles. The fractions, h_i , cannot be determined from the two equations for q_1^m and q_2^m in eq. 3.2.6, therefore, additional restrictions are made for h_i . It is assumed that the fractions are positive in each Burgers vector group, and their sum should be equal to 1 [54, 77, 86]. The number of the possible combinations from the dislocation slip systems with three Burgers vector equals $(2^4-1)(2^2-1)(2^5-1) = 1395$. A computer program was elaborated in order to determine the possible combination among the different slip systems from the fitted experimental parameters [54, 86]. The program is referred to as *Hexburger*, which is repetitively carried out for the weight of fractions for different Burgers vectors to be non-zero weights. The graphic illustration of possible combinations for the dislocation fractions with three Burgers vectors determined by the *Hexburger* is shown in Fig. 3.2.4.

Table 3.2.1 The notation for the most common slip systems in HCP

Burgers vector types	Slip systems	Sub-slip systems	Burgers vector	Slip plane
$\langle \mathbf{a} \rangle$ type	Basal edge	BE	$\frac{1}{3}\langle \bar{2}110 \rangle$	(0001)
	Prismatic edge	PrE		{01 $\bar{1}$ 0}
	Pyramidal edge	PyE		{10 $\bar{1}$ 1}
	Screw	S1		-
$\langle \mathbf{c} \rangle$ type	Prismatic edge	Pr2E	$\langle 0001 \rangle$	{01 $\bar{1}$ 0}
	Screw	S3		-
$\langle \mathbf{c}+\mathbf{a} \rangle$ type	Prismatic edge	Pr3E	$\frac{1}{3}\langle \bar{2}113 \rangle$	{01 $\bar{1}$ 0}
	Pyramidal edge	Py2E		{21 $\bar{1}$ 2}
	Pyramidal edge	Py3E		{11 $\bar{2}$ 1}
	Pyramidal edge	Py4E		{10 $\bar{1}$ 1}
	Screw	S2		-

Table 3.2.2 The theoretical values of the parameters \bar{C}_{hki0} , q_1 and q_2 for all slip systems of the Mg

Burgers vector types	Sub-slip systems	\bar{C}_{hki0}	q_1	q_2
$\langle \mathbf{a} \rangle$ type	BE	0.19483	0.067864	-0.19759
	PrE	0.33713	-1.14306	0.326649
	PyE	0.2986	-0.86223	0.170791
	S1	0.12366	1.191931	-1.008
$\langle \mathbf{c} \rangle$ type	Pr2E	0.03967	4.880886	1.079577
	S3	-2.3×10^{-4}	-2471.84	1412.024
$\langle \mathbf{c}+\mathbf{a} \rangle$ type	Pr3E	0.08297	3.055985	-1.01943
	Py2E	0.08233	1.750516	0.248391
	Py3E	0.0817	3.501807	-0.66875
	Py4E	0.0816	2.081515	-0.03236
	S2	0.38948	1.321473	-0.91879

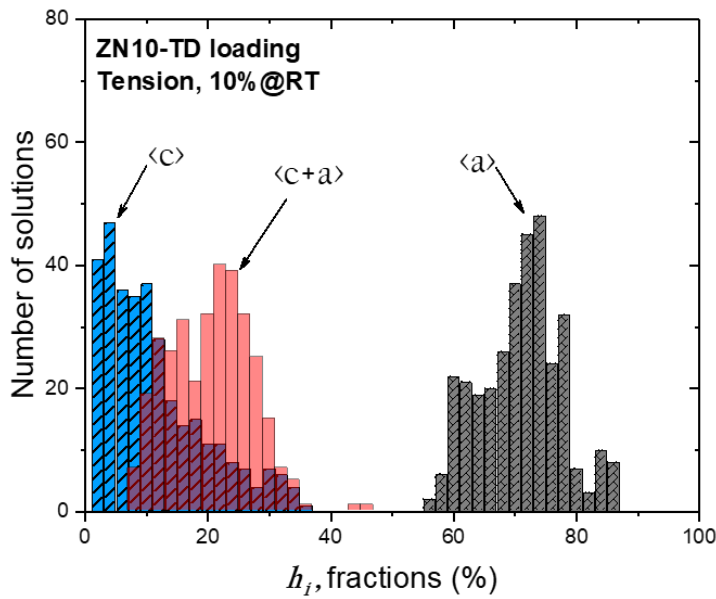


Fig. 3.2.4 The histogram of the solution matrix of the dislocation fractions of three Burgers vectors, a , c , and $c+a$ types, in the case of the ZN10 deformed to $\varepsilon = 10\%$ at RT

3.3 Texture measurement using synchrotron radiation

The texture evolution during the deformation is one of the essential investigations to reveal the active deformation mechanisms since the texture development reflects the deformation history. As aforementioned in Chapter 3.1, a global texture, or a local texture, of a polycrystalline material can be measured within a short time by using synchrotron radiation, especially *in-situ* measurement, to trace the changes in the same sample volume [59]. For texture measurement using synchrotron radiation, the transmission method with a monochromatic beam is generally used. To achieve the monochromatic beam, the primary white beam from the undulator enters through the monochromator chamber, and then the monochromatic beam is collimated by Si single crystals to the desired size and wavelength (or energy). The beam size can be controlled by a collimator in the monochromator chamber, ranging from $10\ \mu\text{m}$ (or smaller) to $500\ \mu\text{m}$, additionally by vertical and horizontal slit systems [95, 96]. The basic beamline set-up for texture measurement, which is applied in this work, is schematically shown in Fig. 3.3.1, based on the High Energy Materials Science (HEMS) P07B beamline at PETRA III in DESY, Hamburg, Germany. The sample is located on the omega, ω , rotation stage, which can rotate the sample coordinate system. The ω rotation stage was mounted on an XYZ-stage, which allows the translation of the sample on the sample perpendicular (X), parallel (Y),

and height (Z) to the beam direction. Therefore, oscillation and/or continuous rotation during the data collection are possible at different beam positions. The translations further make texture measurement possible by the collection of the Debye-Scherrer rings during sample rotation (ω -rotation). Intensity variations along the Debye-Scherrer rings are proportional to pole intensity variations on the corresponding pole figures. That is, one Debye-Scherrer ring at a stationary position in a single detector image covers one circle in the corresponding (hkl) pole figure, Fig. 3.3.2. Thus, the coverage should be extended by the ω rotation of the sample for texture measurement at each step of the ω rotation in order to cover the complete pole figure. The ω rotation is usually set as 3° per step from 0° to 90° or 180° in this work. In general, the ω rotation from 0° to 180° was applied for texture measurement at ambient temperature. However, the ω rotation from 0° to 90° was applied due to the limited rotation by the installed equipment on the rotation stage, e.g. loading device with/without heating module. During the sample rotation, the rotation axis, Z -axis in Fig. 3.3.2, should be precisely fixed to the center of the measured volume; otherwise, the center will be shifted. For accurate texture measurement, the sample volume measured at each ω angle should be the same.

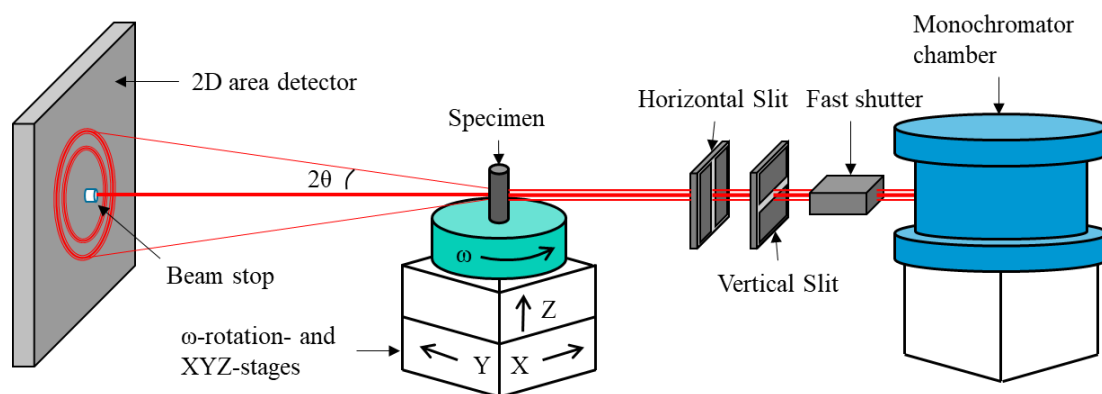


Fig. 3.3.1 Schematic beamline set-up for texture measurement at HEMS P07B in DESY [25, 59]

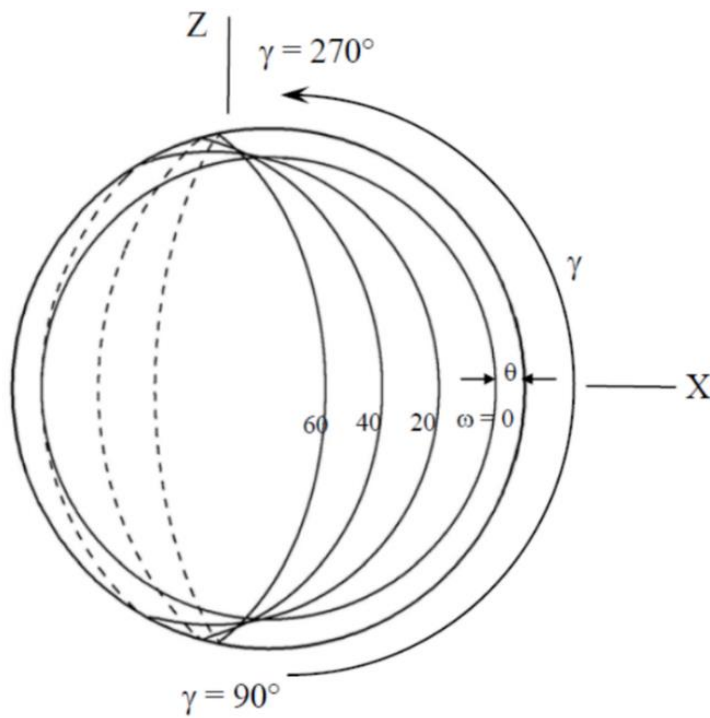


Fig. 3.3.2 Coverage of the Debye-Scherrer rings in a pole figure captured at different ω rotation angles [25]. γ is azimuth angle along the Debye-Scherrer ring

4 Experimental materials and methods

4.1 Experimental materials

Cast ingots of five different compositions, i.e. Mg - 1.32 Zn - 0.13 Zr (ZK10), Mg - 0.61 Nd (N05), Mg - 0.52 Ca (X05), Mg - 1.03 Zn - 0.73 Nd (ZN10), and Mg - 0.91 Zn - 0.54 Ca (ZX10) in wt.%, were prepared by gravity casting. The slabs for rolling experiments were machined from the cast billets to the dimensions of 20 mm in thickness, 200 mm in width, and 100 mm in length. In the case of the ZK10, a small amount (0.13 wt.%) of Zr was added as a grain refiner to restrict abnormal grain growth, which occurred during hot rolling and subsequent annealing of binary Mg-Zn alloys [28, 67]. The abnormal grain growth hinders the appropriate collection of the Debye-Scherrer ring for the *in-situ* experiments. It is assumed that the influence of Zr addition is negligible on the main deformation and recrystallization mechanisms, and the development of deformation texture, in comparison to the binary Mg-Zn alloy. Indeed, the ZK10 exhibits a similar deformation and recrystallization texture to that developed in the Mg - 2Zn alloy [21, 28, 67]. This allows considering ZK10 as a benchmark alloy, which does not contain Ca or RE, for the other alloys.

Hot rolling was carried out at 400°C on ZK10, N05, X05, and ZN10 and 370°C on ZX10 up to a final thickness of 8 mm. The thickness reduction degree was between 10% and 20% per pass, and the intermediate annealing was conducted for 600 to 900 s at the rolling temperature after each rolling step to avoid the cracking or fracture caused by cooling of the slabs. In order to achieve the comparable grain sizes in each alloy, the different conditions of hot rolling and annealing of the hot-rolled sheets, e.g. annealing temperature and time, were applied, as listed in Table 4.1.1. This allows the evaluation of deformation mechanisms of different alloys without suffering from grain size effects. Moreover, the comparable grain sizes in the examined alloys ensure enough grain statistics appropriate for *in-situ* X-ray experiments.

Table 4.1.1 The conditions of hot rolling and annealing applied to examined 5 Mg alloys

Alloys	Rolling			Annealing	
	Temperature (°C)	Thickness reduction (ϕ)	Final thickness (mm)	Temperature (°C)	Time (sec.)
ZK10	400	0.10, 0.15	8.10	400	900
N05	400	0.10, 0.15	8.05	400	900
X05	400	0.10, 0.20	8.24	400	1800
ZN10	400	0.10, 0.15	8.10	400	1800
ZX10	370	0.05, 0.10, 0.15	8.13	370	900

4.2 *In-situ* experiments under tensile loading

4.2.1 Tensile tests

Dog-bone shaped tensile samples with a gauge length of 20mm and diameter of 4 mm were machined from all sheets in the rolling direction (RD) as well as in the transverse direction (TD) according to the *DIN 50125* (Deutsches Institut für Normung).

A universal testing machine (UTM) was installed at the beamline, HEMS-P07B, at PETRA III in DESY, Hamburg. The tensile tests were conducted with collecting the stress and strain by using a *LabVIEW*-based main control program [25]. Fig. 4.2.1 (a) displays the load and displacement variations as a function of time. Tensile tests were carried out into two different schemes up to fracture or 30% of tensile strain, at different temperatures, RT, 100°C, and 200°C. One corresponds to a continuous loading at a constant strain rate, which denotes a conventional tensile test. The other is carried out in combination with *in-situ* measurements, indicating stress relaxations during the texture measurements with stopping or delaying the strain. The tensile tests with both schemes were carried out under the same testing conditions. Fig. 4.2.1 (b) compares the flow curves from the conventional tensile tests with those obtained during *in-situ* measurement. The flow curves from the conventional test verify the validity of the tensile behaviors measured by the *in-situ* measurement. The consistency of the flow curves indicates no significant influence of the

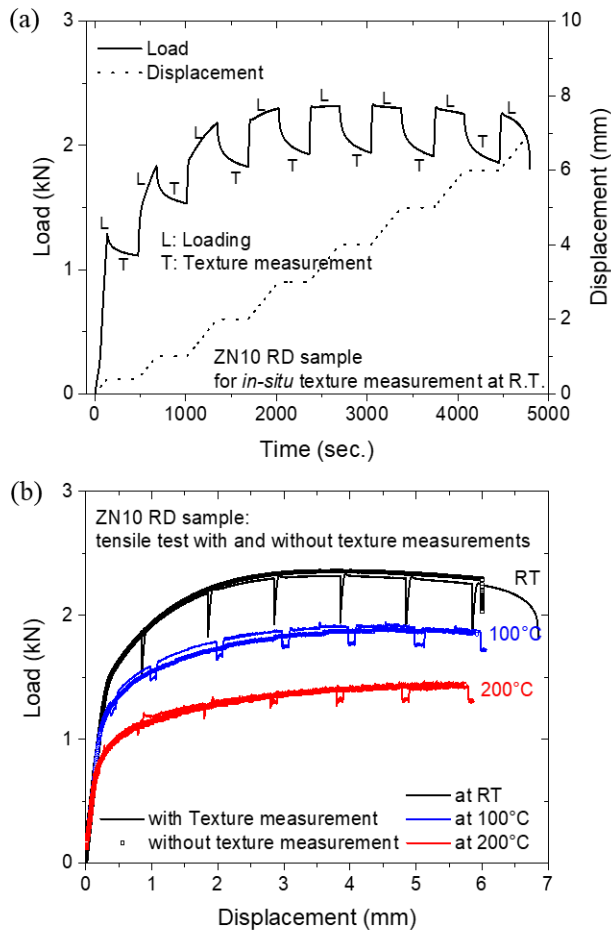


Fig. 4.2.1 An example of the tensile test along the RD in the examined ZN10, (a) Load and displacement profiles as a function of time during the *in-situ* experiment and (b) the comparison between both flow curves for revealing the effect of stress relaxation on the mechanical behavior during texture measurement

testing scheme on deformation behavior, i.e. independently on the stress relaxation during the diffraction experiments, even at elevated temperatures. Similar results have also been found in earlier works [25, 28, 67]. For this reason, the influence of stress relaxation is not considered for the texture development and activities of the main deformation mechanisms. The tensile tests with both schemes for the examined sheets are illustrated in Fig. A.1 in the appendix.

For the tensile test at elevated temperature, a thermocouple was attached to the tensile sample to control the temperature, Fig. 4.2.2. The screw parts of the tensile sample were prolonged to mount the thermocouples, indicated as 5 and 6 in Fig. 4.2.2. During the tensile test, the distance between the thermocouple (5 in Fig. 4.2.2) and the induction coil (4 in Fig. 4.2.2) becomes larger with the sample elongation, that results in the temperature increase, to be higher than the set temperature, at the gauge volume due to the increased distance. Therefore, a continuous adjustment of the temperature is required during tensile

tests at elevated temperature regarding the increased distance between the thermocouple and the induction coil. An example of the set temperature (dashed line) continuously adjusted with increasing the distance (open circle) between the thermocouple and the induction coil is shown in Fig. 4.2.3. By doing so, the sample temperature (solid line) could be maintained constant during the *in-situ* experiments. The time for decrease and retention of the set temperature was calculated based on strain rate, exposure time of beam, and sample rotation. The commercial computer software *SensorTools* provided by the producing company of the induction heating module was used to control all numerical parameters regarding temperature and time.

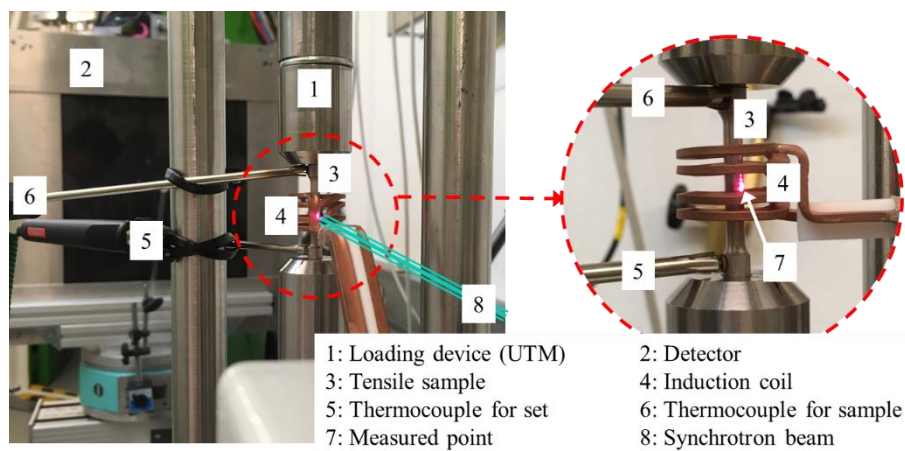


Fig. 4.2.2 UTM installed at the beamline and its elements for the *in-situ* measurement at elevated temperature

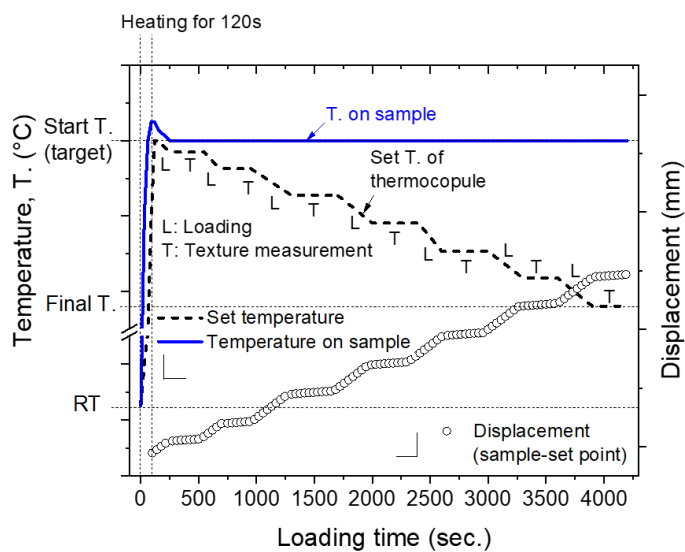


Fig. 4.2.3 An example of controlling temperatures with the set thermocouple and sample in dependence on the distance between the thermocouple and induction coil

4.2.2 *In-situ* texture measurement using synchrotron radiation

An *in-situ* experiment is carried out using synchrotron X-ray radiation combined with a 2-dimensional area detector, a PerkinElmer XRD 1621 detector, within a fast read-out time. The area detector allows collecting the diffraction patterns for whole azimuth angles (γ) in one image. The diffraction patterns were evaluated by selecting the various angular ranges using an open-source software *Fit2D* [97].

Synchrotron radiation was used with a beam energy of 87 keV, corresponding to a wavelength of about 0.1421 Å, beam size of $0.6 \times 0.6 \text{ mm}^2$, and a sample to detector distance of 1288 mm for *in-situ* measurements under loading at different temperatures. The tensile loading was conducted with an initial strain rate of $1.5 \times 10^{-4} \text{ s}^{-1}$, and the loading was stopped at selected strains, e.g. 2%, 5%, 10%, 15%, 20%, 25%, and 30%, for texture measurements at room temperature (RT). At elevated temperatures, the loading was significantly delayed to $1.5 \times 10^{-5} \text{ s}^{-1}$ to minimize the stress relaxation. The sample rotation around ω angle to collect the diffraction images for texture measurement was 105° in 3° step. 18 Debye-Scherrer rings were collected in one detector image, and the first 6 Debye-Scherrer rings were used for texture analysis. The $\{10\bar{1}0\}$, (0002) , $\{10\bar{1}1\}$, $\{10\bar{1}2\}$, $\{11\bar{2}0\}$, and $\{10\bar{1}3\}$ reflections obtained from the area detector, which are required to represent orientation distribution function (ODF), were transmuted into diffraction patterns along the azimuth angles, γ , by using the *Fit2D* software. Recalculated pole figures were then obtained by calculating the ODFs using an open-source software *MTEX* [98].

4.2.3 Line profile analysis using the CMWP fitting procedure

X-ray line profile analysis is carried out by means of the CMWP fitting procedure described in Chapter 3.2.1 to evaluate the diffraction profiles, which provide the densities and their activities of $\langle a \rangle$, $\langle c \rangle$, and $\langle c+a \rangle$ dislocations. In order to achieve high grain statistics in the measured area, the collected Debye-Scherrer rings were integrated into one diffraction pattern over a sample rotation of 24° (from 8 images of the Debye-Scherrer rings) around the loading direction (LD) and over an azimuth angle of 24° along the Debye-Scherrer ring. The integrated diffraction patterns were used for the CMWP

fitting procedure. The integration of the diffraction pattern is schematically shown in Fig. 4.2.4 (a), and the integrated diffraction pattern at $\varepsilon = 0\%$ and 10% are shown in Fig. 4.2.4 (b) together with the fitted diffraction profiles using the CMWP fitting procedure.

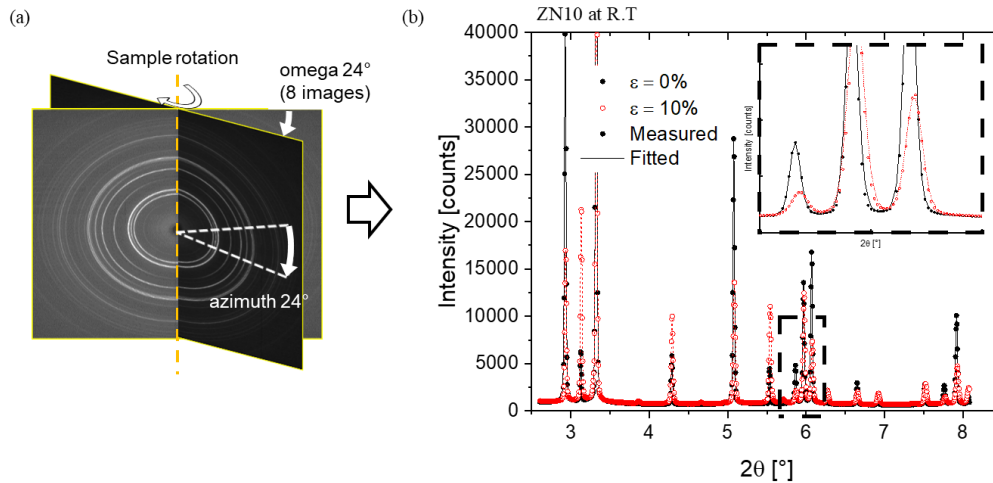


Fig. 4.2.4 (a) Schematic illustrating the integration of area detector images through selected angles of omega and azimuth; (b) diffraction profiles from the integrated diffraction patterns obtained at $\varepsilon = 0\%$ and 10% [28]

4.3 Microstructure and EBSD observations

Optical micrographs of the initial materials after hot rolling and annealing were prepared by standard metallographic sample preparation techniques, e.g., mechanical grinding and polishing with oxide polishing suspension (OPS) lubricant and an etchant based on picric acid [99]. Average grain sizes were measured from the longitudinal section by using a linear intercept measurement computer-assisted of the commercial program *analySIS pro* provided from *Olympus Soft Imaging Solutions GmbH*. A scanning electron microscopy (SEM) is employed to observe the microstructure using a TESCAN Vega SB-U III SEM with an accelerating voltage of 15 kV and a working distance (WD) of 15 mm.

The EBSD samples for tensile specimens deformed up to $\varepsilon = 10\%$ at different temperatures were separately prepared from the *in-situ* experiments. After reaching $\varepsilon = 10\%$, the specimen was immediately quenched in a water bath. The samples for the EBSD

measurement were prepared by using the same standard preparation techniques with the optical micrograph, which was followed by electrolytic polishing at 33 V and -18°C for 30 s. A field emission gun scanning electron microscope (FE-SEM), Zeiss Ultra 55, equipped with an EDAX/TSL EBSD system with a Hikari detector, was used for constructing EBSD maps. Orientation image mapping (OIM) was performed in 0.5 μm step with 15 kV of accelerating power.

4.3.1 IGMA analysis

The active dislocation slip can be determined by an experimental approach based on the dislocation induced lattice rotation and the analysis of the rotation axes from the EBSD measurement [100, 101]. This method is termed as in-grain misorientation axis (IGMA) analysis. It evaluates the rotation axis of the local misorientation, the so-called Taylor axis [28, 100]. Thus, various dislocation slip and the predominant slip can be relatively easily recognized by analyzing the distribution of the Taylor axis. The Taylor axis is defined as:

$$T_s = n_s \times d_s \quad (\text{Eq. 4.3.1}),$$

where T_s , n_s , and d_s are the Taylor axis, slip plane normal, and slip direction, respectively, for a given slip, s , and the Taylor axis is at a crystallographic direction of low indices lying in the slip plane and perpendicular to the slip direction. From the above assumptions, it is possible to evaluate the dominant slip in a deformed single crystal simply by matching the Taylor axis to the experimental measured IGMA distribution plots. In the HCP structure, the prismatic $\langle a \rangle$ slip induces the lattice rotation around the $\langle 0001 \rangle$ axis, and lattice rotation around the $\langle 1\bar{1}00 \rangle$ axis is caused by the basal $\langle a \rangle$ and pyramidal $\langle c+a \rangle$ slip modes, and the $\langle 10\bar{1}2 \rangle$ axis by the pyramidal $\langle a \rangle$ slip [28, 100, 101]. The rotation axes of the corresponding slip are listed in Table 4.3.1 and plotted in Fig. 4.3.1.

Table 4.3.1 List of rotation axes of the corresponding slip in Mg alloys

Slip systems	Burgers Vector	Number of slip	Rotation axes	Variants
Basal $\langle a \rangle$ $\{0001\}\langle 11\bar{2}0 \rangle$	$\langle a \rangle$	3	$\langle 1\bar{1}00 \rangle$	3
Prismatic $\langle a \rangle$ $\{10\bar{1}0\}\langle 11\bar{2}0 \rangle$	$\langle a \rangle$	3	$\langle 0001 \rangle$	1
Pyramidal $\langle a \rangle$ $\{10\bar{1}1\}\langle 11\bar{2}0 \rangle$	$\langle a \rangle$	6	$\langle 10\bar{1}2 \rangle$	6
Pyramidal $\langle c+a \rangle$ $\{11\bar{2}1\}\langle 11\bar{2}3 \rangle$	$\langle c+a \rangle$	6	$\langle 1\bar{1}00 \rangle$	3

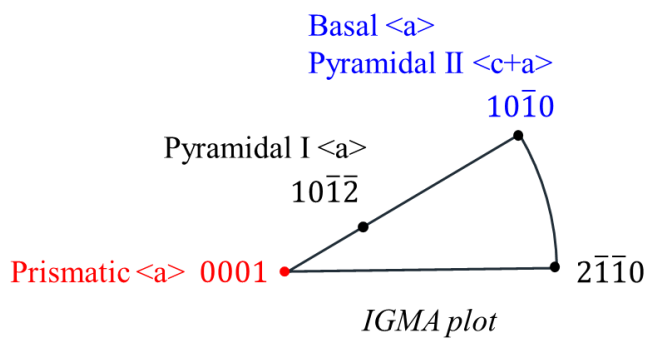


Fig. 4.3.1 Rotation axes of the corresponding slip in the IGMA plot

5 Results and discussion

5.1 Initial microstructure and texture for examined sheets

The optical micrographs of the annealed sheets after hot rolling are shown in Fig. 5.1.1. Fully recrystallized microstructures with equiaxed grains are observed. A comparable grain size was obtained in the examined sheets, while the ZK10 sheet shows a bimodal distribution of the grain size resulting from deformation inhomogeneity. The average grain sizes were 27 μm for ZK10, 23 μm for N05, 22 μm for X05, 23 μm for ZN10, and 17 μm for ZX10, which were considered to have no significant effect on the *in-situ* diffraction measurement, especially concerning the grain number statistic. It is to mention that the adjustment of grain size by using thermomechanical treatments was restricted for the ZX10 alloy due to its strong tendency to hot cracking during the rolling process. Fig. 5.1.2 illustrates the SEM (BSE, backscattered electron) micrographs of the examined sheets. The secondary phases that can be recognized by different contrast to the matrix are homogeneously distributed in all examined alloys, while a higher amount of the secondary phases is observed in the Nd and Ca containing alloys in comparison to the ZK10 sheet.

The recalculated $\{10\bar{1}0\}$ and (0002) pole figures obtained from the XRD measurements of the annealed sheets are shown in Fig 5.1.3. The ZK10 shows a strong texture with the majority of the grains having their c-axis parallel to the ND, so-called basal type texture, and a similar angular distribution towards the RD and TD. The $\{10\bar{1}0\}$ planes are orientated with a rotational distribution around the ND. The max pole density of the (0002) pole figure of the ZK10 is $P_{\text{max}} = 11$ m.r.d (multiple of a random distribution), which is the strongest intensity in the examined sheets. Such texture type is well acknowledged as a representative texture in a conventional Mg alloy sheet, e.g. AZ31 [6-8]. In contrast, the Nd or Ca containing sheets show a weak texture with a basal pole spread, which can be characterized in two different modes. First, a basal pole split toward the RD is observed in N05 and X05. Second, the basal pole broadening toward the TD is observed in ZN10 and ZX10. The corresponding $\{10\bar{1}0\}$ pole figures indicate a preferential alignment of the $\langle 10\bar{1}0 \rangle$ axis in the RD and a weak rotational distribution

around the ND. This type of texture development, e.g. texture modification with a basal pole broadening from the ND, has been reported mainly in the RE or Ca containing Mg alloy sheets [6, 16, 17, 21, 22]. The max intensities of (0002) pole figure are $P_{\max} = 5.1$ for N05, 5.6 for X05, 2.7 for ZN10, and 3.2 for ZX10, respectively, as shown in Fig. 5.1.3.

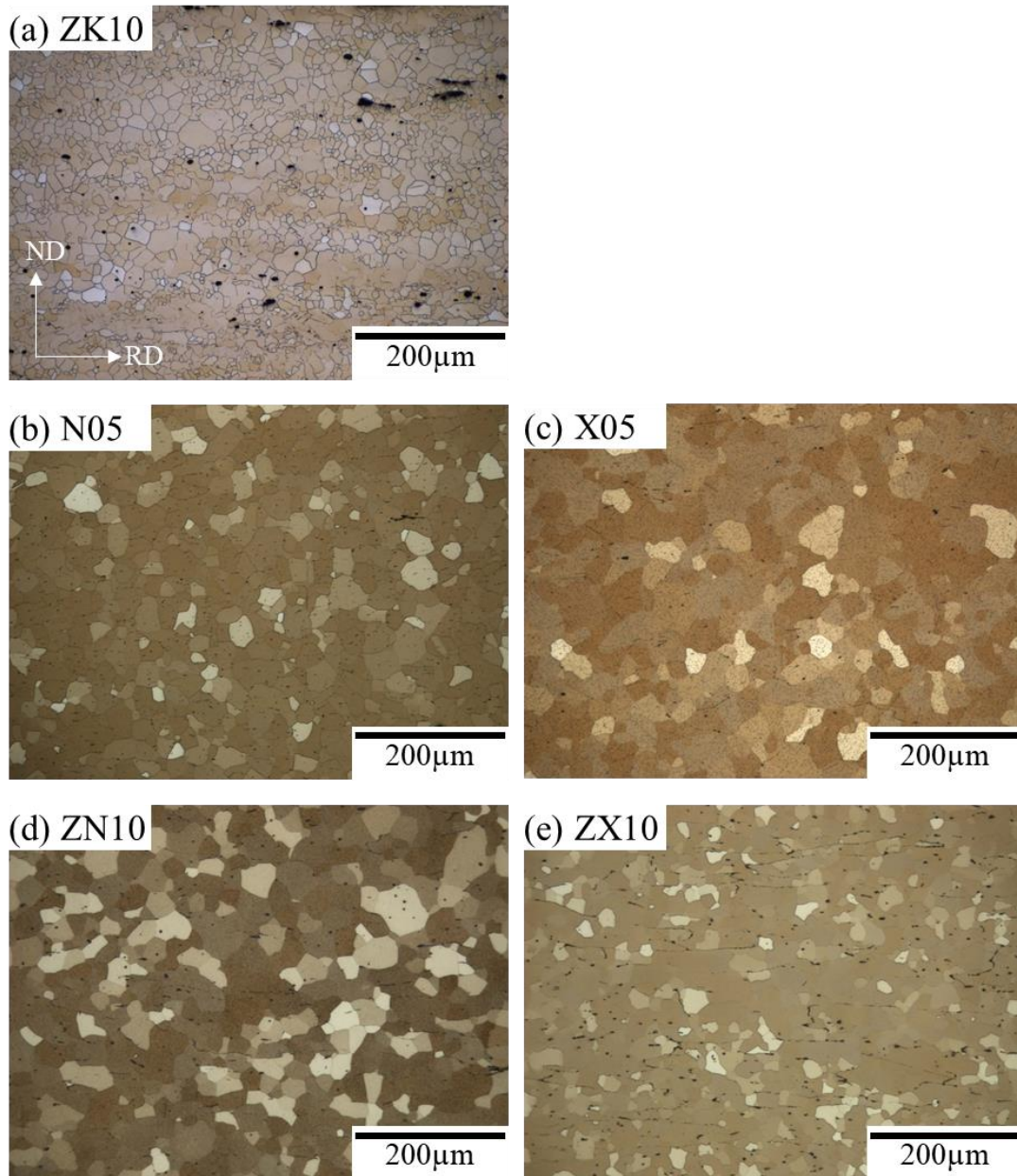


Fig. 5.1.1 Initial optical micrographs after annealing for the rolled sheets obtained from the longitudinal sections of (a) ZK10, (b) N05, (c) X05, (d) ZN10, and (e) ZX10

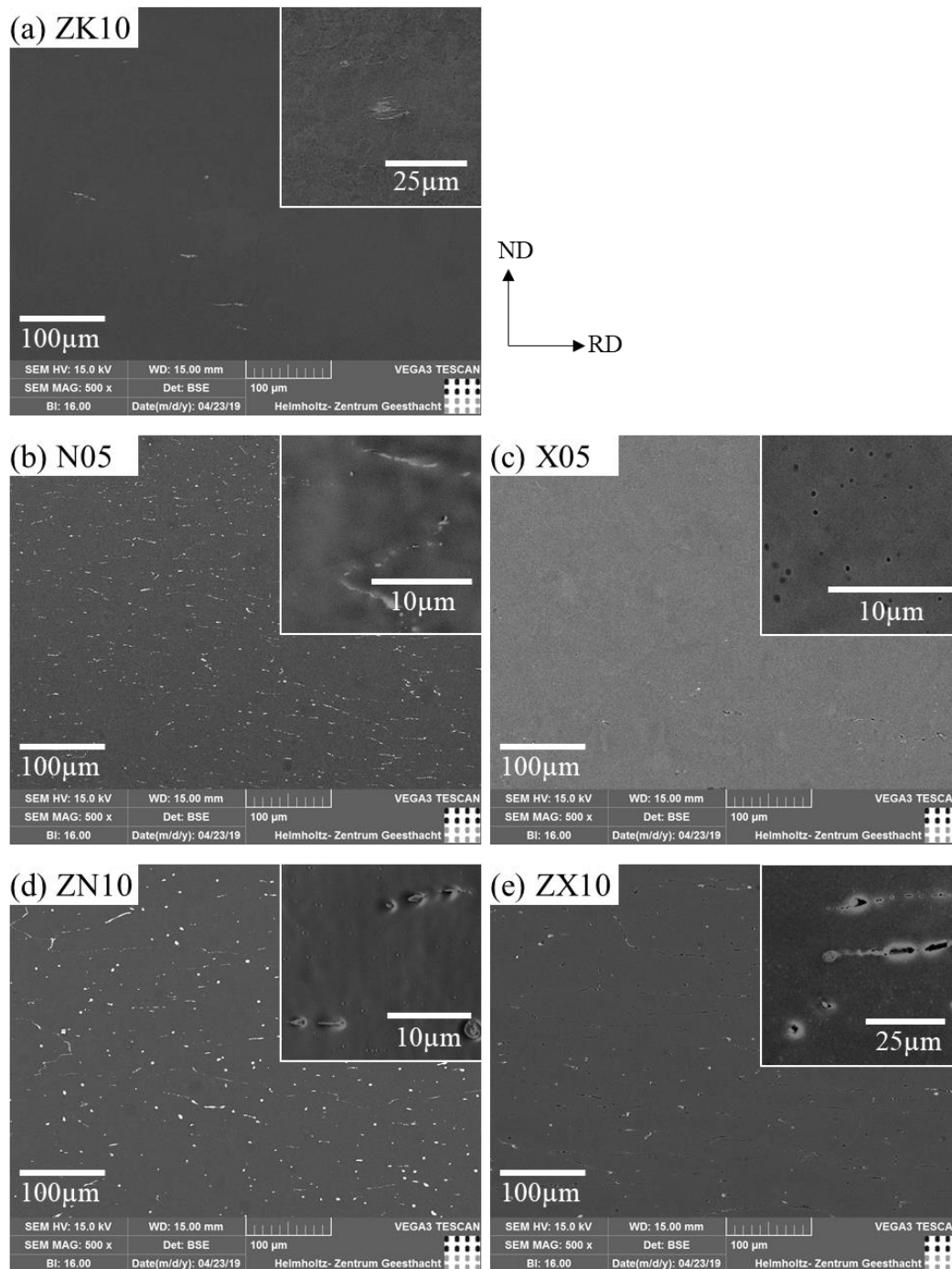


Fig. 5.1.2 SEM (BSE) micrographs of the examined sheets: (a) ZK10, (b) N05, (c) X05, (d) ZN10, and (e) ZX10. The secondary phases at higher magnification are shown in the insets.

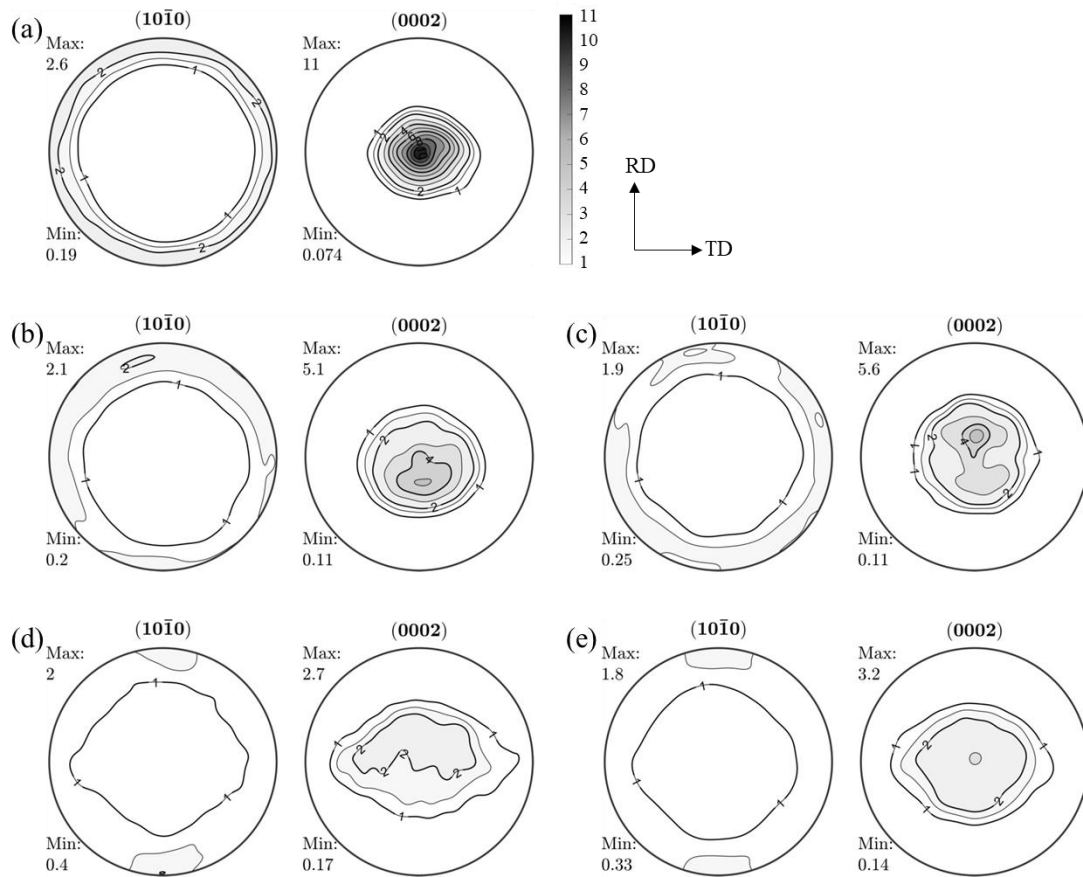


Fig. 5.1.3 Recalculated $\{10\bar{1}0\}$ and (0002) pole figures after annealing treatment of all examined sheets observed by X-ray diffraction: (a) ZK10, (b) N05, (c) X05, (d) ZN10, and (e) ZX10. Contour levels = 1.0, 1.5, 2.0, 3.0, 4.0, ..., 11.0 m.r.d.

5.2 Texture development and dislocation activity in different Mg sheets

This section handles the *in-situ* tensile test at RT as a part of the experimental series at various temperatures. The focus of the *in-situ* experiments at RT was given to the investigation of the deformation mechanisms, rather than thermally activating recrystallization or recovery processes. The obtained results from the *in-situ* diffraction experiments at synchrotron will be discussed in terms of the texture development and predominant deformation modes under tensile loading.

5.2.1 Results: *in-situ* texture measurement under tension

Mechanical properties

The stress-strain curves acquired from the continuous tensile loading at the constant strain rate, $1.5 \times 10^{-4} \text{ s}^{-1}$, are shown in Fig. 5.2.1. The stress-strain curves acquired from the continuous loading and the *in-situ* experiments match well in all cases, even though the stress relaxation occurs during the collection of diffraction patterns of the *in-situ* measurements. The similarities of the flow curves between the continuous loading and the *in-situ* measurements ensure the reliability of the tensile behaviors determined from both test schemes, as described in Chapter 4.2.1 and Fig. A.1 in the appendix. The plastic strain concurrent with the stress relaxation is almost negligible, about 10^{-5} , so that the stress relaxation has no significant influence on the deformation behavior, including the flow curve, the work hardening behavior, and texture developments [28, 67].

The corresponding mechanical properties are listed in Table 5.2.1. In the RD samples, the yield strength of the N05 (118 MPa) and ZN10 (113 MPa) are similar to that of ZK10 (116 MPa), whereas those of the X05 (105 MPa) and ZX10 (109 MPa) are relatively low. In the TD samples, the binary N05 (109 MPa) and X05 (108 MPa) alloys show a similar YS with ZK10 (107 MPa), while the ternary alloys, ZN10 (83 MPa) and ZX10 (93 MPa), show distinctly lower YS compared to that of the other three sheets.

It is to mention that the YS values in the TD sample are lower than those in the RD samples, and their difference is noticeable in ZN10 and ZX10. In the case of the ultimate tensile strength (UTS), unlike the YS, there is no significant difference between both loading directions. The binary alloys, N05 (171 MPa) and X05 (177 MPa), show the lowest values of UTS in both loading directions, and the ternary alloys, ZN10 (188 MPa) and ZX10 (200 MPa), show relatively higher UTS in both loading directions than that of ZK10 (190 MPa).

It is generally acknowledged that the difference between YS and UTS (UTS-YS) represents the work hardening ability. As shown in Fig. 5.2.2 (f), the ZN10 and ZX10 alloys with low YS and relatively high UTS show relatively larger work hardening ability than other sheets in both loading directions. The N05 and X05 show a smaller work

hardening behavior than the ZK10. The examined sheets show a higher work hardening ability in TD loading due to the relatively low YS compared to the RD loading, excluding the X05 that indicates a premature fracture. The difference in the working hardening ability according to the loading direction, i.e. mechanical anisotropy, is more apparent in the ZN10 and ZX10 due to the noticeably low YS in the TD. The higher working hardening ability observed during the TD loading of the ternary alloys can be understood as a result of an easier activation of slip systems with a high Schmid factor during the TD loading than RD loading.

It should be mentioned that the examined sheets except for X05 show a large strain, higher than 20%, which enables to conduct the *in-situ* experiments with sufficiently collected data sets to trace the active deformation modes and texture development. Meanwhile, the *in-situ* experiments of the X05 with a premature fracture were conducted within a restricted range, especially for the TD loading with the fracture strain of $\epsilon = 5\%$.

Table 5.2.1 Tensile properties in the RD and TD of the examined sheets at RT (YS: yield strength (MPa), UTS: ultimate tensile strength (MPa), and FS: fracture strain (%))

Alloy	RD loading				TD loading			
	YS	UTS	FS	UTS-YS	YS	UTS	FS	UTS-YS
ZK10	116	190	20	74	107	192	14	85
N05	118	171	31	53	109	170	28	61
X05	105	177	12	72	108	160	5	52
ZN10	113	188	31	75	83	181	23	98
ZX10	109	200	29	91	94	197	24	103

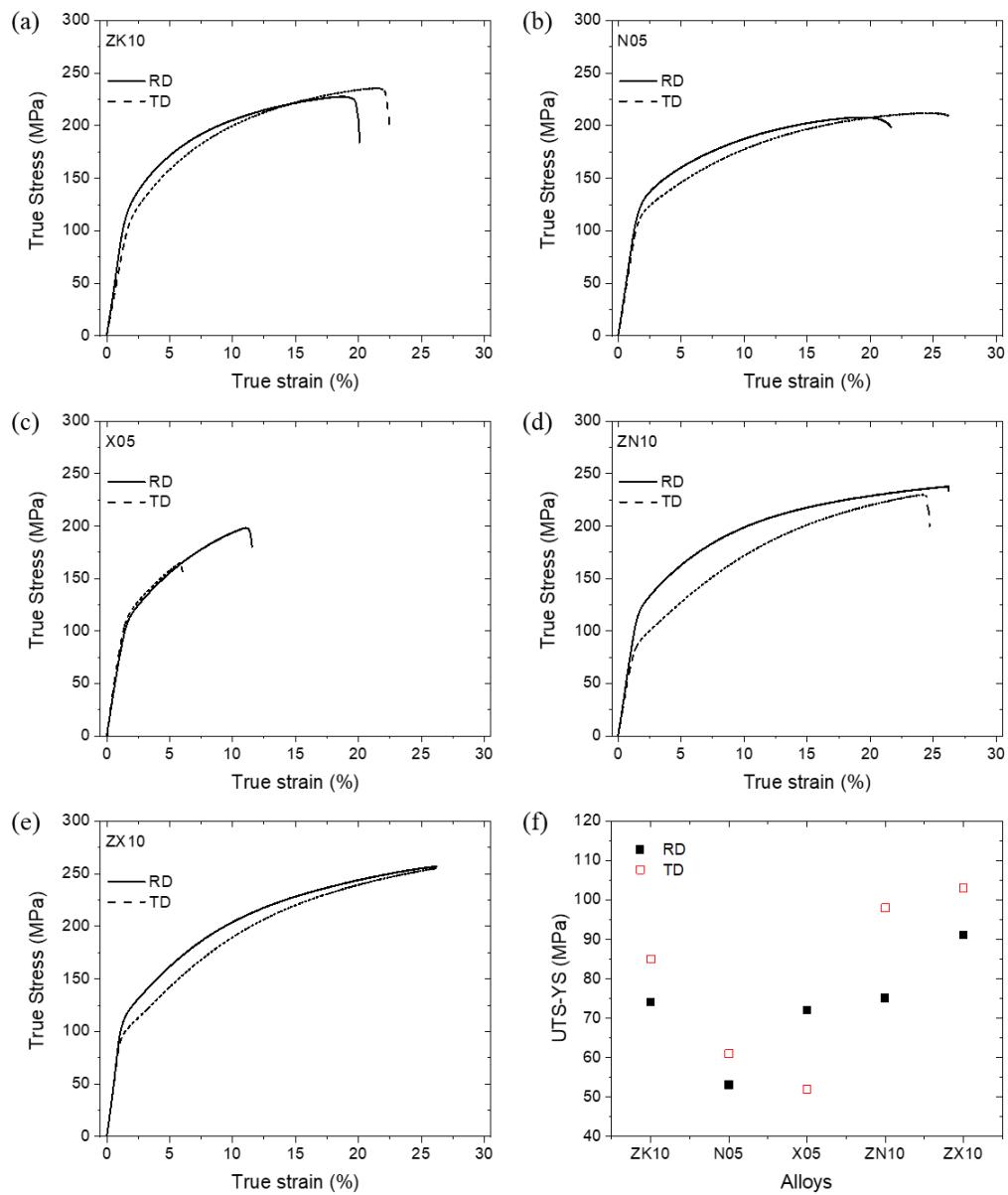


Fig. 5.2.2 True stress-strain curves during the tensile tests along the RD and TD at RT of all examined sheets; (a) ZK10, (b) N05, (c) X05, (d) ZN10, (e) ZX10, and (f) UTS-YS.

Texture developments

The $\{10\bar{1}0\}$ and (0002) pole figures measured at $\varepsilon = 5\%$ and 15% during the *in-situ* texture measurements under the tensile loading along the RD and TD are presented in Figs. 5.2.3 and 5.2.4, respectively. The strain values of $\varepsilon = 5\%$ and 15% are selected in the figures, as a characteristic strain of the stress-strain curve: the strain of 5% corresponds to the point of the beginning of plastic deformation, while the measurement at $\varepsilon = 15\%$ stands for the strain hardening stage. The initial textures ($\varepsilon = 0\%$) of tensile samples under different experimental conditions were considered to be the same as the texture of each sheet, as shown in Fig. 5.1.3. It should be mentioned that the strong basal pole at the ND associated with the coarse grains is observed in the X05 sheet, Fig. 5.2.4 (c), which can also contribute to the premature fracture.

As shown in Fig. 5.2.3, the intensities of the $\{10\bar{1}0\}$ and (0002) pole figures slightly increase with deformation degree, also during further deformation above $\varepsilon = 15\%$, in all examined sheets. In the RD samples, the (0002) pole figure at $\varepsilon = 5\%$ of the ZK10 does not show a significant change compared with the initial condition, while the N05, X05, ZN10, and ZX10 show a broadening of basal pole perpendicular to the LD. With further loading to $\varepsilon = 15\%$, the ZK10 forms that the basal pole is concentrated in the ND with a slight broadening perpendicular to the LD, which accompanies with the strengthening of the $\langle 10\bar{1}0 \rangle$ in the LD with its equivalent 6-fold poles, as shown in the $\{10\bar{1}0\}$ pole figure. In the other sheets, the strengthening of the $\langle 10\bar{1}0 \rangle$ pole in the LD is also found, but its equivalent poles at the periphery of the $\{10\bar{1}0\}$ pole figure exhibit a weaker intensity than that in the ZK10. This relates to the broadening of the $\langle 0001 \rangle$ pole perpendicular to the LD, i.e. the development of $\langle 10\bar{1}0 \rangle$ fibre parallel to the LD and the accompanying rotation of the basal pole around the fibre axis. Such characteristics of the texture developments are more pronounced in ZN10 and ZX10. That is, the forming tendency of the basal pole broadening perpendicular to the LD is observed in all examined alloys, but its formation degree as a function of the tensile strain is different between the alloys.

Fig. 5.2.4 shows the $\{10\bar{1}0\}$ and (0002) pole figures measured at $\varepsilon = 5\%$ and 15% of the tensile strain in the TD. The TD samples indicate a similar tendency of the texture

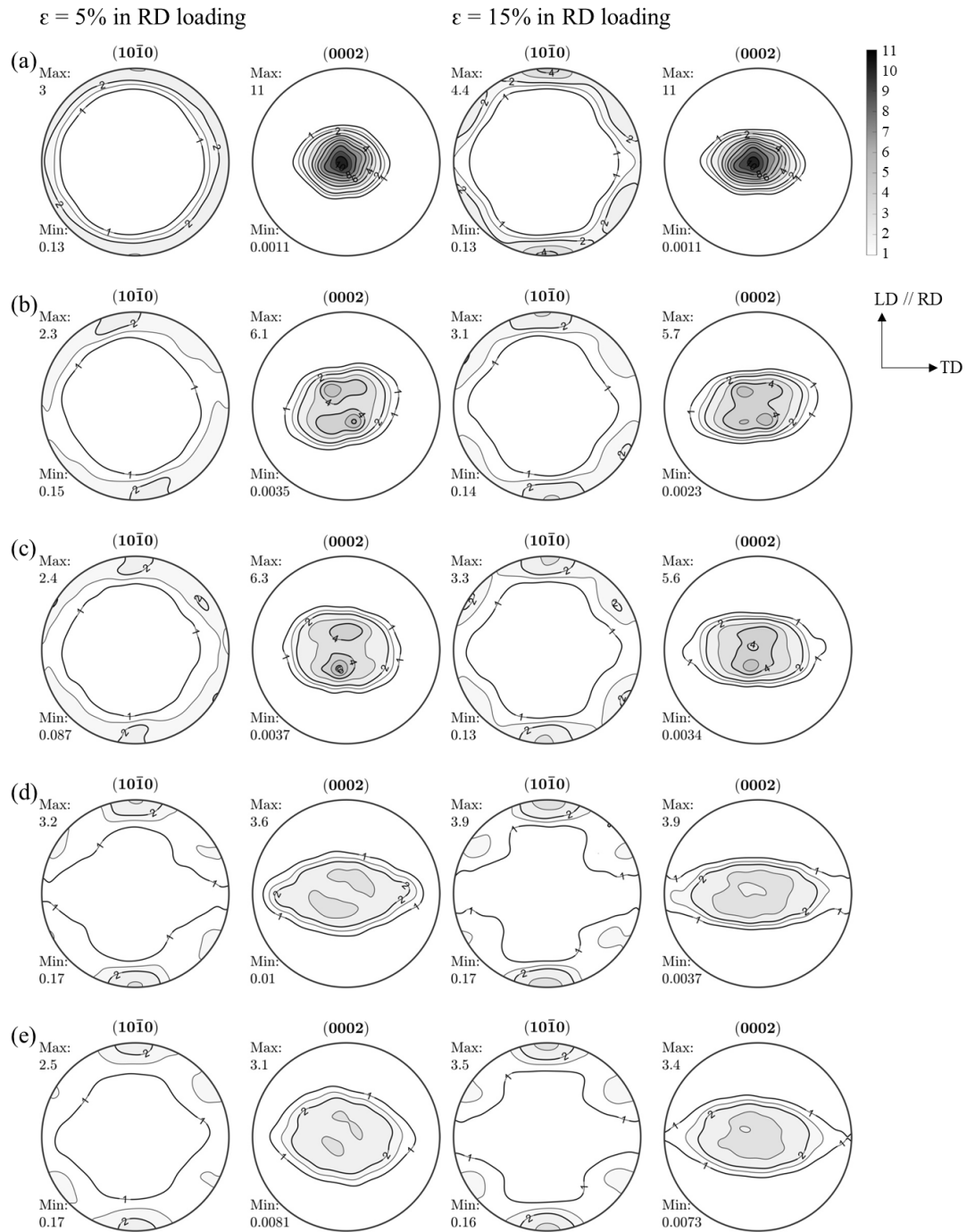


Fig. 5.2.3 $\{10\bar{1}0\}$ and (0002) pole figures of tensile sample deformed to at $\varepsilon = 5\%$ and 15% along the RD of the examined sheets: (a) ZK10, (b) N05, (c) X05, (d) ZN10, and (e) ZX10. Contour levels = 1.0, 1.5, 2.0, 3.0, 4.0, ..., 11.0 m.r.d.

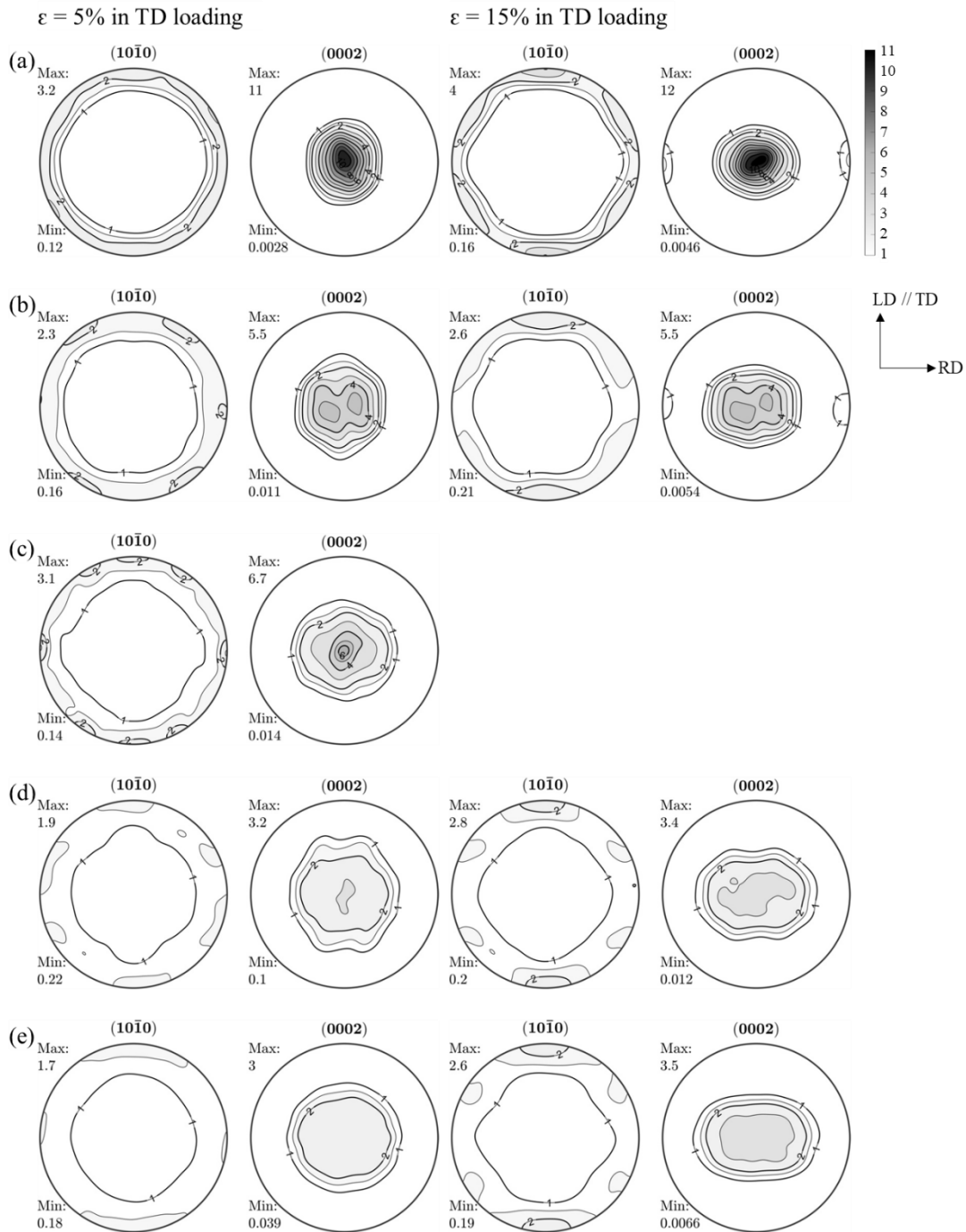


Fig. 5.2.4 $\{10\bar{1}0\}$ and (0002) pole figures of tensile sample deformed to at $\varepsilon = 5\%$ and 15% along the TD of the examined sheets: (a) ZK10, (b) N05, (c) X05, (d) ZN10, and (e) ZX10. The pole figure of the X05 in TD loading does not show at $\varepsilon = 15\%$ due to the premature fracture. Contour levels = 1.0, 1.5, 2.0, 3.0, 4.0, ..., 11.0 m.r.d.

development during the tensile loading to that observed in the RD samples aforementioned, e.g. basal pole broadening perpendicular to the LD. However, the formation kinetics of the basal pole spread is slower than the RD samples because of the rotated initial texture in the TD samples. These results indicate that the different initial textures according to the loading directions do not contribute to changing the intrinsic tendency of texture development in each sheet, but the initial texture has an influence on the texture development degree at the certain strain. In other words, the active deformation modes are identical in the examined alloys, e.g. dislocation slip systems resulting in qualitatively similar texture development, but the significances of each mode are different between the alloys.

5.2.2 Results: variation of dislocation activities

The activities of the dislocation slip systems during tensile deformation were evaluated by using the CMWP fitting procedure at selected strain levels, $\varepsilon = 2\%$, 5% , 10% , 15% , and 20% . The results obtained from the CMWP analysis for all examined sheets are listed in Table A.1 – A.3 in the appendix.

Fig. 5.2.5 displays the overall dislocation densities and their differences between the RD and TD loadings. The overall dislocation densities of the examined sheets increase with the applied strain in both directions. This indicates that the strain is mainly accommodated by increasing dislocation glide in all cases. In the RD loading, the ZK10 shows a gradual increase in overall dislocation density from $2.56 \times 10^{14} \text{ m}^{-2}$ to the max density of $4.90 \times 10^{14} \text{ m}^{-2}$ during the deformation. The N05 and X05 show a higher increase in the overall dislocation density than the ZK10 with the max densities of $5.61 \times 10^{14} \text{ m}^{-2}$ and $5.91 \times 10^{14} \text{ m}^{-2}$, respectively. The ZN10 and ZX10 show the highest value in the overall dislocation density with the maximum densities of $6.61 \times 10^{14} \text{ m}^{-2}$ and $6.84 \times 10^{14} \text{ m}^{-2}$. The ZK10, N05, and X05 indicate no distinct difference between the RD and TD loading, but in the ZN10 and ZX10. The ZN10 and ZX10 show a lower overall dislocation density with 5.80 and $6.28 \times 10^{14} \text{ m}^{-2}$ during the TD loading compared to the RD loading. As shown in Fig. 5.2.5 (c), the difference in the dislocation activities between both loading

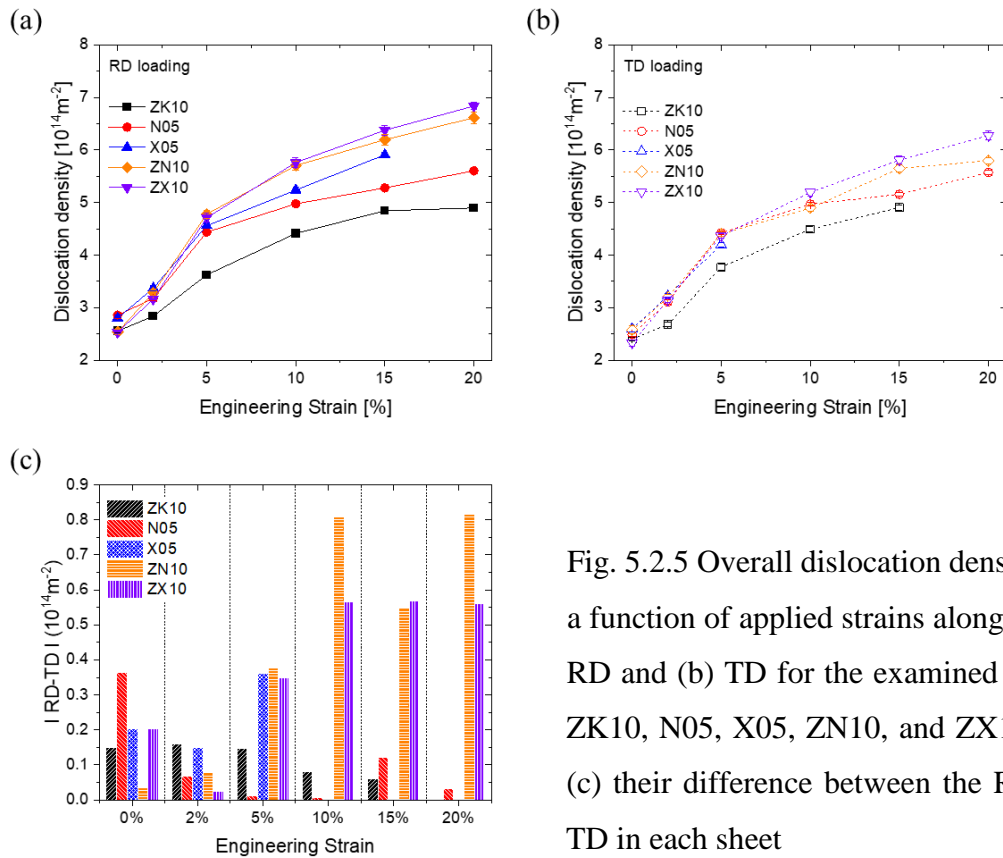


Fig. 5.2.5 Overall dislocation densities as a function of applied strains along the (a) RD and (b) TD for the examined sheets: ZK10, N05, X05, ZN10, and ZX10, and (c) their difference between the RD and TD in each sheet

directions increases with strain in the ZN10 and ZX10, while the difference becomes smaller with increasing strain in the other sheets.

The overall dislocation densities were analyzed by classifying the Burgers vectors, $\langle a \rangle$, $\langle c \rangle$, $\langle c+a \rangle$ types to determine separately the activities of different dislocation modes. The obtained results for the $\langle a \rangle$ and $\langle c+a \rangle$ dislocations as a function of the strain are shown in Fig. 5.2.6. The $\langle c \rangle$ dislocations have the lowest density among the three dislocation modes with approximately $0.5 \times 10^{14} \text{m}^{-2}$ that is unchanged at the whole strain range. That is, the $\langle c \rangle$ dislocation plays a minor role in all the examined cases, and the $\langle c \rangle$ dislocations are excluded from presenting in Fig. 5.2.6. The evaluation of the active dislocation modes of the X05, especially in the TD loading, is limited due to the strong intensities of a certain diffraction peak (in relation to the strong texture and coarse grains, shown in Fig. 5.2.4) and the premature fracture. Accordingly, the dislocation modes could be evaluated only at the low strain of $\varepsilon = 2\%$ and 5% . It is to note that the strong texture and coarse grains cause a significant difference in the peak intensity from the theoretical

diffraction peaks and, therefore, suffer the whole profile analysis in the CMWP fitting procedure. Moreover, the internal stress within lattice by elastic deformation and asymmetric grain shape at high strain can be other influencing factors on the CMWP fitting procedure.

The $\langle a \rangle$ dislocations, which are known as an easier slip system due to its relatively low CRSS, play an important role in the strain accommodation with the densities higher than $3.3 \times 10^{14} \text{ m}^{-2}$ in all the examined sheets. Besides, a relatively high activity of $\langle c+a \rangle$ dislocations is found with densities higher than $1.2 \times 10^{14} \text{ m}^{-2}$. With increasing strain, the $\langle a \rangle$ and $\langle c+a \rangle$ dislocations become dominating, while their densities vary in dependence on the alloying elements and loading directions. This result is similar to that of the overall

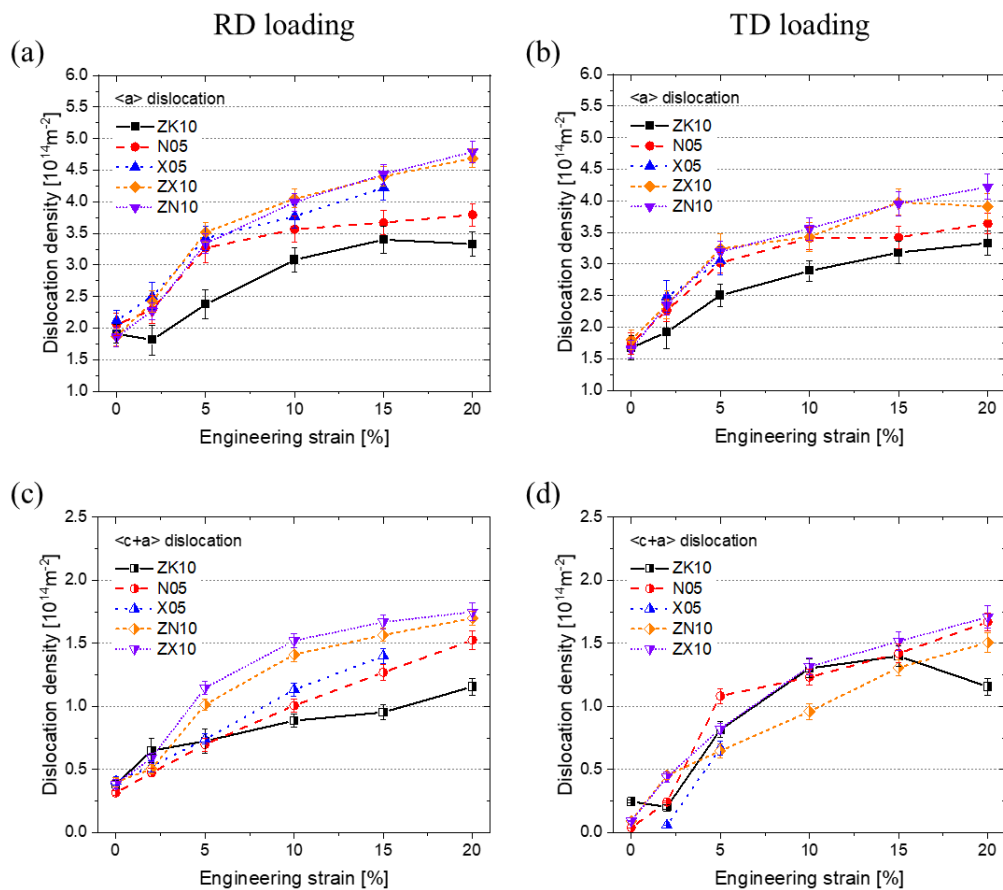


Fig. 5.2.6 Dislocation densities classified according to the Burgers vectors, (a), (b) $\langle a \rangle$ and (c), (d) $\langle c+a \rangle$ types, as a function of applied strains along the RD (left) and TD (right) for the examined sheets: ZK10, N05, X05, ZN10, and ZX10.

dislocation density. In other words, the overall dislocation densities in each sheet are closely correlated with the activities of $\langle a \rangle$ and $\langle c+a \rangle$ dislocations.

The ZK10 shows the lowest $\langle a \rangle$ dislocations densities with $3.33 \times 10^{14} \text{ m}^{-2}$ and $3.18 \times 10^{14} \text{ m}^{-2}$ in the RD and TD loading, respectively. Other sheets show a similar increase of the dislocation densities, with approximately $3.02 \sim 3.52 \times 10^{14} \text{ m}^{-2}$, at $\varepsilon = 5\%$ in both loading directions. Again, the amount of the density increase differs between the alloys during the further deformation. In the RD loading, the X05 shows a slightly higher density than that of the N05, with $4.22 \times 10^{14} \text{ m}^{-2}$ and $3.80 \times 10^{14} \text{ m}^{-2}$, respectively. The ZN10 and ZX10 show the highest density of $\langle a \rangle$ dislocations with $4.69 \times 10^{14} \text{ m}^{-2}$ and $4.79 \times 10^{14} \text{ m}^{-2}$. The N05, ZN10, and ZX10, in the TD loading, show similar increasing behavior of the $\langle a \rangle$ dislocation densities up to 10% strain, while the ZN10 and ZX10 show a slightly higher density after 10% strain. The N05 has the max density of $3.64 \times 10^{14} \text{ m}^{-2}$, and the ZN10 and ZX10 have the max densities of $3.91 \times 10^{14} \text{ m}^{-2}$ and $4.22 \times 10^{14} \text{ m}^{-2}$, respectively. The differences in the activities of $\langle a \rangle$ dislocations between the sheets are more pronounced in the RD loading than in the TD loading.

Figs. 5.2.6 (c) and (d) illustrate the activities of the $\langle c+a \rangle$ dislocations during the RD loading. The ZK10, N05 and X05 show a similar density of $0.70 \times 10^{14} \text{ m}^{-2}$, up to $\varepsilon = 5\%$. With increasing strain, the N05 and X05 show a slight increase of the densities up to $1.40 \times 10^{14} \text{ m}^{-2}$ and $1.53 \times 10^{14} \text{ m}^{-2}$, while the ZK10 has the lowest density of $1.16 \times 10^{14} \text{ m}^{-2}$. The ZN10 and ZX10 show the highest densities of $1.70 \times 10^{14} \text{ m}^{-2}$ and $1.75 \times 10^{14} \text{ m}^{-2}$. These distinct behaviors between the alloys diminish during the TD loading. The ZK10 shows a large increase of the $\langle c+a \rangle$ dislocations up to $\varepsilon = 10\%$ in TD loading. The ZN10 and ZX10 indicate the gradual increase of $\langle c+a \rangle$ dislocation densities to $1.51 \times 10^{14} \text{ m}^{-2}$ and $1.71 \times 10^{14} \text{ m}^{-2}$. The density of $\langle c+a \rangle$ dislocations shows a relatively small difference between the alloys during the TD loading.

Fig. 5.2.7 presents the variation of the ratio of the basal $\langle a \rangle$ and non-basal $\langle a \rangle$ dislocations ($\rho_{\text{basal } \langle a \rangle}$ and $\rho_{\text{non-basal } \langle a \rangle}$) to the overall dislocation densities (ρ_{total}), i.e., $\rho_{\text{basal } \langle a \rangle} / \rho_{\text{total}}$ and $\rho_{\text{non-basal } \langle a \rangle} / \rho_{\text{total}}$, with increasing strain along the RD and TD. The classified densities of basal $\langle a \rangle$ and non-basal $\langle a \rangle$ dislocation for examined sheets are listed in Table A.3 in the appendix. It is well known that the basal $\langle a \rangle$ slip mostly takes over the strain accommodation in Mg and its alloys [29, 63, 102], because

the basal plane is a closed packed plane in correlation with the c/a ratio. However, the present experimental results show a high ratio of non-basal $\langle a \rangle$ dislocations, $\rho_{non-basal \langle a \rangle} / \rho_{total} > 0.3$, for all the examined sheets in the both loading directions, in Fig. 5.2.7. With increasing strain, the ZK10 indicates the increasing non-basal $\langle a \rangle$ dislocations, and the decrease in basal $\langle a \rangle$ dislocations by 0.05 ~ 0.06 in the RD and TD loading. The ratio of non-basal $\langle a \rangle$ dislocations decreases at the early deformation stage,

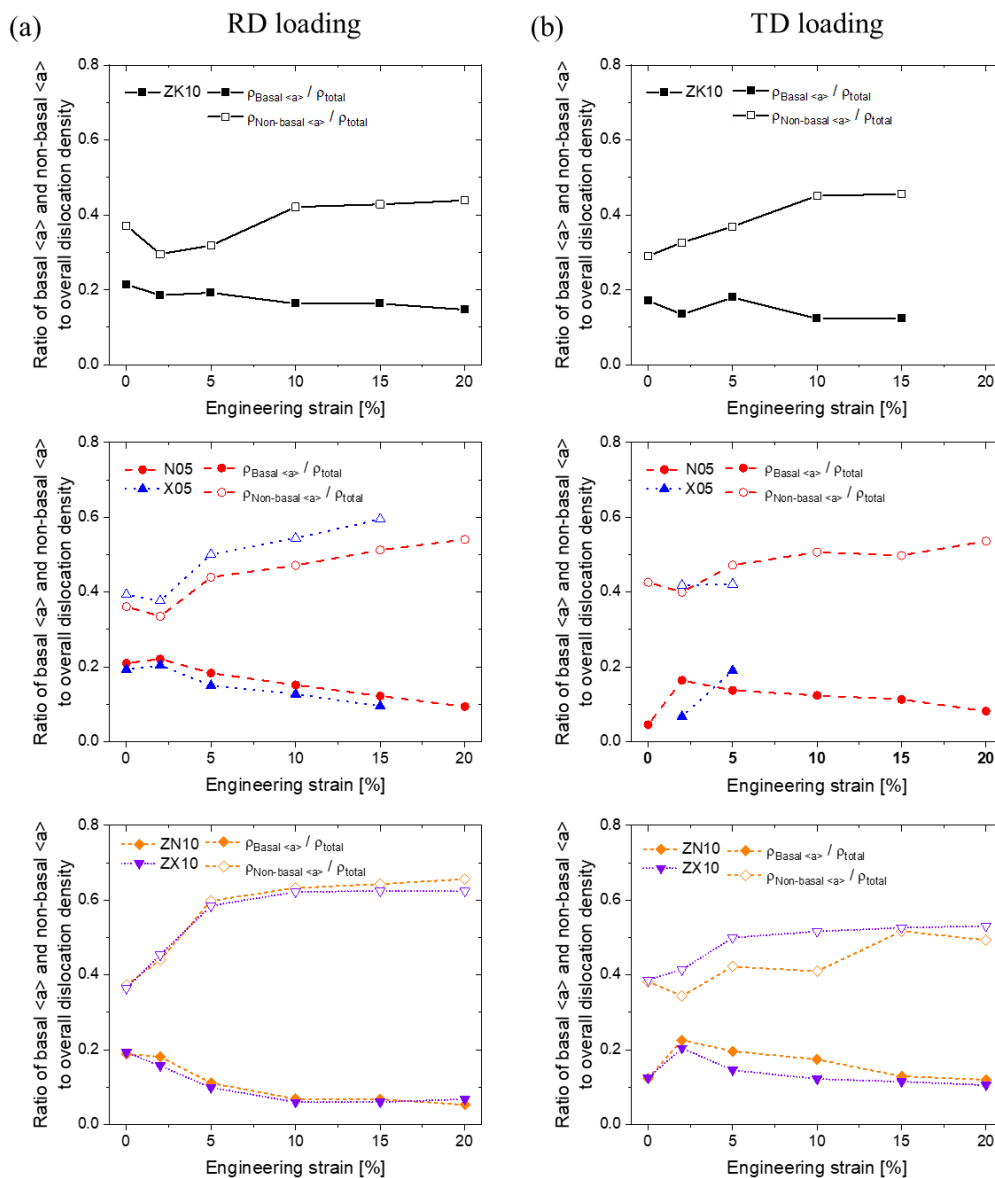


Fig. 5.2.7 The ratio of basal (solid) and non-basal $\langle a \rangle$ (open) dislocations to the overall dislocation as a function of applied strains along the (a) RD and (b) TD for the examined sheets: ZK10, N05, X05, ZN10, and ZX10

$\varepsilon = 2\%$, during the RD loading (0.37 to 0.30), but not in the TD loading (0.29 to 0.33). With increasing strain, the ratio of non-basal $\langle a \rangle$ dislocation increases up to 0.44 and 0.46 during the RD and TD loading, respectively. A similar curve in the ratio of non-basal $\langle a \rangle$ dislocations to that of the ZK10 is shown during the RD loading of the N05 and X05, i.e. concave shape at the early deformation stage, while that of basal $\langle a \rangle$ dislocations shows a convex-shaped curve. During the TD loading of the N05 and X05, the ratio of basal and non-basal $\langle a \rangle$ dislocations are similar to those of the RD loading. It is to note that the N05 and X05 show a higher ratio of non-basal $\langle a \rangle$ dislocation and a lower ratio of basal $\langle a \rangle$ dislocation compared to the ZK10. The highest ratio of non-basal $\langle a \rangle$ dislocations is observed in the RD loading of the ZN10 and ZX10. While the ratio of non-basal $\langle a \rangle$ dislocations increases from 0.35 to 0.65 during the RD loading of the ZN10 and ZX10, the ratio of basal $\langle a \rangle$ dislocation decreases from 0.19 to 0.05. This tendency is less pronounced during the TD loading, while the ratio of basal $\langle a \rangle$ dislocation increases at the early deformation stage, from 0.12 to 0.20. The ratio of basal and non-basal $\langle a \rangle$ dislocations in the ZN10 and ZX10 are similar to those in the N05.

As aforementioned, the prismatic $\langle a \rangle$ and pyramidal $\langle a \rangle$ dislocation were accounted as the non-basal $\langle a \rangle$ dislocations in CMWP analysis of this work. Non-basal $\langle a \rangle$ dislocations have been usually considered to be only prismatic $\langle a \rangle$ dislocation. Recently the activity of pyramidal $\langle a \rangle$ dislocation and its importance for strain accommodation have been reported, e.g. tracing of individual grains of a Mg - 3%Y alloy during the deformation by using an *in-situ* 3D X-ray experiment [43]. Thus, a more detailed analysis of prismatic $\langle a \rangle$ and pyramidal $\langle a \rangle$ dislocations is required to determine their impacts on the deformation behavior of the examined alloys. The activities of prismatic and pyramidal $\langle a \rangle$ dislocations were qualitatively evaluated by considering the local misorientation within individual grains, i.e. IGMA analysis of the EBSD measurement. This analysis enables to identify which of the non-basal $\langle a \rangle$ dislocations are predominant via evaluation of the preferred axes of lattice rotation within the grains, so-called Taylor axes. The EBSD orientation maps from the tensile samples deformed to $\varepsilon = 10\%$ are presented in Fig. 5.2.8. The ZK10 deformed in the RD shows the deformed structure in the local deformation area, such as a shear or deformation band along the white dash line marked, whereas the other cases show homogeneously deformed grain structure accompanying the deformed grains and twins. The deformation stored within a grain is

recognized by the intergranular misorientation as a color gradient within a deformed grain in the EBSD orientation map. This color gradient indicates the lattice distortion induced by dislocations accumulated during deformation.

In this work, a grain orientation spread (GOS) higher than 2° was applied to classify the deformed grains from whole measured grains [16, 28, 103], a misorientation angle between 1° and 5° was selected for the IGMA analysis [100]. Fig. 5.2.9 shows the distribution plots of the IGMA of the deformed grains of all examined samples. The corresponding Taylor axes to different dislocations are marked on the plot, e.g. $\langle 10\bar{1}0 \rangle$ for basal $\langle a \rangle$ and pyramidal $\langle c+a \rangle$ slip, $\langle 10\bar{1}2 \rangle$ for pyramidal $\langle a \rangle$ slip, and $\langle 0001 \rangle$ for prismatic $\langle a \rangle$ slip [100, 101]. The IGMA distribution plots were separately evaluated from two groups of grain orientations, i.e. one with their c -axes parallel to the ND (RED-grains) and the other with their c -axes perpendicular to the LD and ND (BLUE-grains), to determine the influence of grain orientation on the slip. The selected grains and their orientations are shown in the $\langle 0001 \rangle$ discrete pole figures in Fig. 5.2.9.

The RD and TD samples in the examined sheets show a concentration of misorientation around $\langle 0001 \rangle$ axis, which corresponds to the preferred activity of prismatic $\langle a \rangle$ slip, while the RD samples of the N05 and X05 show a relatively homogeneous distribution with a slight concentration around $\langle 0001 \rangle$ axis. The results of the IGMA analysis indicate a predominant activation of the prismatic $\langle a \rangle$ slip, among the non-basal $\langle a \rangle$ slip. Even though a slight concentration at the other IGMA distributions, e.g. corresponding to basal $\langle a \rangle$, pyramidal $\langle a \rangle$, and pyramidal $\langle c+a \rangle$ slip are also observed, it is much less in comparison with the prismatic $\langle a \rangle$ slip. It is a good agreement with the results shown in Fig. 5.2.7, where the higher activity of non-basal $\langle a \rangle$ dislocations was found in the examined sheets. The IGMA analysis shows less activity of basal $\langle a \rangle$ slip, despite that this is easily activated with the lowest CRSS value. This controversial result to the theoretical interpretation can be understood by a relatively higher difficulty of basal $\langle a \rangle$ slip, e.g. in comparison to prismatic $\langle a \rangle$ slip since the initial texture and texture evolutions during deformation are not favorable to the basal $\langle a \rangle$ slip. The results of the IGMA analysis are consistent with the results of the CMWP analysis, even though the dislocations activity can be qualitatively shown by IGMA analysis. In other words, the high activation of non-basal $\langle a \rangle$ dislocations (or high ratio of non-basal $\langle a \rangle$ dislocations

to the overall dislocation density), measured in the CMWP analysis, is reasonably attributed to the predominant activity of prismatic $\langle a \rangle$ slip rather than pyramidal $\langle a \rangle$ slip. Moreover, it is worth mentioning that the TD sample of the X05 measured at 4% strain indicates concentration around the $\langle 0001 \rangle$ axis, i.e. a high activation of prismatic $\langle a \rangle$ slip also in the Ca-containing binary alloy.

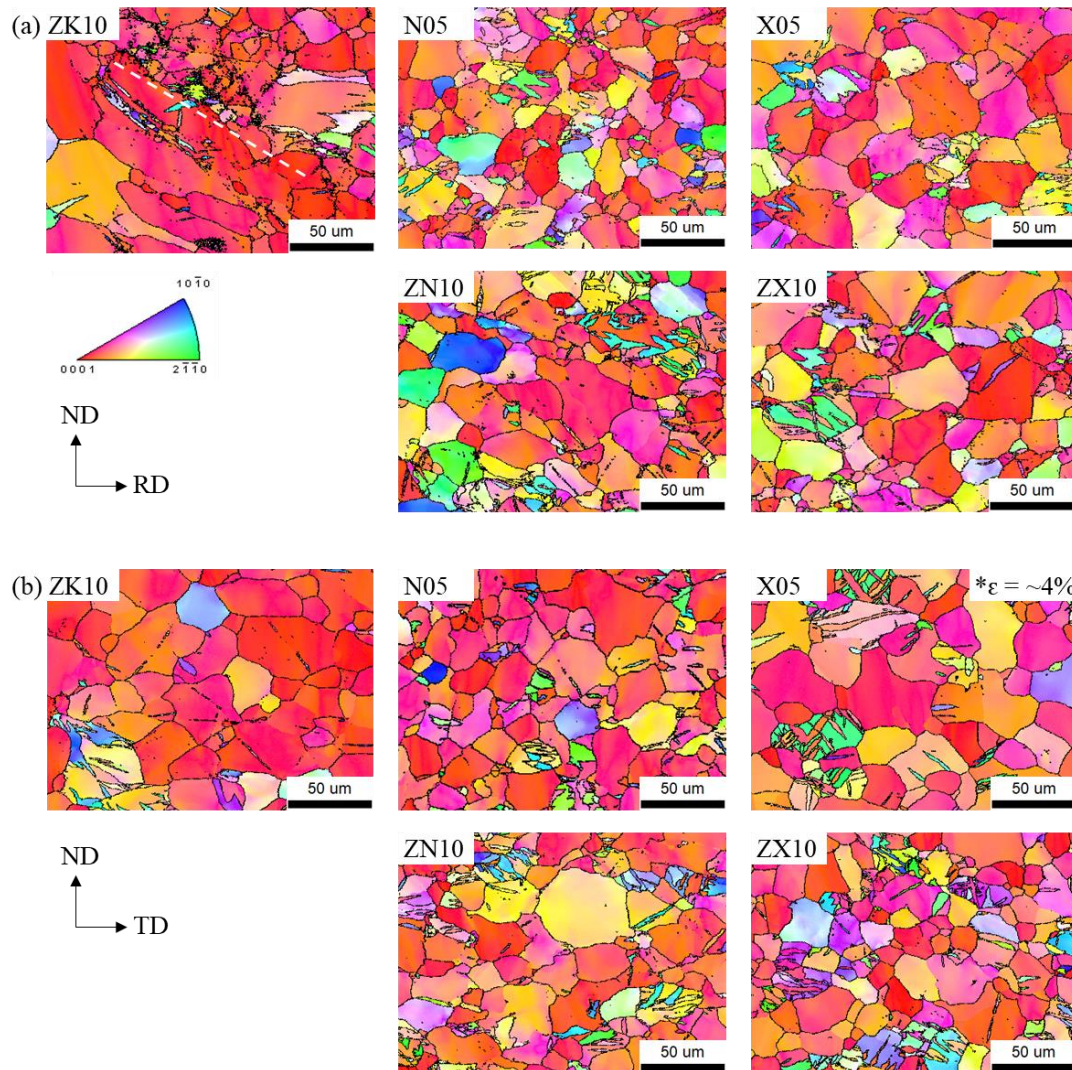


Fig. 5.2.8 EBSD orientation maps of tensile samples deformed to $\varepsilon = 10\%$ in the (a) RD and (b) TD for the examined sheets: ZK10, N05, X05, ZN10, and ZX10. High angle grain boundaries ($\theta > 15^\circ$), are marked with a black line.

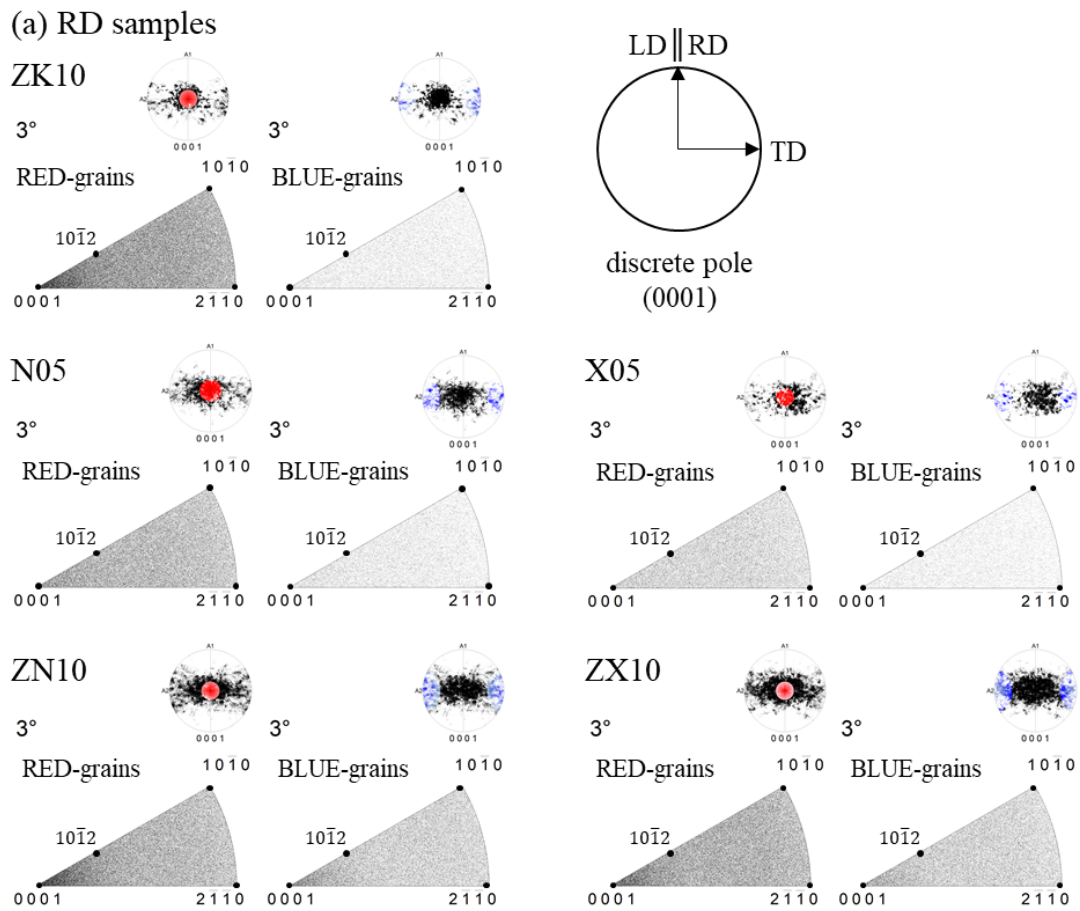


Fig. 5.2.9 IGMA distributions in the deformed grains classified by $GOS > 2^\circ$ depending on the grain orientations (RED- or BLUE-grains) in each sample deformed in the (a) RD and (b) TD to $\varepsilon = 10\%$ for examined sheets: ZK10, N05, X05, ZN10, and ZX10. Exceptively, the TD samples in the X05 showed the IGMA distribution at $\varepsilon = 4\%$. The (0001) discrete pole figures indicating the orientation of the grains selected for the IGMA analysis are inserted. (continue to next page)

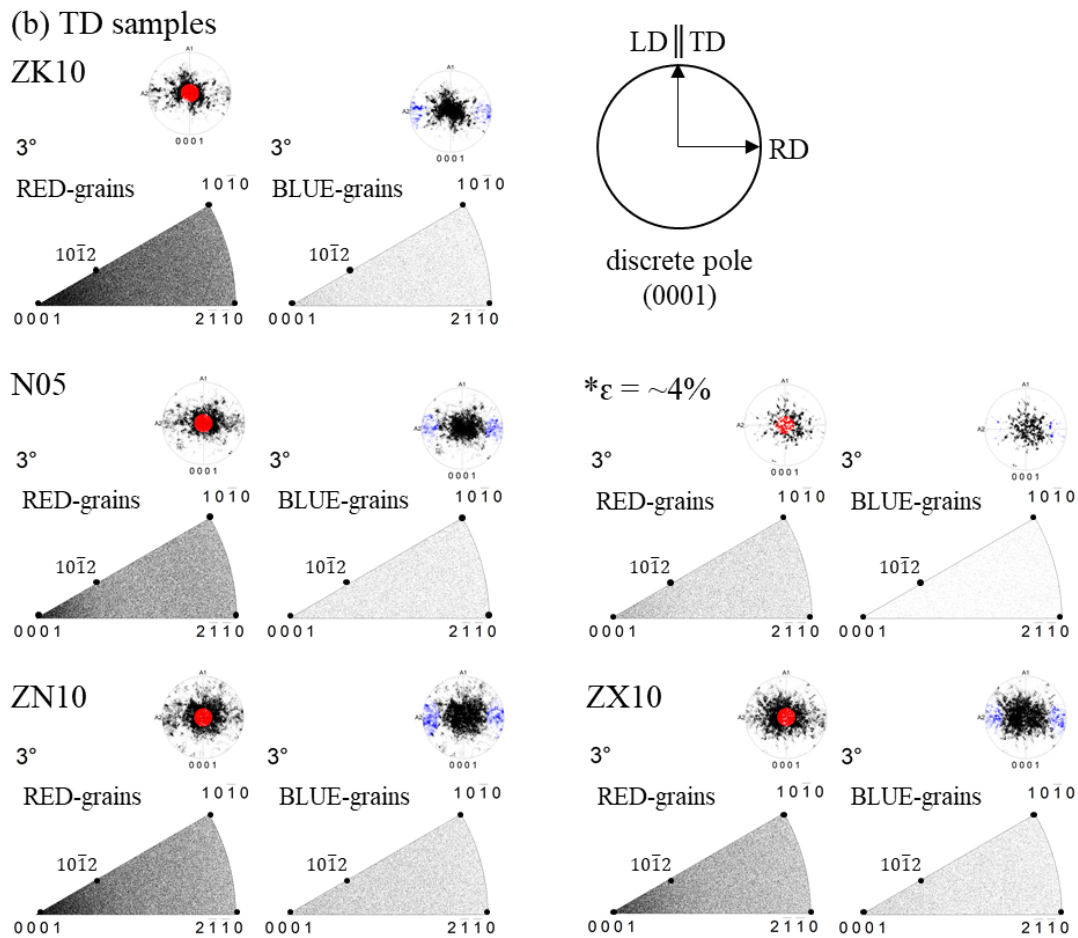


Fig. 5.2.9 continue

5.2.3 Discussion: deformation modes for texture development

The deformation mechanisms are the only factor to change texture development when the influence of recrystallization is ruled out. The main deformation mechanisms in the Mg and its alloys are dislocation slip and twin activation for the strain accommodation. The dislocation densities were investigated by the *in-situ* diffraction experiments combined with the CMWP analysis, where the twin activation was not considered. The twin was investigated by the EBSD observation.

The tendency of texture developments of the examined sheets are similarly determined by the strengthening of the $\langle 10\bar{1}0 \rangle$ pole parallel to the LD and a broadening of the basal pole perpendicular to the LD, described in Chapter 5.2.1.

It has been reported that such texture development is mainly related to the high activation of the prismatic $\langle a \rangle$ slip [28-30]. In this work, the CMWP analysis has indicated the high activations of non-basal $\langle a \rangle$ dislocations, i.e. prismatic $\langle a \rangle$ and pyramidal $\langle a \rangle$ dislocations, for all examined sheets. Furthermore, the IGMA analysis of the EBSD measurements supports a predominant activity of prismatic $\langle a \rangle$ slip among the non-basal $\langle a \rangle$ slip. These results indicate that the prismatic $\langle a \rangle$ slip mainly contributes to the strain accommodation in the examined sheets, irrespective of the initial texture and alloy elements, and further leads to such texture development, which is in good agreement with earlier works [28-30]. Even though the main slip systems do not change with the alloying elements and loading direction, it is clear that the importance of each mode, in terms of the ratio of its density, considerably varies with the alloying elements and loading direction, Fig. 5.2.7. Accordingly, the difference in the deformation textures is shown, Figs. 5.2.3 and 5.2.4. The ZN10 and ZX10 indicate the pronounced development of the basal pole broadening perpendicular to the LD with the highest ratio of non-basal $\langle a \rangle$ dislocations (approximately 0.60). This tendency of the texture development is weaker in the N05 and X05 with a lower ratio of non-basal $\langle a \rangle$ dislocations (approximately 0.50) than in the ZN10 and ZX10, while the tendency is ambiguous in the ZK10 with the lowest ratio of non-basal $\langle a \rangle$ dislocations (approximately 0.40).

The pyramidal $\langle c+a \rangle$ slip has been emphasized as a deformation mode significantly affecting the texture development. The texture development according to the high activity of pyramidal $\langle c+a \rangle$ slip was reported by Agnew et al. [6, 58], based on the crystal plasticity simulation. They presented that a split of the basal pole from ND towards the main loading direction results from the activation of pyramidal $\langle c+a \rangle$ slip. As shown in Fig. 5.2.6, the activities of pyramidal $\langle c+a \rangle$ slip in the examined alloys are in order of ZK10 < N05 and X05 < ZN10 and ZX10. Except for the ZK10, the examined alloys have a weak texture component of basal poles tilted from the ND by 15-20°, that is formed with increasing activation of pyramidal $\langle c+a \rangle$ slip (ratio of ~ 0.20 , $\rho_{pyra. \langle c+a \rangle} / \rho_{total}$) after large deformation, e.g. at $\varepsilon = 20\%$. It is to mention that a clear split of the basal pole

from the ND to the LD is not observed in the present results from the *in-situ* texture measurements. This can be understood from the relatively low fraction of the pyramidal $\langle c+a \rangle$ dislocation, in comparison to the non-basal $\langle a \rangle$ dislocations with the ratio of approximately 0.60. That is, the fraction of the pyramidal $\langle c+a \rangle$ dislocations is insufficient yet to result in a clear split of the basal pole. Likewise, it was observed in [58] that the corresponding texture development disappears by varying the importance of predominant deformation modes. The study showed that the texture component of the basal pole split disappears during tensile deformation of AZ31B sheet as a result of predominant prismatic $\langle a \rangle$ slip with its fraction of 0.7. Besides, it has been known that a higher activation of pyramidal $\langle c+a \rangle$ slip with the reduced CRSS requires the deformation at elevated temperatures.

In the case of basal $\langle a \rangle$ dislocations, the initial texture of the ZK10 is not favorable due to geometrical reasons, i.e. low Schmid factor. Even if the texture is favorable for the basal $\langle a \rangle$ slip, e.g. the tension in the RD of the N05 or in the TD of the ZN10 and ZX10, the activation of basal $\langle a \rangle$ slip is pronounced only at the early deformation stage, while the non-basal $\langle a \rangle$ slip eventually become predominant. This behavior also seems to relate to the texture, which is unfavorable for basal $\langle a \rangle$ slip, evolved during further deformation.

In addition to the slip systems, the twin activity attributes to texture development. For example, the secondary twin attributes to the formation of the RD split component during rolling [6, 76]. The tensile twin attributes to the split of the basal poles in the TD during deformation in AZ31 [22]. The nucleation of randomly oriented grains during recrystallization can be induced at twin boundaries in Mg-Zn-Ca and Mg-Y-RE alloys [104, 105]. The twin activity is investigated by the EBSD measurement of the tensile samples deformed to $\varepsilon = 10\%$, in Fig. 5.2.10. Different types of twin are identified by their misorientation relations, i.e. the $\{10\bar{1}2\}$ tensile twin (red, 86° , $\langle 11\bar{2}0 \rangle$), the $\{10\bar{1}1\}$ compression twin (yellow, 56° , $\langle 11\bar{2}0 \rangle$), and the $\{10\bar{1}1\}\{10\bar{1}2\}$ secondary twin (green, 38° , $\langle 11\bar{2}0 \rangle$), and displayed with different colors. The twin fraction was evaluated from the twin area, as exemplarily illustrated in Fig. 5.2.10 (a). The microstructure contains tensile twins as well as compression and secondary twins. The fraction of tensile twins is approximately 6 ~ 7% in all examined samples, while the compression and secondary

twins show a low fraction below 1%. The twin behavior is similar in all the examined sheets.

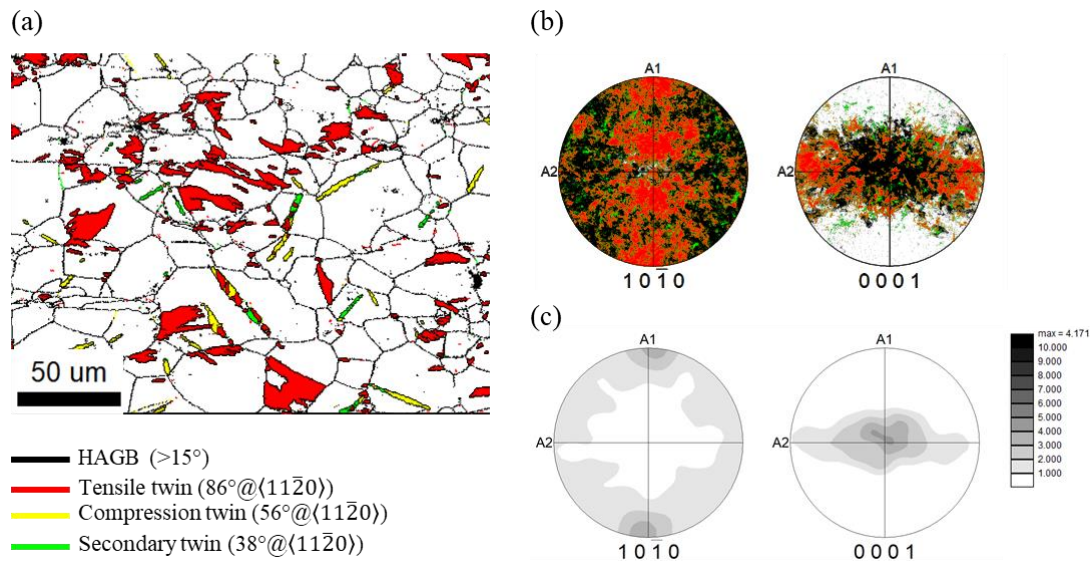


Fig. 5.2.10 (a) EBSD boundary map of (b) the corresponding orientations generated at the different twinned area as red, yellow, and green in the $(10\bar{1}0)$ and (0001) discrete pole figures (c) the $(10\bar{1}0)$ and (0001) pole figures calculated in whole EBSD data of the tensile sample deformed to $\varepsilon = 10\%$ at RT in the ZX10.

The texture component corresponding to the tensile twins (red) as well as compression (yellow) and secondary (green) twins is visible in the discrete pole figure in Fig. 5.2.10 (b). This texture component is consistent with the deformation texture measured by hard X-ray diffraction, i.e. TD split component perpendicular to the LD in (0002) pole figure as well as a strengthening of $\langle 10\bar{1}0 \rangle$ component at the LD. It is to note that these components are not clearly observed in the $(10\bar{1}0)$ and (0001) pole figures calculated from the whole EBSD data, Fig. 5.2.10 (c). Hence, it can be concluded that the twin activity in the present study is not the deformation mode determining global texture. Moreover, the development of diverse textures in each sheet, despite a similar fraction of twin activity, supports that high activity of non-basal $\langle a \rangle$ slip with a predominant prismatic $\langle a \rangle$ slip is the controlling mechanism of the texture development.

The impact of the c/a ratio is not significant on the texture development. The lattice parameters a and c and the corresponding c/a ratio were determined from the $(10\bar{1}0)$ and (0002) peaks of the initial samples measured from the synchrotron radiation. The results are listed in Table 5.2.2, and it is clear that all examined alloys have similar lattice parameters and c/a ratios.

Table 5.2.2. Lattice parameters a and c and c/a ratio measured using $(10\bar{1}0)$ and (0002) peaks of the results from the synchrotron diffraction measurement for the initial tensile samples in all examined sheets

Alloy	a	c	c/a
ZK10	0.3213	0.5215	1.6228
N05	0.3216	0.5218	1.6226
X05	0.3216	0.5218	1.6225
ZN10	0.3213	0.5215	1.6228
ZX10	0.3213	0.5216	1.6231

5.2.4 Discussion: effect of initial texture on dislocation activity

The results of the CMWP and IGMA analyses consistently show a high activation of non-basal $\langle a \rangle$ dislocations, especially relating to the prismatic $\langle a \rangle$ slip, in Figs. 5.2.7 and 5.2.9. In the CMWP analysis, the N05 and X05 indicate the enhanced activation of non-basal $\langle a \rangle$ dislocations compared to the ZK10. The activation of non-basal $\langle a \rangle$ and pyramidal $\langle c+a \rangle$ dislocations are significantly enhanced in the ZN10 and ZX10, especially in the RD samples. Interestingly, the apparent differences of the activation of non-basal $\langle a \rangle$ and pyramidal $\langle c+a \rangle$ dislocations are diminished in the TD samples of the ZN10 and ZX10. These results suggest that alloying additions and different initial textures should be considered as an influencing factor on the activity of slip systems.

Each alloy examined in the present study shows a distinct initial texture, as shown in Fig. 5.1.3. The ZK10 forms the basal pole in the ND (no pronounced basal pole spread towards the RD or TD), and the N05 and X05 show the basal pole split toward the RD, and the ZN10 and ZX10 indicate a considerable broadening of the basal pole toward the TD. It is generally known that the different textures provide different Schmid factor. For example, the texture of the ZN10 and ZX10 with a wide broadening of the basal pole towards the TD provides a high Schmid factor for the basal $\langle a \rangle$ slip during the loading in the TD. In contrast, a basal type texture or a slight broadening of the basal pole, observed in the ZK10, N05, and X05, provide a relatively lower Schmid factor for the basal $\langle a \rangle$ slip [44, 48]. Indeed, in the CMWP analysis shown in Fig. 5.2.7, the increasing ratio of basal $\langle a \rangle$ dislocation was found at the early deformation stage in the TD samples of the ZN10 and ZX10, and the N05 and X05 with the RD spread of the basal pole have a relatively high ratio of basal $\langle a \rangle$ dislocation during the RD loading. However, the activation of basal $\langle a \rangle$ dislocations at the early deformation stage, up to $\varepsilon = 5\%$, diminishes gradually with increasing the strain, despite the high Schmid factor for basal $\langle a \rangle$ slip. That is, the different initial texture influences on the activation of slip systems at the early deformation stage. With increasing strain, the activation of the slip system is relatively less influenced by the initial texture, which means that it is influenced by other factors, e.g. alloying elements.

5.2.5 Discussion: effect of alloying elements on dislocation activity

Significantly enhanced activities of non-basal $\langle a \rangle$ and $\langle c+a \rangle$ dislocations were found in the examined sheets, except for the ZK10, Figs. 5.2.6 and 5.2.7. It was observed that the prismatic $\langle a \rangle$ slip predominantly contributes to the high activation of non-basal $\langle a \rangle$ dislocations, Fig. 5.2.9. An important factor influencing the activation of different slip systems is the alloying elements. The addition of Zn or Al into Mg enhances the cross slip from the basal plane to the prismatic plane due to the solution effect [40]. In the case of Nd or Ca addition, it was reported that the formation of an intermetallic particle such as Mg_2Ca , $\text{Mg}_{41}\text{Nd}_5$, or Mg_{12}Nd in Mg enhances the activity of the prismatic $\langle a \rangle$ slip due to reducing the ratio $\text{CRSS}_{\text{prism.}}/\text{CRSS}_{\text{basal}}$ [18]. The formation of the corresponding

phases in the examined alloys is shown in the equilibrium phase diagrams, Fig. A.2 in the appendix. In addition to the formation of intermetallic phases, the addition of RE elements such as Y, Nd as well as Ca plays an important role as a solute in solid solution, changing the stacking fault energy (SFE) [51, 52, 76]. The addition of RE elements results in a significant decrease in the SFE on the basal plane and promotes a formation of the stacking faults and/or localized segregation during recrystallization [70]. Similar results for the Ca addition were reported in the previous study [71].

The decrease of the SFE on the basal plane can act as a sessile defect structure (stacking faults) to hinder the dislocation glide on the basal plane. Consequently, the dislocation glide on other planes is induced. It is associated with changes of the CRSS on the specific plane, i.e. hardening of the CRSS of basal slip simultaneously with softening of the CRSS of prismatic or pyramidal slip. Besides, the decrease of SFE promotes the stabilized configuration of extended dislocation, and its stabilization further promotes the partial dislocations [76, 106, 107]. Consequentially, the basal $\langle a \rangle$ slip is restricted, and other slip modes are promoted. Also, it has been suggested that the stacking fault acts as a source of formation of $\langle c+a \rangle$ dislocations [76, 107]. It was assumed that the distinct decrease of the SFE or the formation of stacking faults due to the addition of alloying elements promotes the formation of $\langle c+a \rangle$ dislocations by cross slip. Interestingly, the source mechanism described the formation of partial dislocation on a pyramidal plane by the interaction of the $\langle a \rangle$ dislocation glide on a prismatic plane with sessile c dislocation, which exists intrinsically in the matrix of the initial material. This mechanism can provide a basis for heterogeneous nucleation sources for the pyramidal $\langle c+a \rangle$ dislocations and can be correlated to the activation of the prismatic $\langle a \rangle$ slip. Therefore, it can be understood that the activation of non-basal $\langle a \rangle$ and $\langle c+a \rangle$ dislocations are highly enhanced by the addition of Nd or Ca due to decreasing the SFE and simultaneously promoting the stacking faults on the basal plane.

The activation of non-basal $\langle a \rangle$ and $\langle c+a \rangle$ dislocations becomes more pronounced with the simultaneous addition of Zn with Nd or Ca, such as ZN10 and ZX10, compared to the sole addition of Nd or Ca. In earlier works, it was reported that the simultaneous addition of Zn and Nd induces more easily the extended dislocation configuration to be stabilized and the dissociation of dislocation into partials than sole Zn or Nd [108]. Similar findings

were observed by [106], in which the SFE significantly decreases with the simultaneous addition of Zn and Y in Mg-Zn-Y rather than in Mg-Y. Hence, it is supposed that the simultaneous addition of Zn and Nd or Ca provides a higher probability of sources for activating non-basal $\langle a \rangle$ and $\langle c+a \rangle$ slip with the formation of the stacking fault. The Zn and Zr addition in Mg does not distinctly influence on a decrease of the SFE [52].

5.3 Dislocation activities at elevated temperature

5.3.1 Results: *in-situ* texture measurements under tensile loading

In the above Chapter, deformation mechanisms at RT were addressed in relation with the effects of alloying elements and initial textures. However, the forming processes of Mg and its alloys, which are difficult to deform at RT, are typically performed at elevated temperatures. The deformation temperature strongly influences on the activities of deformation mechanisms. In order to analyze the deformation mechanisms at elevated temperatures, the *in-situ* X-ray experiments were conducted during the tensile loading along the RD at elevated temperatures, 100 °C and 200 °C.

Mechanical properties

The stress-strain curves acquired from the continuous tensile tests at 100°C and 200°C are shown in Fig. 5.3.1. Similar to the experiment at RT, the stress-strain curves acquired from *in-situ* experiments at 100°C and 200°C showed the stress relaxation during the sample rotation and the collection of diffraction patterns. The stress-strain curves of the *in-situ* measurements well match to those obtained by continuous loading in all the examined samples. The mechanical properties are summarized in Table 5.3.1. Unlike the loading at RT, all samples show a distinct decrease in YS and UTS, in comparison to RT, and a high fracture elongation that is higher than $\epsilon = 30\%$ in most sheets. The ZK10, which showed a high YS (116 MPa) and UTS (190MPa) at RT compared to other sheets, shows a relatively clear decrease of YS and UTS with increasing deformation temperature, especially pronounced at 200°C. In contrast, the YS and UTS of the other alloys decrease

moderately with increasing deformation temperature. Comparing the strength values between RT and 200°C, the ZK10 shows a decrease of about 6-fold in YS and 3-fold in UTS (18 MPa and 61 MPa, respectively, at 200°C). But the other sheets show a relatively smaller decrease, e.g. about a half in YS (39 ~ 64 MPa) and 60% in UTS (106 ~ 130 MPa at 200°C) compared to the values at RT, as listed in Table 5.3.1. Such differences between the alloys correlate with the thermal softening mechanisms, such as dynamic recrystallization (DRX) or dynamic recovery (DRV), and it seems to be promoted in the ZK10, i.e. retardation of the thermally activated mechanisms in the other alloys. In addition, the decreased YS relates to the reduced CRSS for dislocation slip at higher deformation temperature, especially for non-basal slip. It is clear that the occurrence of the thermal softening mechanisms and the changes in YS with the reduced CRSS at elevated temperatures are influenced by the addition of alloying elements. That is, the deformation mechanisms and their activities are different at elevated temperatures from those at RT.

It is to be noted that serrated flow curves are evidently presented in the examined sheets at 200°C, in Fig. 5.3.1. The serration in flow curves is typically known as plastic instability. Similar results were reported in [109-113], in which the serrated flows in RE or Ca containing Mg alloys occur in a specific regime of deformation, e.g. at a certain range of temperature (150 ~ 250°C) and strain rate (approximately $1 \times 10^{-4}/s \sim 10^{-3}/s$). This is correlated with a solid solution strengthening mechanism in terms of solute-dislocation interactions, e.g. a pronounced dynamic strain aging (DSA).

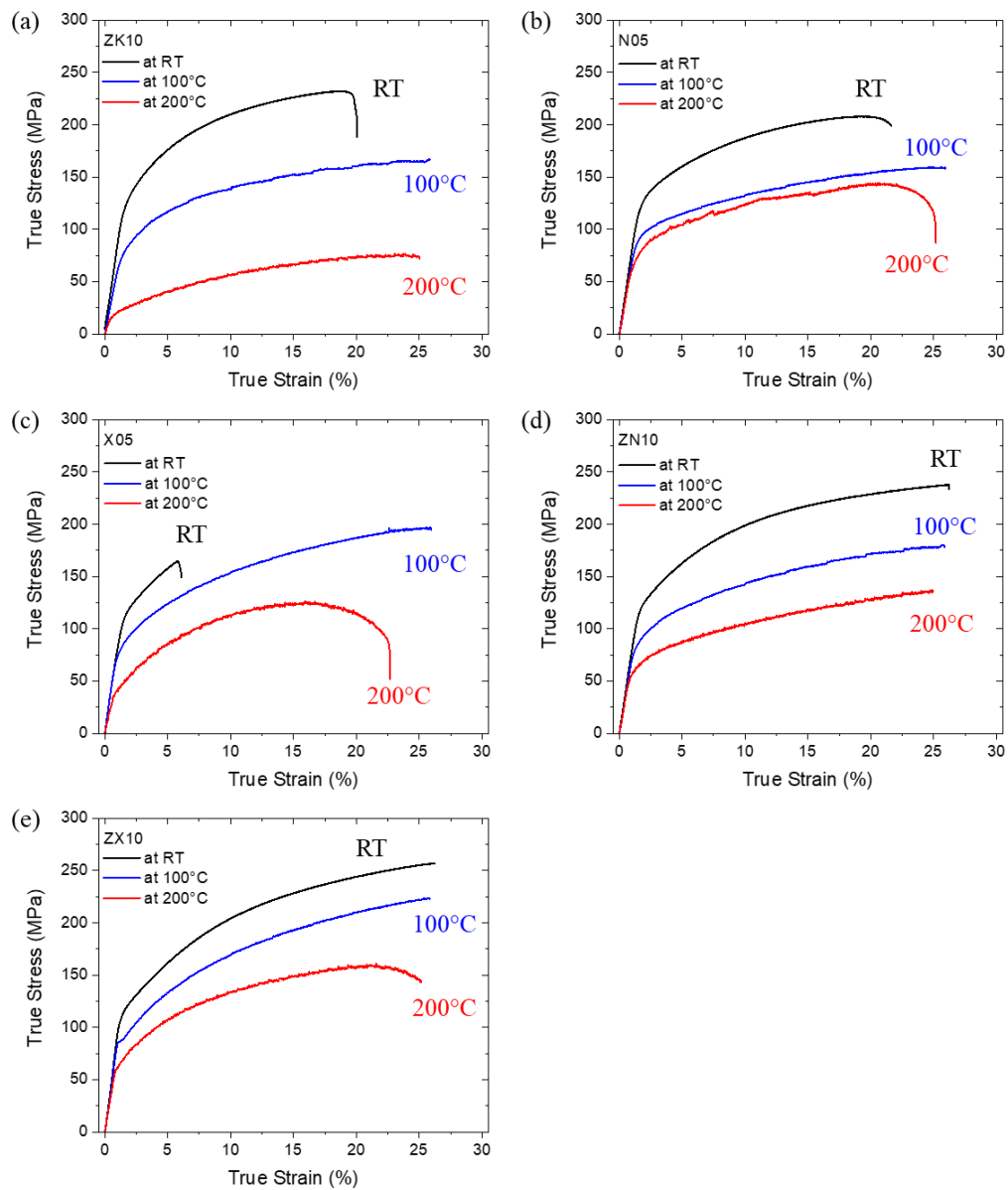


Fig. 5.3.1 True stress-strain curves during the tensile tests along the RD and TD at different temperatures, RT (black), 100°C (blue), and 200°C (red) of all examined sheets: (a) ZK10, (b) N05, (c) X05, (d) ZN10, and (e) ZX10.

Table 5.3.1 Tensile properties along RD measured for the examined sheets at 100°C and 200°C (YS: yield strength (MPa), UTS: ultimate tensile strength (MPa), and FS: fracture strain (%)).

Alloy	at 100°C			at 200°C		
	YS	UTS	FS	YS	UTS	FS
ZK10	75	133	-	18	61	-
N05	86	126	-	64	113	26
X05	74	156	-	39	109	26
ZN10	80	141	-	55	106	-
ZX10	85	173	-	62	130	-

Texture developments

The $\{10\bar{1}0\}$ and (0002) pole figures from the *in-situ* texture measurements at the tensile strains of $\varepsilon = 5\%$ and 15% along the RD at 100°C and 200°C are shown in Figs. 5.3.2 and 5.3.3, respectively. It is to note that the textures could be measured at $\varepsilon = 5\%$ and $\sim 27\%$ (after fracture) for the N05 deformed at 200°C, Fig. 5.3.3 (b), due to a technical problem in the beamline, i.e. unexpected shut-down of the beam.

The tensile loading at 100°C and 200°C results in a similar tendency of texture developments to that at RT for all the examined sheets, which are a strengthening of the $\langle 10\bar{1}0 \rangle$ pole at the LD and the spread of the (0002) pole perpendicular to the LD. The basal pole broadening perpendicular to the LD is observed in all the examined sheets, except for the ZK10, with increasing strain, and the characteristic 6-fold poles are evidently exhibited in the $\{10\bar{1}0\}$ pole figure. This tendency of texture development is more obvious in the ZN10 and ZX10, in comparison to the texture formed at the comparable strain at RT shown in Fig. 5.2.3. As discussed in Chapter 5.2, the difference in the texture development between the examined alloys is correlated with the importance of activation of the slip modes. Consequently, it is anticipated that the identical

deformation modes with different importance in their activities are responsible for the texture developments also at elevated temperatures.

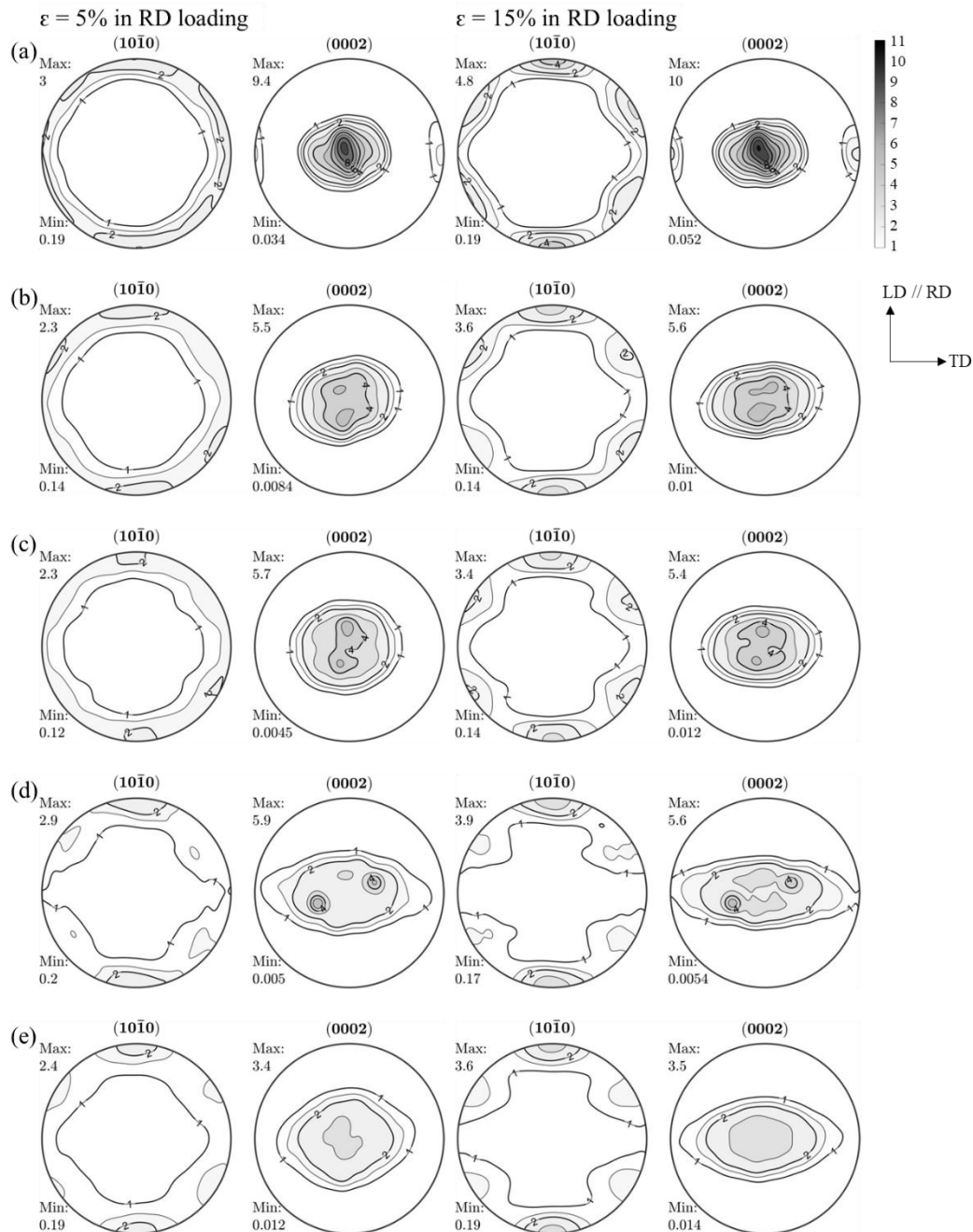


Fig. 5.3.2 $\{10\bar{1}0\}$ and (0002) pole figures of tensile sample deformed to at $\epsilon = 5\%$ and 15% along the RD at 100°C for the examined sheets: (a) ZK10, (b) N05, (c) X05, (d) ZN10, and (e) ZX10. Contour levels = 1.0, 1.5, 2.0, 3.0, 4.0, ..., 11.0 m.r.d.

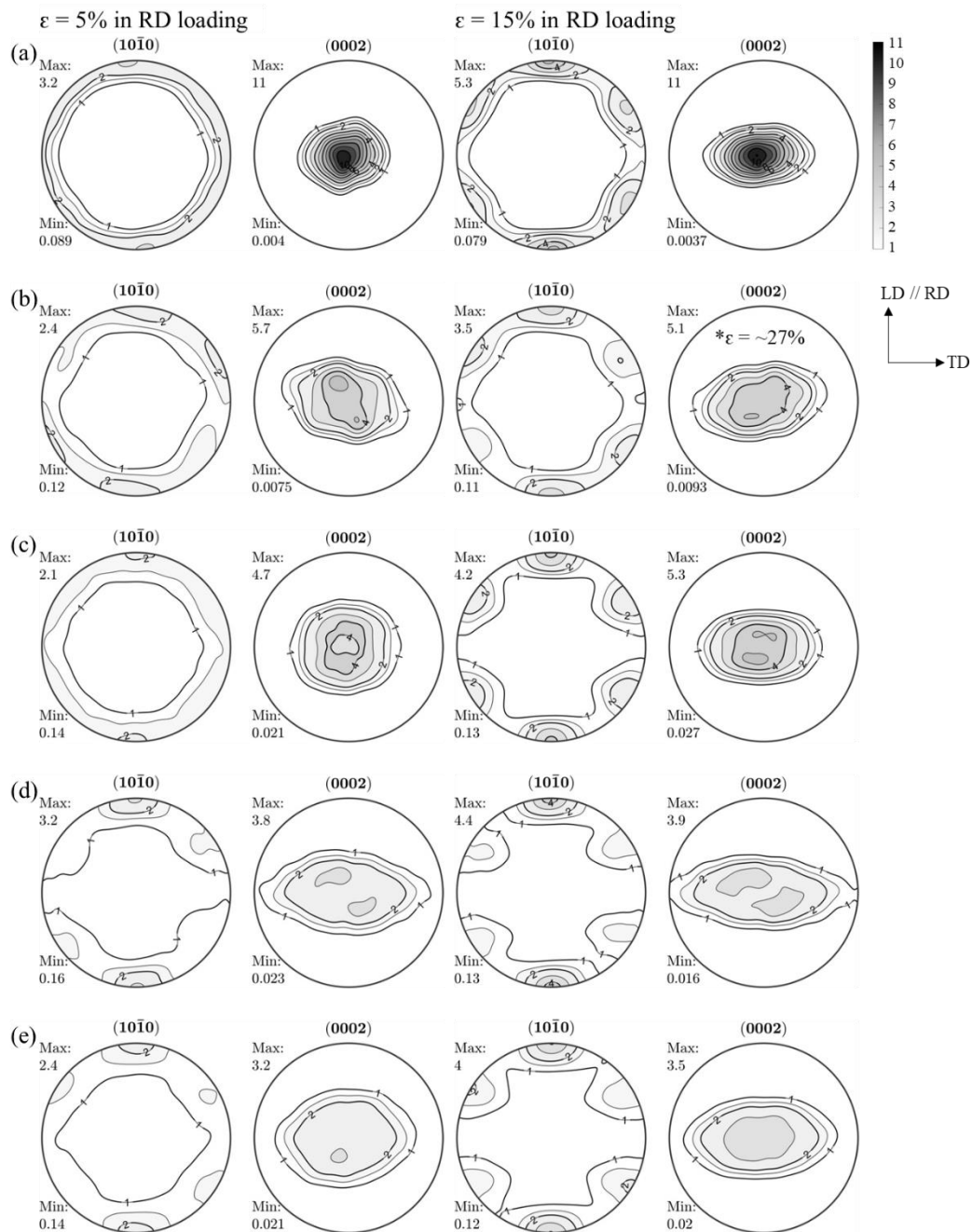


Fig. 5.3.3 {10 $\bar{1}$ 0} and (0002) pole figures of tensile sample deformed to at $\epsilon = 5\%$ and 15% along the RD at 200°C for the examined sheets: (a) ZK10, (b) N05, (c) X05, (d) ZN10, and (e) ZX10. Contour levels = 1.0, 1.5, 2.0, 3.0, 4.0, ..., 11.0 m.r.d.

5.3.2 Results: dislocation activities at elevated temperatures

In this section, the dislocation activities varied with deformation temperature are described separately for each sheet. The results obtained from the CMWP analysis at the elevated temperatures are summarized in Table A.3 - A.7 in the appendix.

ZK10

The variation of overall dislocation densities, their classifications according to the Burgers vectors, and the ratio of basal $\langle a \rangle$ and non-basal $\langle a \rangle$ dislocations to the overall density are given in Fig. 5.3.4.

A remarkable change of overall dislocation density is clearly shown with increasing temperature. The overall dislocation density at 100°C is comparable to that at RT, but that at 200°C significantly decreases. The preferred dislocations types that are classified by Burgers vectors do not change with increasing temperature, as shown in Fig. 5.3.4 (b). The $\langle a \rangle$ dislocation has the highest density, that is followed by the $\langle c+a \rangle$ dislocation, and the $\langle c \rangle$ dislocation plays a minor role.

The difference in overall dislocation density at different temperatures is caused by the different activities of $\langle a \rangle$ and $\langle c+a \rangle$ dislocations. At 100°C, the $\langle a \rangle$ and $\langle c+a \rangle$ dislocation densities slightly increase compared with that at RT during deformation, while their densities decrease at 200°C. The density of the $\langle a \rangle$ dislocation is lowest at 200°C among the examined temperatures, and the density of $\langle c+a \rangle$ dislocation decreases. No distinct increase of the dislocation density at 200°C, despite the low CRSS for non-basal dislocations, can be understood as a result of thermally activated processes, such as DRX and DRV, as well as accompanying dislocation annihilation.

The $\langle a \rangle$ dislocations, which are dominant at all temperatures, is composed of the high amount of non-basal $\langle a \rangle$ dislocations with their ratio of 0.33 ~ 0.67 and the basal $\langle a \rangle$ dislocation with its ratio lower than 0.20, Fig. 5.3.4 (c). Interestingly, the ratio of non-basal $\langle a \rangle$ dislocations significantly increases at 100°C compared to RT, 0.37 to 0.44 at RT and 0.40 to 0.67 at 100°C. It can be explained by that the activation of non-basal $\langle a \rangle$

dislocations, as well as the $\langle c+a \rangle$ dislocations, which are slightly increased, are thermally enhanced at 100°C, due to the decrease of the CRSS on the non-basal slip. At 200°C, despite the decrease in the overall dislocation density, the ratio of non-basal $\langle a \rangle$ dislocation is higher than that at RT, while the ratio of basal $\langle a \rangle$ dislocations is similar to that at RT. This can also be understood by thermally enhanced activities of non-basal slip at elevated temperatures.

Fig. 5.3.5 displays the EBSD orientation maps from the tensile samples deformed to $\varepsilon = 10\%$. The deformed grains with intragranular misorientation are observed at all temperatures. At RT, the microstructure corresponding to the localized deformation marked with a white dash line is observed, but it is not observed at 100°C and 200°C.

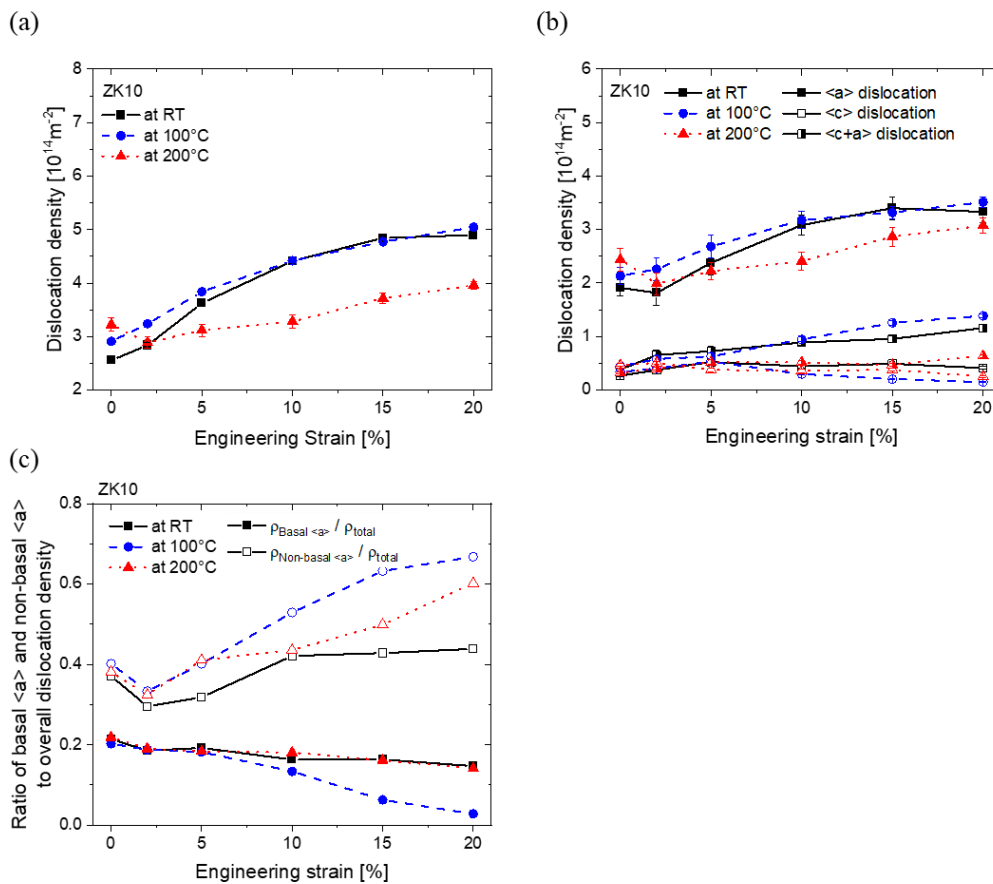


Fig. 5.3.4 Dislocation evolutions as function of applied strains along the RD at different temperatures, RT, 100°C, and 200°C in the ZK10. (a) overall dislocation densities, (b) dislocation densities classified according to $\langle a \rangle$, $\langle c \rangle$, and $\langle c+a \rangle$ dislocations, (c) the ratio of basal (solid) and non-basal $\langle a \rangle$ (open) dislocations to the overall dislocation

Moreover, it is remarkable that the sample deformed at 200°C shows serrated grain boundaries and some fine grains formed at grain boundaries, marked with black arrows in Fig. 5.3.5 (c). The corresponding IGMA distribution is evaluated for the group of grains having similar orientations (RED- and BLUE-grains, same to those applied for the RT), shown in Fig. 5.3.6. Similar to the results at RT, the samples deformed at 100°C and 200°C show high concentrations of IGMA around the $\langle 0001 \rangle$ axis in the RED-grains, which corresponds to the predominant activity of prismatic $\langle a \rangle$ slip. It can be seen that most of the density in the non-basal $\langle a \rangle$ dislocations is attributed to the predominant activity of prismatic $\langle a \rangle$ slip at all examined temperatures. In the BLUE-grains, the ZK10 shows uncertain concentrations with low grain statistics at elevated temperatures, which is caused by a strong basal type texture.

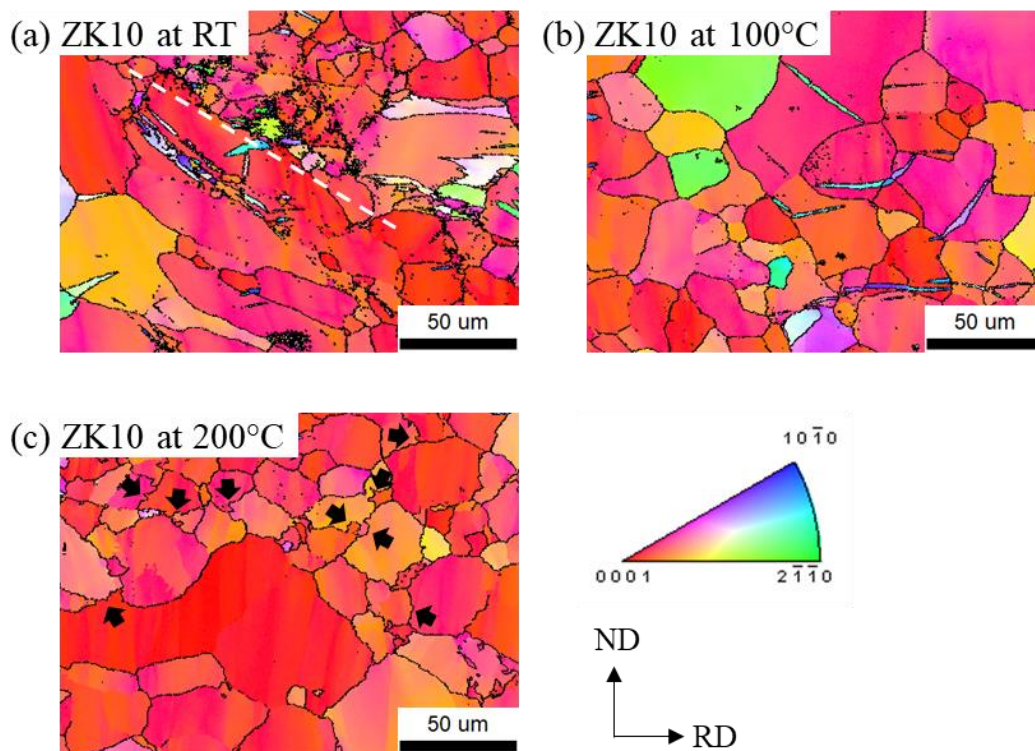


Fig. 5.3.5 EBSD orientation maps for the ZK10 deformed to $\epsilon = 10\%$ at 3 different temperatures; (a) RT, (b) 100°C, and (c) 200°C. High angle grain boundaries ($\theta > 15^\circ$) are marked with a black line. Black arrows in Fig. 5.14 (c) indicate the boundary serration.

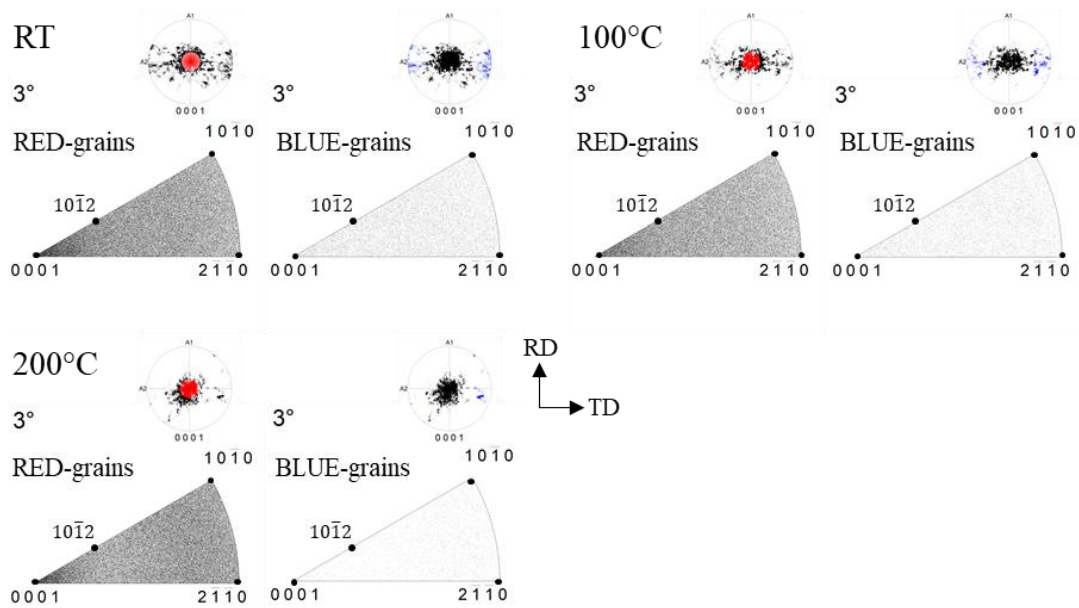


Fig. 5.3.6 IGMA distributions evaluated in deformed grains classified by $GOS > 2^\circ$ depending on the grain orientations (RED- or BLUE-grains) of the ZK10 deformed to $\epsilon = 10\%$ at 3 different temperatures. The (0001) discrete pole figures indicating the orientation of the grains selected for the IGMA analysis are inserted.

N05 and X05

Fig 5.3.7 presents the variation of overall dislocation densities, their classifications according to the Burgers vectors, and the ratio of basal $\langle a \rangle$ and non-basal $\langle a \rangle$ dislocations to overall dislocations for the N05 and X05.

Differently to the ZK10, the N05 shows a comparable overall dislocation density at the 3 different temperatures. Also, each dislocation type, classified by Burgers vectors, has similar densities at different temperatures, while the $\langle c+a \rangle$ dislocation shows a slightly higher density at 100 °C, up to $\epsilon = 15\%$, Fig. 5.3.7 (b). However, the ratio of non-basal $\langle a \rangle$ dislocations varies at different temperatures, Fig. 5.3.7 (c). An apparent increase in the ratio of non-basal $\langle a \rangle$ dislocations is observed at 100°C. Concurrently, the ratio of basal $\langle a \rangle$ dislocation slightly decrease. It is clear that the contribution of non-basal $\langle a \rangle$

and $\langle c+a \rangle$ dislocations to the overall dislocation density increases at 100°C, while the contribution of basal $\langle a \rangle$ dislocations decreases. This seems to be related to the change of relative CRSS values on the slip systems. The X05 shows a similar tendency to that found in the N05, which is a high ratio of non-basal $\langle a \rangle$ dislocations and a slight increase of the $\langle c+a \rangle$ dislocation at 100°C, as shown in Fig. 5.3.7 (e) and (f). However, at 200°C, the $\langle a \rangle$ and $\langle c+a \rangle$ dislocations are relatively reduced compared to that at 100°C, relating to thermally active processes, e.g. DRX or DRV.

Fig. 5.3.8 displays the EBSD orientation maps from the tensile samples deformed to $\varepsilon = 10\%$ for the N05 and X05, and the corresponding IGMA distributions are shown in Fig. 5.3.9. The deformed grains that are identified by the intragranular misorientations are observed at all deformation temperatures. Differing from the ZK10, the serrated grain boundaries are not observed in the N05 and X05 deformed at 200°C. For IGMA analysis in the corresponding samples, the concentration around $\langle 0001 \rangle$ axis markedly increases at 100°C and 200°C. This finding relates to the enhanced activation of the prismatic $\langle a \rangle$ slip based on the reduced CRSS with increasing temperature. Indeed, the enhanced activation of non-basal $\langle a \rangle$ and $\langle c+a \rangle$ dislocations was observed in the CMWP results, Fig. 5.3.7. In both IGMA and CMWP analyses, the high ratio of non-basal $\langle a \rangle$ dislocations matches well.

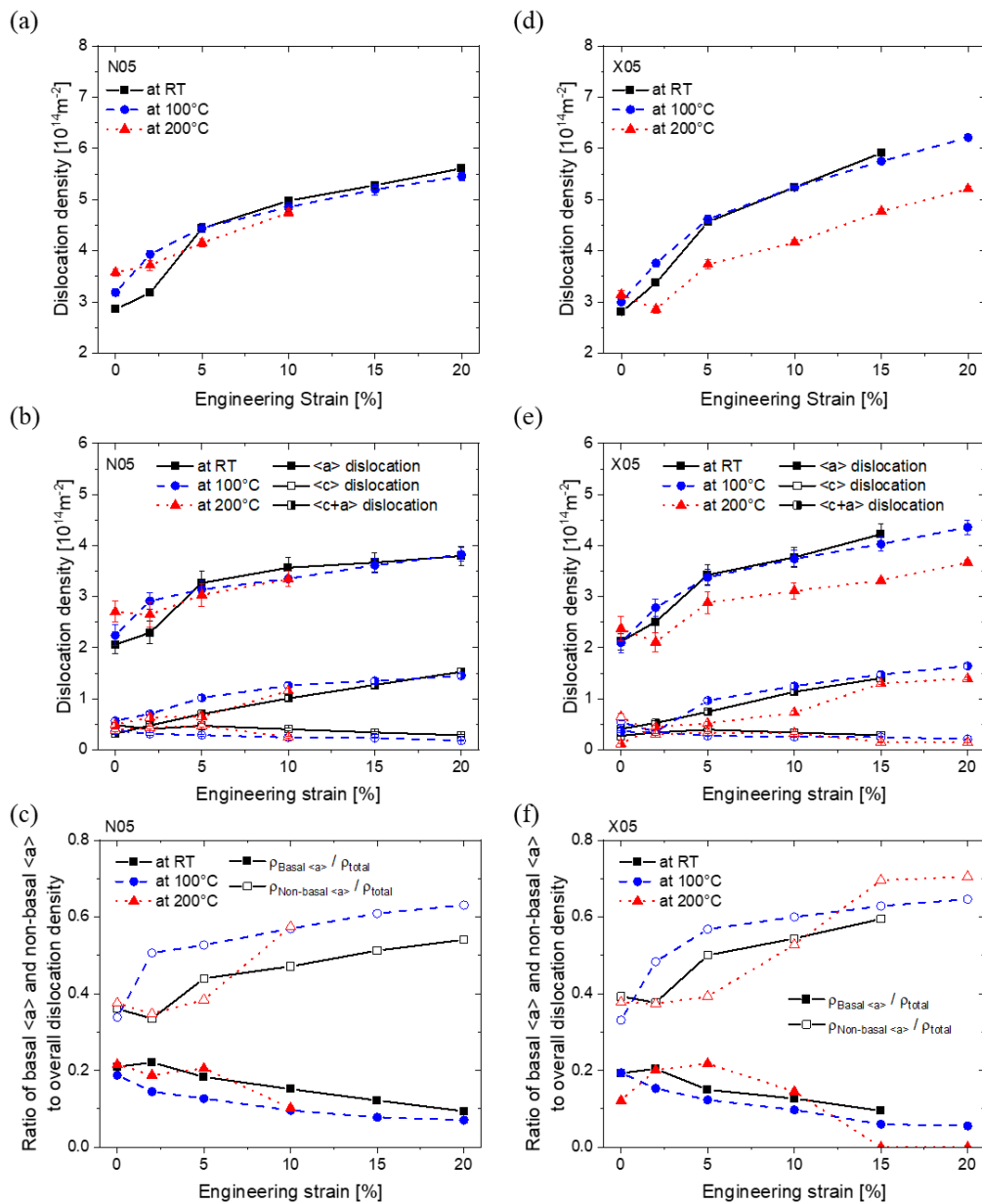


Fig. 5.3.7 Dislocation evolutions as function of applied strains along the RD at different temperatures, RT, 100°C, and 200°C in the N05 and X05. (a) and (b) overall dislocation densities, (b) and (e) dislocation densities classified by $\langle a \rangle$, $\langle c \rangle$, and $\langle c+a \rangle$ dislocations; (c) and (f) ratio of the basal and non-basal $\langle a \rangle$ dislocations to the overall dislocation.

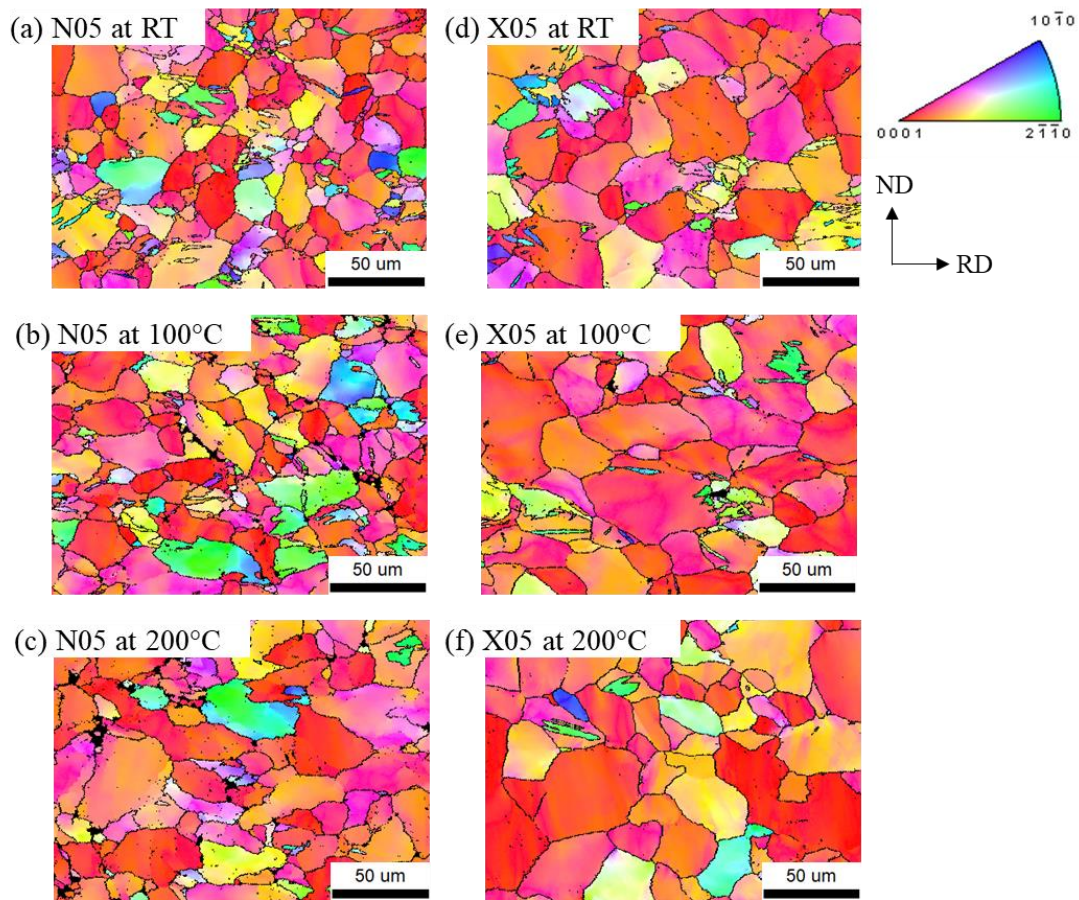


Fig. 5.3.8 EBSD orientation maps for the N05 and X05 deformed to $\epsilon = 10\%$ at 3 different temperatures. (a) ~ (c) for the N05 and (d) ~ (f) for the X05. The sample of N05 at 200°C was observed at $\epsilon = \sim 8\%$, Fig. 5.3.8 (c). High angle grain boundaries ($\theta > 15^\circ$), are marked with a black line.

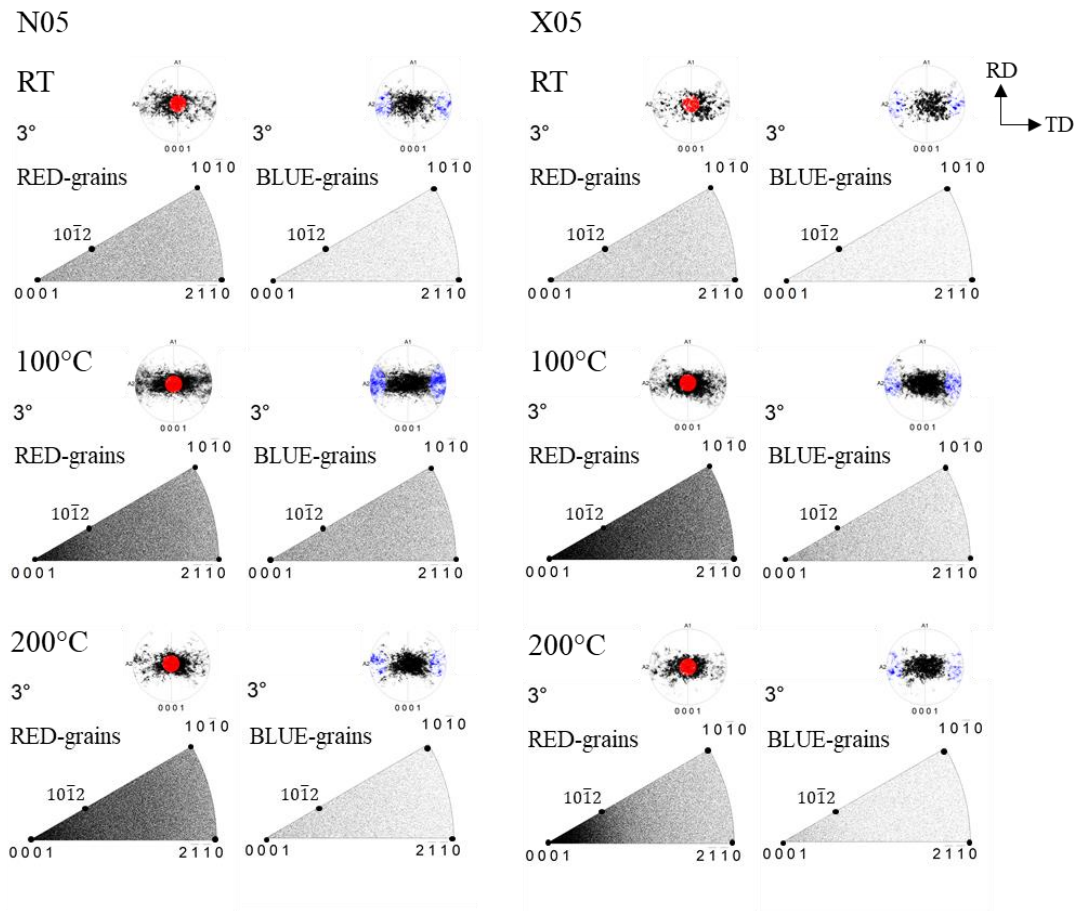


Fig. 5.3.9 IGMA distributions evaluated in deformed grains classified by $GOS > 2^\circ$ depending on the grain orientations (RED- or BLUE-grains) of the N05 and X05 deformed to $\epsilon = 10\%$ at 3 different temperatures. The sample of the N05 at 200°C was evaluated at $\epsilon = \sim 8\%$, Fig. 5.3.9 (c). The (0001) discrete pole figures indicating the orientation of the grains selected for the IGMA analysis are inserted.

ZN10 and ZX10

The variation of overall dislocation densities, their classifications according to the Burgers vectors, and the ratio of basal $\langle a \rangle$ and non-basal $\langle a \rangle$ dislocations to overall dislocations are given in Fig. 5.3.10.

The ZN10 shows a decrease in the overall dislocation density at 100°C, while it is retained at 200°C, Fig. 5.3.10 (a). The ZX10 shows a stepwise decrease in the overall dislocation density as the temperature increases, Fig. 5.3.10 (d).

Moreover, it is remarkable that the ZN10 and ZX10 show no significant decreases in the densities of $\langle c+a \rangle$ dislocations despite the decrease in overall dislocation densities. In other words, the decrease in the overall dislocation density with increasing temperature relating to the thermally active processes (DRX or DRV) is attributed to a relatively higher decrease of $\langle a \rangle$ dislocations rather than $\langle c+a \rangle$ dislocations, which differs from the other sheets.

The ratio of non-basal $\langle a \rangle$ dislocations in the ZN10 and ZX10 shows a slight change at different temperatures compared with that at RT, unlike other sheets. While the ratio of non-basal $\langle a \rangle$ dislocations slightly decreases at 100°C in both alloys, no significant difference is found at 200°C to the ratio at RT, even a slightly higher ratio of non-basal $\langle a \rangle$ dislocations than at RT in the ZN10, Fig. 5.3.10 (c) and (f).

EBSD orientation maps acquired from the tensile samples deformed to $\varepsilon = 10\%$ at different temperatures are presented in Fig. 5.3.11. Similar to the N05 and X05, the deformed grains are observed in the ZN10 and ZX10. The serrated grain boundaries, which are found in the ZK10, are not found at 100°C and 200°C. The IGMA distribution of the ZN10 and ZX10 is shown in Fig. 5.3.12. The ZN10 and ZX10 show a high concentration around the $\langle 0001 \rangle$ axis at all testing temperatures, regardless of the grain orientations (RED- and BLUE-grains). These results indicate that the non-basal $\langle a \rangle$ dislocations do not significantly decrease in the ZN10 and ZX10 even at elevated temperatures.

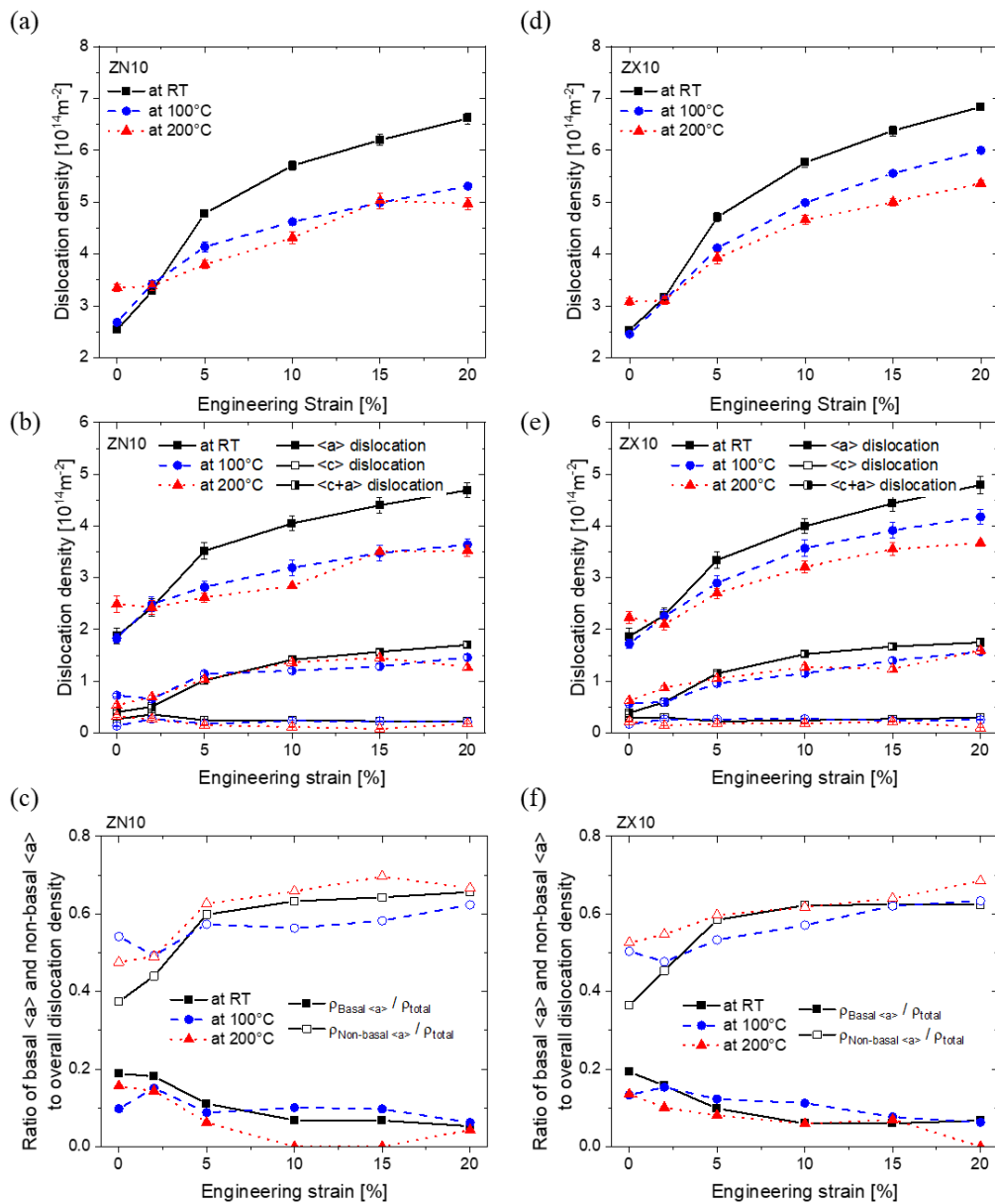


Fig. 5.3.10 Dislocation evolutions as function of applied strains along the RD at different temperatures, RT, 100°C, and 200°C in the ZN10 and ZX10. (a) and (b) overall dislocation densities, (b) and (e) dislocation densities classified by <a>, <c>, and <c+a> dislocations, (c) and (f) the ratio of basal <a> and non-basal <a> dislocations to overall dislocation

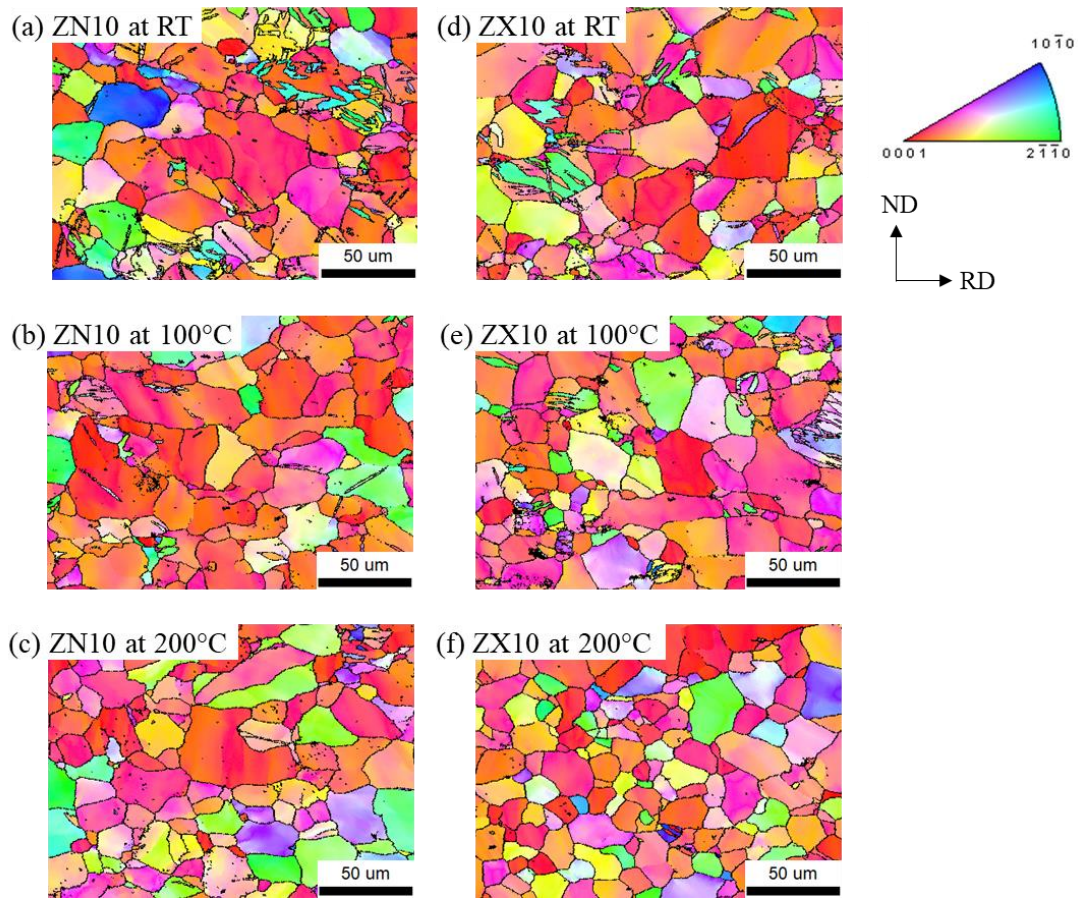


Fig. 5.3.11 EBSD orientation maps for the ZN10 and ZX10 deformed to $\varepsilon = 10\%$ at 3 different temperatures. (a) ~ (c) for the ZN10 and (d) ~ (f) for the ZX10. High angle grain boundaries ($\theta > 15^\circ$), are marked with a black line.

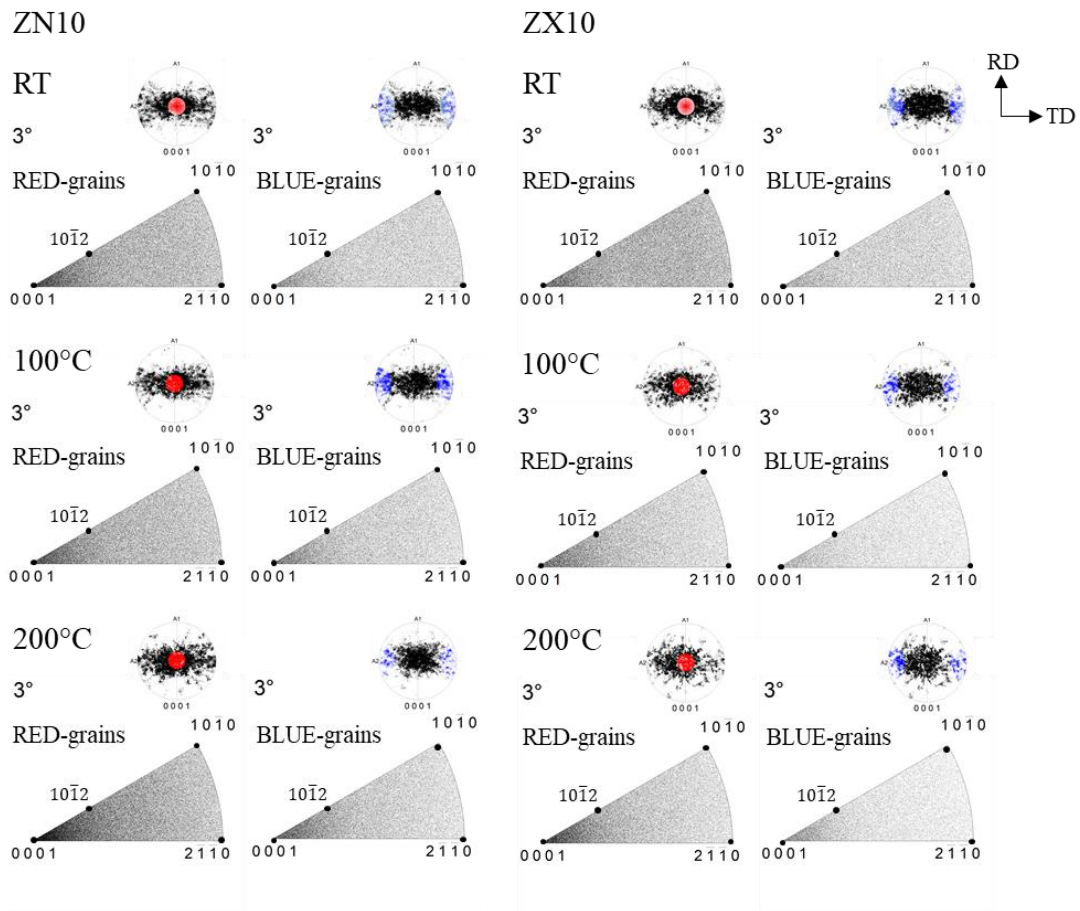


Fig. 5.3.12 IGMA distributions evaluated in deformed grains classified by $GOS > 2^\circ$ depending on the grain orientations (RED- or BLUE-grains) of the ZN10 and ZX10 deformed to $\varepsilon = 10\%$ at 3 different temperatures. The (0001) discrete pole figures indicating the orientation of the grains selected for the IGMA analysis are inserted.

5.3.3 Discussion: effect of deformation temperature on dislocation activity

The preference of diverse dislocations classified by Burgers vectors is basically retained at all examined temperatures. The $\langle a \rangle$ and $\langle c+a \rangle$ dislocations have a main contribution to the overall dislocation densities, whereas the $\langle c \rangle$ dislocations have a minor role in the strain accommodation.

During the deformation at elevated temperatures, a noticeable difference is observed in the dislocation densities between the examined alloys. That is, the amount of dislocations

activated or annihilated (or recovered) by the temperature increase are different. Since the recovery and recrystallization processes occur by eliminating dislocations, i.e. reducing the stored energy (dislocation densities), a decrease in dislocation density is generally observed during the deformation at elevated temperature [114]. However, comparable densities of overall dislocation were shown in the ZK10, N05, and X05 deformed at RT and 100°C. The ratio of non-basal $\langle a \rangle$ and $\langle c+a \rangle$ dislocations slightly increase at 100°C, compared to those at RT, while the ratio of basal $\langle a \rangle$ dislocations decreases, in Figs. 5.3.4 and 5.3.7. These results are associated with a reduced CRSS for non-basal $\langle a \rangle$ and $\langle c+a \rangle$ slip at 100°C. Similar results of the reduced CRSS for non-basal slip with increasing temperature were reported in earlier works [40, 42, 115, 116]. A reduction in the activation energy required for cross slip from basal to non-basal planes can attribute to the reduced CRSS. All examined alloys show a high ratio of non-basal $\langle a \rangle$ dislocation, larger than 0.60, at 100°C. It can be understood that basal $\langle a \rangle$ slip cannot easily activate in the ZK10 due to strong basal texture with a lower Schmid factor [22, 48], while non-basal $\langle a \rangle$ slip with a reduced CRSS is more favorably activated with increasing temperature. The increased activities of non-basal $\langle a \rangle$ dislocations at 100°C compensate for the dislocation annihilation induced by thermally activated processes. In contrast, the ZK10 deformed at 200°C shows a distinct decrease of the overall dislocation density, which is the lowest in all testing conditions, $\rho_{total} = 3.96 \times 10^{14} \text{ m}^{-2}$ at $\varepsilon = 20\%$. The ratio of non-basal $\langle a \rangle$ and $\langle c+a \rangle$ dislocations also reduced at 200°C. Concerning that the ratio of basal $\langle a \rangle$ dislocations is similar to that at RT, the reduction of the overall dislocation density is attributed to the decreased activities of non-basal $\langle a \rangle$ and $\langle c+a \rangle$ dislocations. Compared to the ZK10, the other sheets show high overall dislocation densities, higher than $4.5 \times 10^{14} \text{ m}^{-2}$. The reduction of the overall dislocation densities accompanying the temperature increase does not directly connect to certain dislocations, differently to the ZK10. The densities of $\langle c+a \rangle$ dislocations are maintained even at elevated deformation temperatures. That is, the alloy elements cause different retardation of the thermally activated processes, relating to DRX or DRV, during deformation at elevated temperatures, especially pronounced in the case of simultaneous addition of Zn and Nd or Ca, i.e. the ZN10 and ZX10.

The retarded reduction of dislocation densities measured from the CMWP analysis can be visibly determined by the kernel average misorientation (KAM) in the EBSD

measurement. The KAM maps and the number fractions measured from the tensile samples deformed to $\varepsilon = 10\%$ are shown in Figs. 5.3.13 and 5.3.14, respectively. The ZK10 deformed at RT shows a concentration of the KAM higher than 3° within the deformation bands, Fig. 5.3.13 (a), whereas a decrease of the KAM higher than 3° with vanishing the deformation band is observed at 100°C and 200°C , Figs. 5.3.13 (b) and (c). The uniform deformation at elevated temperature, without the occurrence of deformation band, is associated with the enhanced slip activities. Indeed, a higher number fraction of the KAM higher than 1° is observed at 100°C , Fig. 5.3.14 (b), than that at RT. A clear increase in the number fraction of the KAM lower than 1° is shown at 200°C , Fig 5.3.14 (c). The increase of the low KAM is related to the thermally activated process such as DRX or DRV. The ZK10 deformed at 200°C shows the fine grains around the grain boundary and the serrated grain boundaries, in Fig. 5.3.5 (c). This is consistent to the results of the CMWP analysis. Moreover, it was reported in earlier work [73] that the non-basal dislocations provide an early formation of a DRX grain structure in ZK60. This matches to the present results showing the onset of DRX, such as the serrated grain boundaries, in the ZK10 deformed at 200°C . By the onset of the DRX, the densities of non-basal $\langle a \rangle$ and $\langle c+a \rangle$ dislocations are decreased, while the retarded reduction of dislocation densities observed in the others sheets deformed at 200°C . Instead of DRX, the other sheets deformed at elevated temperatures show a uniform deformation that is indicated by a high number fraction of the KAM higher than 1° , Figs. 5.3.14 (b) and (c). This is associated with the high slip activities in the experimental conditions, which is consistent with the results of the CMWP analysis. The retarded reduction can be correlated to an interaction of dislocation with solute atoms, e.g. solute trapping of dislocations and restricted dislocation mobility [19, 31-33].

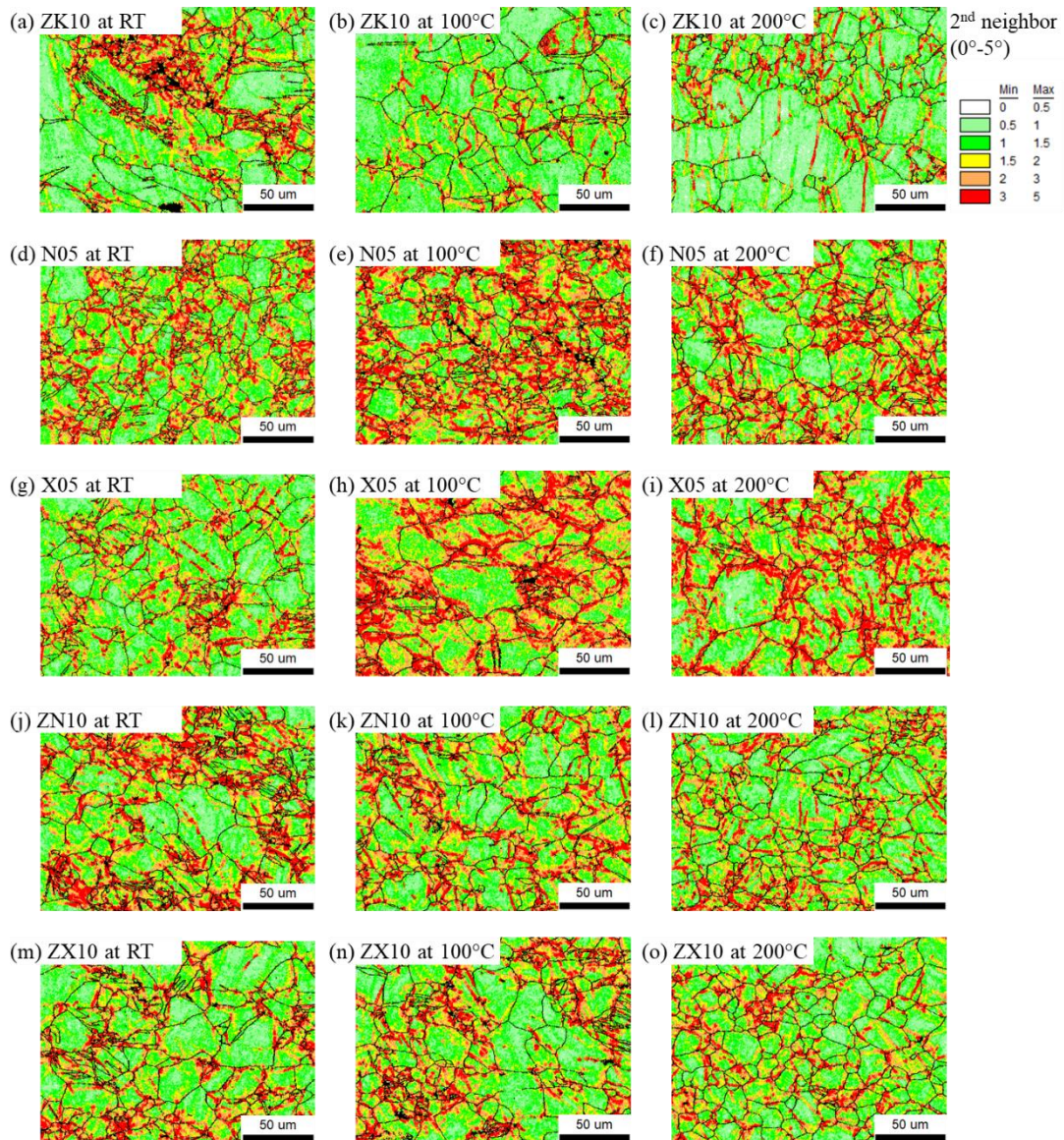


Fig. 5.3.13 Kernel average misorientation (KAM) maps with color codes in tensile samples deformed to $\epsilon = 10\%$ at different temperatures for the examined alloys; (a) ~ (c): ZK10, (d) ~ (f): N05, (g) ~ (i): X05, (j) ~ (l): ZN10, and (m) ~ (o): ZX10. High angle grain boundaries, $\theta > 15^\circ$, are marked with a black line.

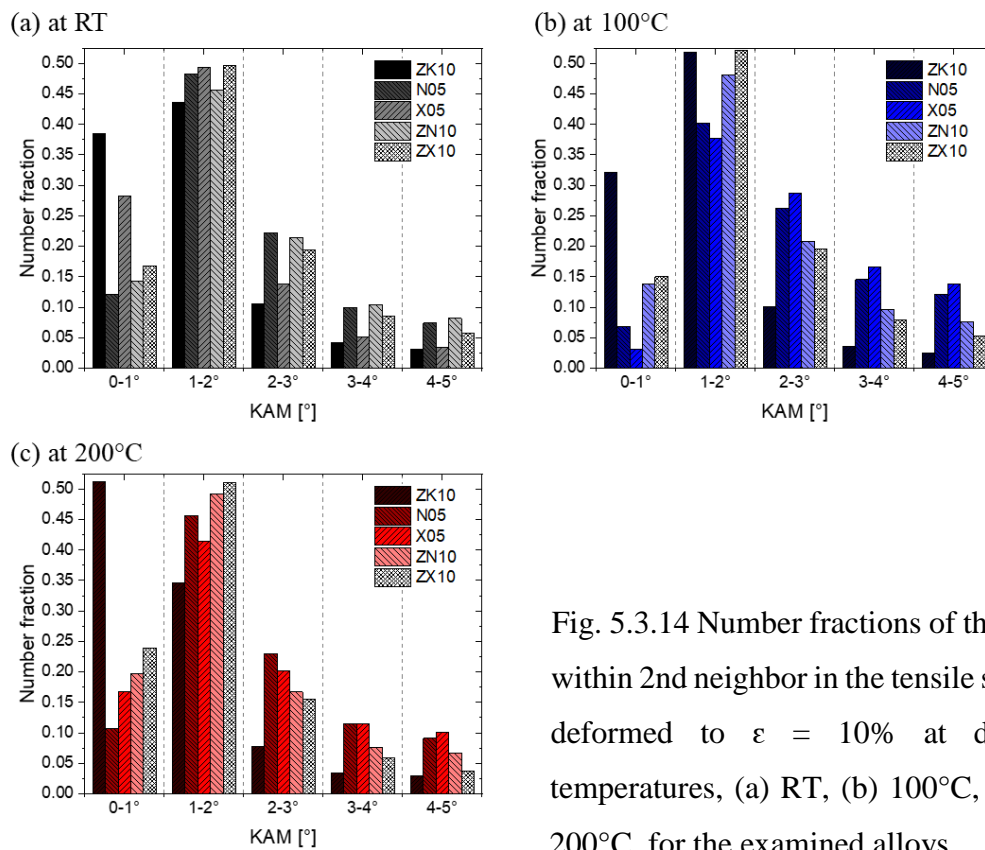


Fig. 5.3.14 Number fractions of the KAM within 2nd neighbor in the tensile samples deformed to $\epsilon = 10\%$ at different temperatures, (a) RT, (b) 100°C, and (c) 200°C, for the examined alloys.

It is to be noted that the decrease in the overall dislocation density in the ZN10 and ZX10 deformed at 100°C, compared to those at RT, is observed, whereas the maintained densities of the $\langle c+a \rangle$ dislocations are found even the deformation temperature increases. It can be associated with the dislocation reaction that the dislocations are annihilated or rearranged. It was reported in [54, 117] that the activity of $\langle c+a \rangle$ dislocations plays an influential role in the dislocation reaction, the corresponding reaction can be described as:



It supports that the high density of the $\langle c+a \rangle$ dislocations observed in the ZN10 and ZX10 provides a relatively high probability of the corresponding dislocation reaction, relating to a decrease in the overall dislocation density at 100°C.

Several studies reported that the basal pole spread toward the TD is attributed to the retarded recrystallization kinetics with low boundary energy, i.e. reduced boundary mobility by co-segregation of Zn and RE or Ca atoms at grain boundaries, during the heat treatment of Mg-Zn-RE or Mg-Zn-Ca alloy sheets [70, 108, 118]. It was revealed in the present study that the higher activity of prismatic $\langle a \rangle$ slip is correlated with the broadening of the basal poles perpendicular to the LD under tensile loading in the examined alloys. In order to investigate the relationship between the dislocations measured in the present study and the texture evolution during the annealing, the heat treatment at 350°C for 30 min was conducted using the tensile samples deformed to $\epsilon = \sim 32\%$ of the N05 and ZN10, that were used for the *in-situ* experiments at RT.

Fig. 5.3.15 displays the $\{10\bar{1}0\}$ and (0002) pole figures after deformation and annealing of the N05 and ZN10. The deformation textures of both alloys are similar to those presented in Fig. 5.2.3. During the annealing, the broadened basal poles toward the TD are diminished in the N05, whereas those in the ZN10 are still visible Fig. 5.3.15 (b). Fig. 5.3.16 presents the dislocation densities of the deformed and annealed samples from the CMWP analysis. A clear relaxation in the overall dislocation density after the annealing is found in the N05 with a decrease of $\sim 27\%$, while the ZN10 shows a decrease of $\sim 15\%$. The reduction of the overall dislocation densities is accompanied with the different reducing tendencies of each dislocation type. The relaxation in the N05 during the annealing occurs with the decrease of 17% and 6% in the ratio of non-basal $\langle a \rangle$ and $\langle c+a \rangle$ dislocations, and the 8% increase in the ratio of basal $\langle a \rangle$ dislocation, whereas the ZN10 shows no significant differences in the ratio of each dislocation. That is, the retarded reduction of the non-basal $\langle a \rangle$ and $\langle c+a \rangle$ dislocations is more evident in the ZN10 rather than in the N05. The above results clearly show that a higher activation of prismatic $\langle a \rangle$ slip and, simultaneously, strong retardation of the thermally activated process provides a high potential of the texture formation that is a wide broadening of the basal pole perpendicular to the main loading direction.

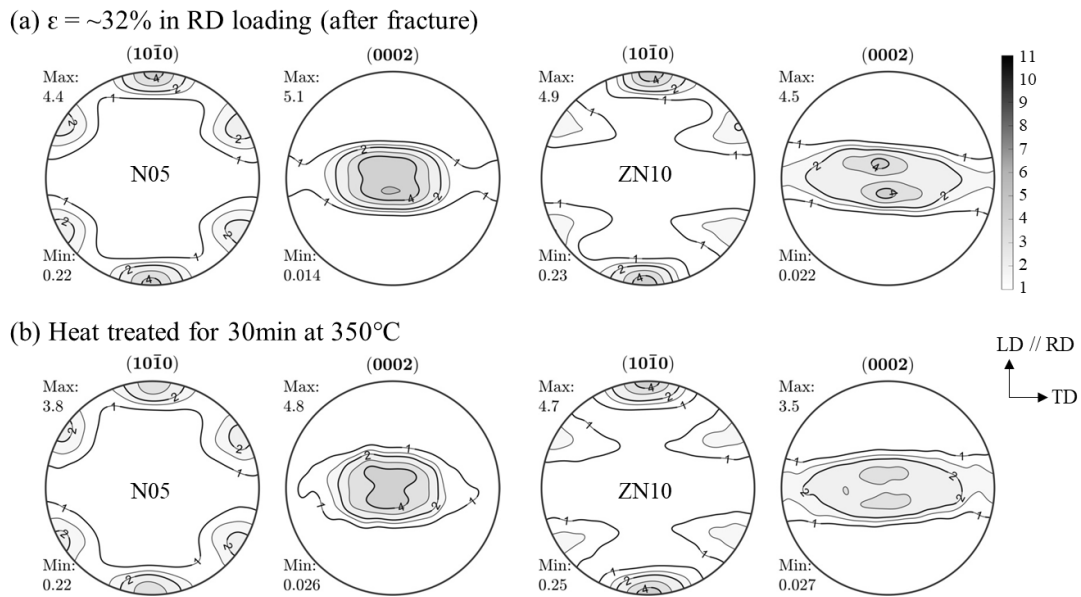


Fig. 5.3.15 $\{10\bar{1}0\}$ and (0002) pole figures of the tensile samples (a) deformed to $\epsilon = \sim 32\%$ and (b) annealed at 350°C for 30min of the N05 and ZN10. Contour levels = 1.0, 1.5, 2.0, 3.0, 4.0, ..., 11.0 m.r.d.

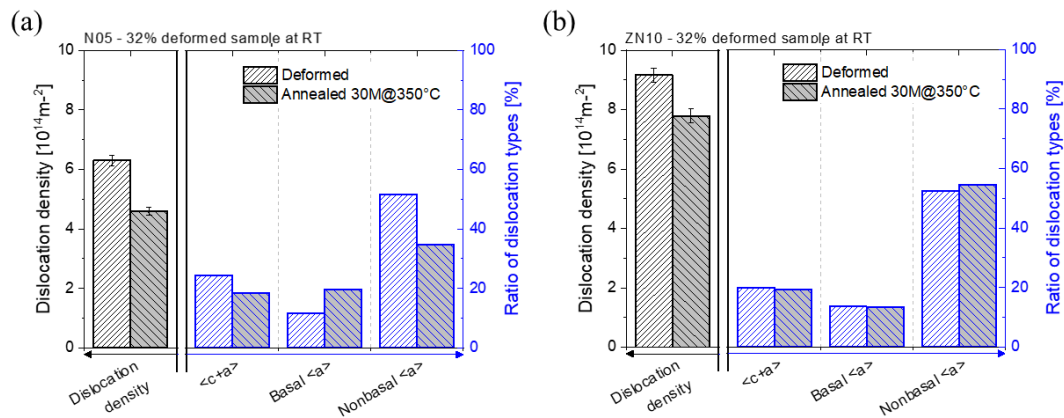


Fig. 5.3.16 Overall dislocation density and the ratio of dislocation types in the overall dislocation density evaluated from the CMWP analysis of the tensile samples deformed to $\epsilon = \sim 32\%$ and annealed at 350°C for 30 min of the (a) N05 and (b) ZN10.

Texture evolution under rolling of the ZN10 sheet

The hot-rolled ZN10 sheet was rolled at ambient temperature in order to investigate texture evolution and dislocation activities during the rolling. The cold rolling was carried out in one single pass with a thickness reduction of 5% to the final thickness of 4 mm. The *in-situ* texture measurement during annealing was conducted by using hard X-ray diffraction at synchrotron and the $\{10\bar{1}0\}$ and (0002) pole figures are displayed in Fig. 5.3.17. The basal pole split towards the RD is observed in the as-rolled ZN10 sheet. A broadening of the basal pole towards TD and a strengthening of $\langle 10\bar{1}0 \rangle$ pole in the RD are evolved during the annealing. The dislocation densities evaluated from the CMWP analysis are shown in Fig. 5.3.18. The dislocation density and its ratio of the rolled sheet are similar to those after the tensile deformation. The highest density of the $\langle a \rangle$ dislocations, followed by $\langle c+a \rangle$ dislocations, is found. The densities of $\langle c+a \rangle$ dislocations of the rolled sheet are similar to those of the deformed tensile sample, despite the basal pole split toward the RD is observed in the rolled sheet. It can be understood that such texture component developed in the rolled sheet is mainly contributed by twins, e.g. secondary twin activity. The high activation of the secondary twin is observed in the image quality (IQ) map from EBSD measurement, in Fig. 5.3.19 (b), and it contributes to the basal pole split toward the RD, which is in good agreement with the earlier works [6, 76]. It is to be noted that the dislocation densities are mostly reduced during the annealing at 200°C for 30 min, Fig. 5.3.18 (a), but the deformed microstructure with a high fraction of the KAM higher than 1° is still observed, Figs. 5.3.20 (a) and 5.3.21.

Fig. 5.3.17 (c) clearly shows that the basal poles broadening towards the TD with the weakening intensity after annealing at 325°C for 30 min, and the corresponding microstructure is fully annealed in Fig. 5.3.20 (b). However, the dislocations densities reduce rapidly after annealing at 325°C for 3 min, Fig. 5.3.18 (b), and the densities are not significantly changed with further increasing annealing time. This can be interpreted that texture evolution is closely related to the favorable growth of grain, having the grain orientation spread towards the TD, without reducing the dislocation densities. The basal pole spread toward the RD observed in the rolled sheet diminishes during the annealing, i.e. the growth of grains having the corresponding orientations is restricted. The high activation of the prismatic $\langle a \rangle$ slip promotes the formation of recrystallization nuclei

having the broadening of the basal poles toward the TD. It is worth to mention that the predominant activity of the dislocations under the rolling is similar to that under the tensile loading.

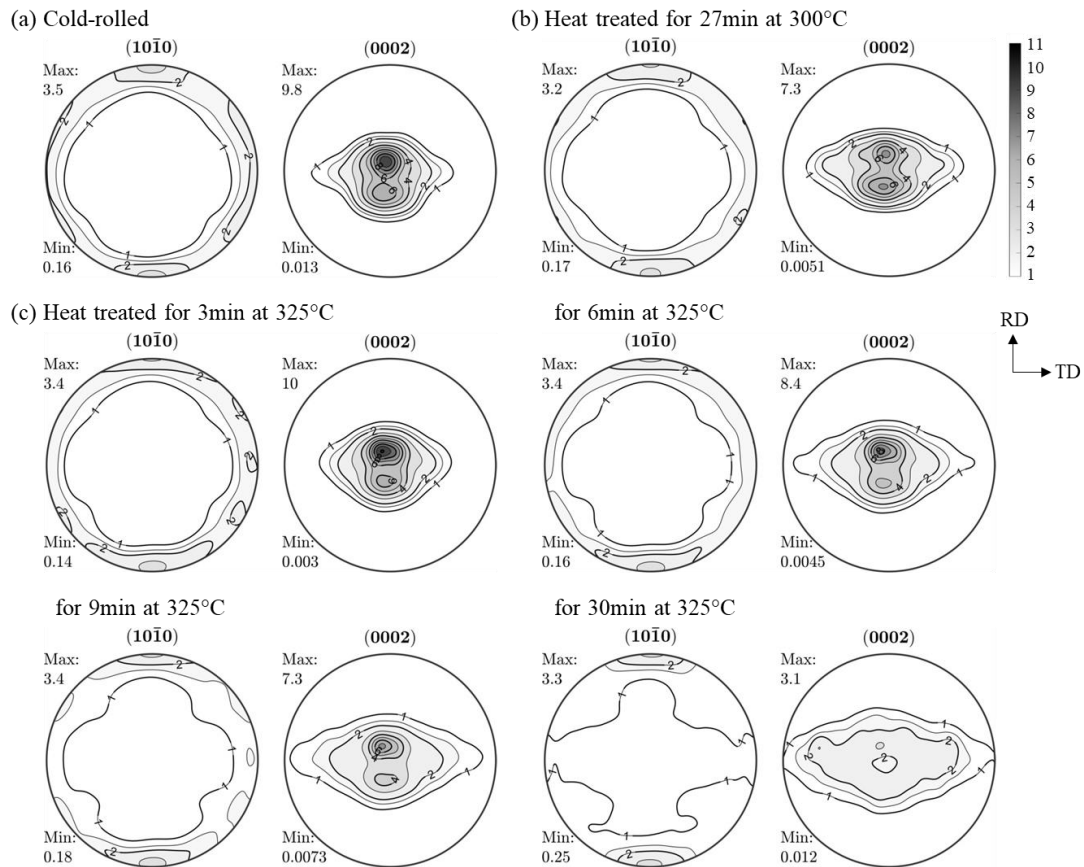


Fig. 5.3.17 $\{10\bar{1}0\}$ and (0002) pole figures measured for (a) cold-rolled and annealed conditions (b) at 200°C for 30 min and (c) at 325°C for 3 ~ 30 min of the cold-rolled ZN10 sheets. Contour levels = 1.0, 1.5, 2.0, 3.0, 4.0, ..., 11.0 m.r.d.

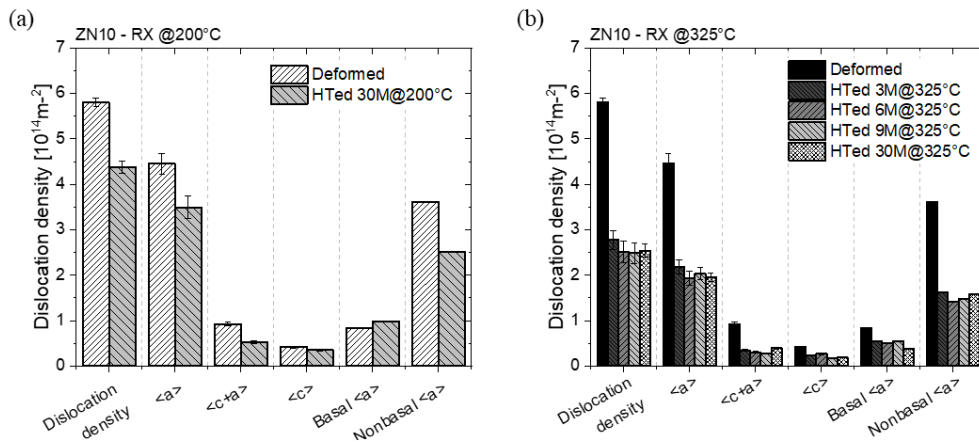


Fig. 5.3.18 Dislocation densities evaluated from the CMWP analysis after the annealing at (a) 200°C for 30 min and (b) 325°C for 30 min of the cold-rolled ZN10 sheet.

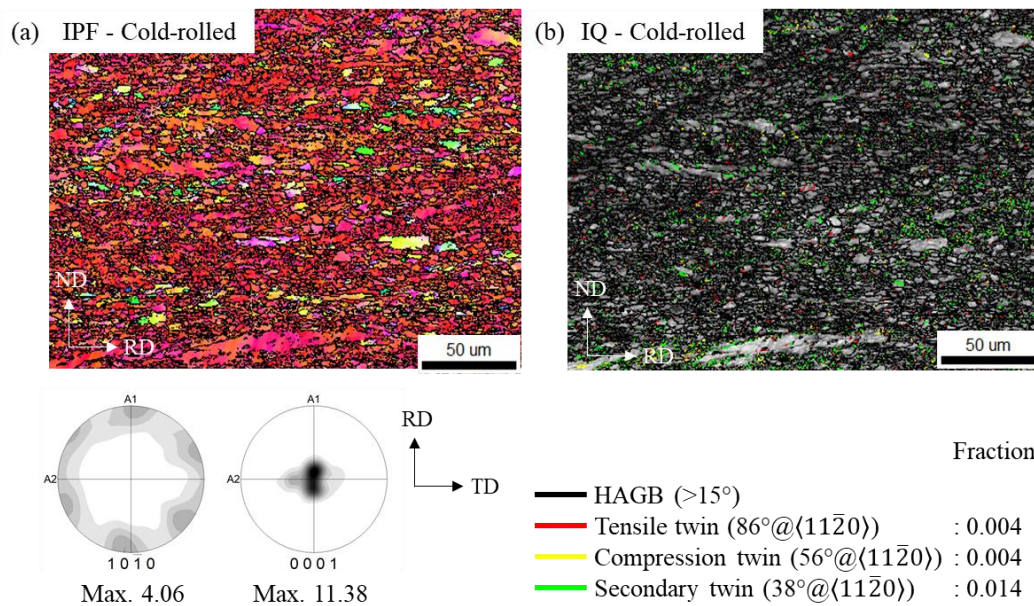


Fig. 5.3.19 EBSD observation of the cold-rolled ZN10 sheet. (a) EBSD orientation map, texture, and (b) twin boundaries with different color in image quality (IQ) map. High angle grain boundaries ($\theta > 15^\circ$) are marked with a black line. The colors of twin boundaries are shown in the insets.

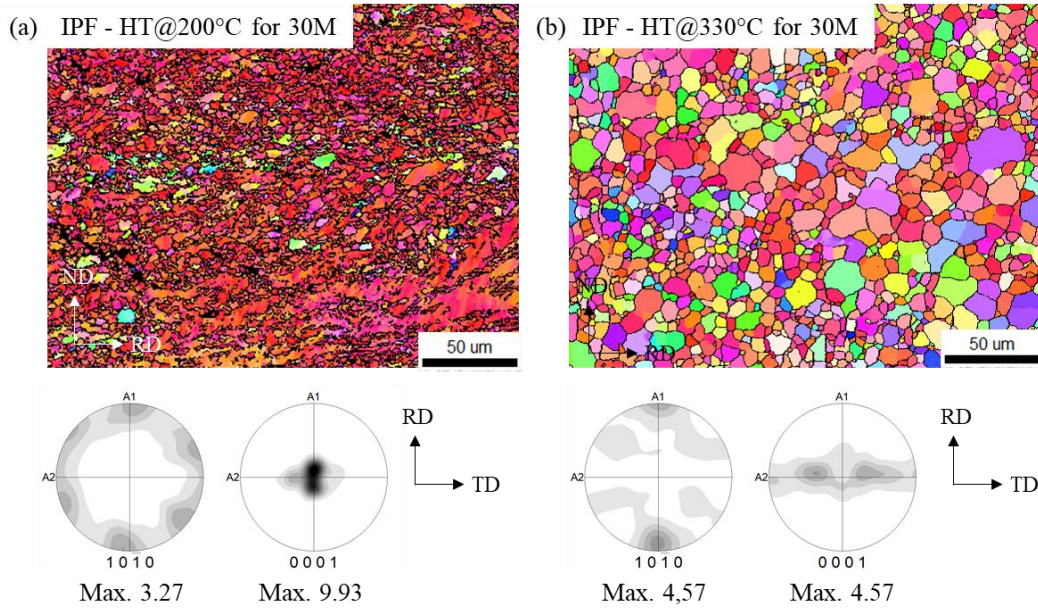


Fig. 5.3.20 IPF orientation map and texture for the cold-rolled ZN10 sheet after annealing at (a) at 200°C for 30 min and (b) 330°C for 30 min. High angle grain boundaries ($\theta > 15^\circ$) are marked with a black line.

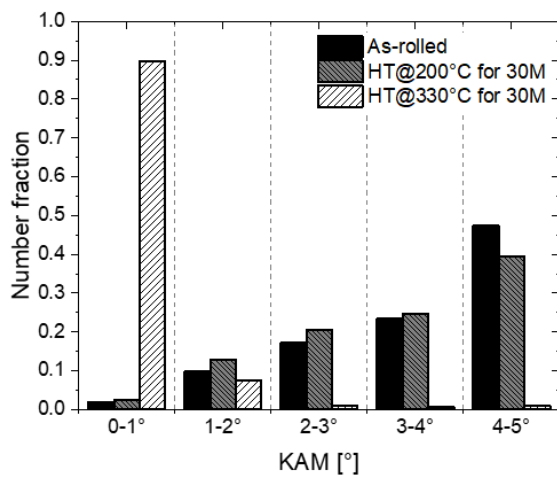


Fig. 5.3.21 Number fractions of the KAM within 2nd neighbor after the annealing at 200°C for 30 min and 330°C for 30 min of the cold-rolled ZN10 sheet

6 Summary and outlook

6.1 General remarks

Five Mg alloy sheets, Mg - 1.32 Zn - 0.13 Zr, Mg - 0.61 Nd, Mg - 0.52 Ca, Mg - 1.03 Zn - 0.73 Nd, and Mg - 0.91 Zn - 0.54 Ca in wt.%, were designed based on their different tendencies in texture development during thermomechanical treatments. The Mg sheets were investigated in terms of the interrelationship between the texture evolutions, the dislocation activities, and microstructure development under tensile loading at different temperatures. The *in-situ* experiments with synchrotron radiation were conducted. The obtained results were evaluated by the CMWP and IGMA analyses. Following results from the experimental investigations can be drawn:

- The results obtained from *in-situ* experiments by using hard X-ray diffraction at synchrotron under different testing conditions were successfully evaluated by the CMWP combined with IGMA analysis for tracking dislocation activities relating to the texture development.
- In all the experimental cases, a strengthening of the $\langle 10\bar{1}0 \rangle$ pole at the LD and a broadening of the $\langle 0001 \rangle$ pole perpendicular to the LD are observed, which is independent on the alloy elements and deformation conditions. The ZN10 and ZX10 containing Zn and simultaneously Nd or Ca present a pronounced evolution of the above mentioned texture during tensile loading, in comparison to the N05 and X05 with a sole addition Nd or Ca. The ZK10 without Nd and Ca addition presents a less pronounced texture development.
- The initial textures influence the texture evolution and dislocation activities at the early deformation stage. At a higher deformation degree, the alloy elements play a more important role on the dislocation activities and texture evolution.
- The high activation of the prismatic $\langle a \rangle$ slip is ascribed to the addition of Nd or Ca, compared to the addition of Zn. The simultaneous addition of Zn with Nd or Ca ensures the enhanced activation of non-basal $\langle a \rangle$ and $\langle c+a \rangle$ dislocations, in comparison with the sole addition of Zn, Nd, and Ca.

- A localized deformation, e.g. the deformation band, is observed in the ZK10 at RT, while a uniform deformation is observed in the other alloys. The deformation band does not occur with increasing deformation temperature due to the enhanced activation of non-basal $\langle a \rangle$ dislocations. The serrated grain boundaries and fine grains at the grain boundaries, i.e. the onset of DRX, are observed in the ZK10 deformed at 200°C. This results in a significant decrease in the overall dislocation density. Instead of DRX, the uniform deformation and the retardation of the thermally activated processes, e.g. DRV and DRX, are ascribed to the addition of Nd or Ca. The retardation becomes more pronounced with the simultaneous addition of Zn with Nd or Ca

6.2 Outlook

There are numerous directions along which the study presented in this dissertation may be extended for further useful investigation. The following points are recommended:

- The dislocation activities of Mg-Zn based alloy systems have been determined based on different alloy compositions and testing conditions under a limited deformation process in the present work. However, many kinds of researches were reported on the different role of dislocations in diverse Mg alloys, e.g. Mg-Al based or Mg-Mn based alloy. An extensive analysis of the dislocation activities applied in the present study of different Mg alloys under various deformation processes would be helpful to understand the relationship between dislocation activity and texture development.
- The investigation of the role of active dislocations related to grain nucleation or grain growth during the thermally activated process could not be analyzed due to premature relaxation in a short time in the present study. Regarding the above issue, an investigation or simulation model would be helpful to interpret the role of the dislocations in the formation of recrystallization nuclei relating to the texture weakening.
- It is proved that the *in-situ* X-ray line profile technique as an advanced *in-situ* experimental method is useful to investigate the dislocation structure. This

technique has the potential for broad applicability in studies of deformation and recrystallization mechanisms in diverse metallic materials.

References

- [1] C.J. Bettles, M.A. Gibson, Current Wrought Magnesium Alloys: Strengths and Weaknesses, *Jom-U*s 57 (2005) 46-49.
- [2] H. Friedrich, S. Schumann, Research for a "new age of magnesium" in the automotive industry, *Journal of Materials Processing Technology* 117(3) (2001) 276-281.
- [3] J. Hirsch, T. Al-Samman, Superior light metals by texture engineering: Optimized aluminum and magnesium alloys for automotive applications, *Acta Materialia* 61(3) (2013) 818-843.
- [4] B.-C. Suh, M.-S. Shim, K.S. Shin, N.J. Kim, Current issues in magnesium sheet alloys: Where do we go from here?, *Scripta Materialia* 84-85 (2014) 1-6.
- [5] N.T. Nguyen, O.S. Seo, C.A. Lee, M.G. Lee, J.H. Kim, H.Y. Kim, Mechanical Behavior of AZ31B Mg Alloy Sheets under Monotonic and Cyclic Loadings at Room and Moderately Elevated Temperatures, *Materials (Basel)* 7(2) (2014) 1271-1295.
- [6] S.R. Agnew, M.H. Yoo, C.N. Tome, Application of texture simulation to understanding mechanical behavior of Mg and solid solution alloys containing Li or Y, *Acta Materialia* 49(20) (2001) 4277-4289.
- [7] J. Bohlen, G. Kurz, S. Yi, D. Letzig, Rolling of magnesium alloys, (2012) 346-375.
- [8] L. Stutz, J. Bohlen, G. Kurz, D. Letzig, K.U. Kainer, Influence of the processing of magnesium alloys AZ31 and ZE10 on the sheet formability at elevated temperature, *Key Eng Mater* 473 (2011) 335-342.
- [9] U. F. Kocks, C. N. Tomé, H.-R. Wenk, *Texture and anisotropy*, Cambridge University Press, 1998.
- [10] T. Al-Samman, X. Li, Sheet texture modification in magnesium-based alloys by selective rare earth alloying, *Mat Sci Eng a-Struct* 528(10-11) (2011) 3809-3822.
- [11] K. Hantzsche, J. Bohlen, J. Wendt, K.U. Kainer, S.B. Yi, D. Letzig, Effect of rare earth additions on microstructure and texture development of magnesium alloy sheets, *Scripta Materialia* 63(7) (2010) 725-730.
- [12] M.-T. Pérez-Prado, J. Bohlen, S. Yi, D. Letzig, T. Al-Samman, J. Robson, M. Barnett, W. Poole, C. Mendis, S. Agnew, N. Stanford, *Emerging Hot Topics and Research Questions in Wrought Magnesium Alloy Development*, *Jom-U*s (2020).
- [13] N. Stanford, M.R. Barnett, The origin of "rare earth" texture development in extruded Mg-based alloys and its effect on tensile ductility, *Mat Sci Eng a-Struct* 496(1-2) (2008) 399-408.
- [14] L.W.F. Mackenzie, M. Pekguleryuz, The influences of alloying additions and processing parameters on the rolling microstructures and textures of magnesium alloys, *Materials Science and Engineering: A* 480(1-2) (2008) 189-197.
- [15] K.-H. Kim, B.-C. Suh, J.H. Bae, M.-S. Shim, S. Kim, N.J. Kim, Microstructure and texture evolution of Mg alloys during twin-roll casting and subsequent hot rolling, *Scripta Materialia* 63(7) (2010) 716-720.
- [16] J. Bohlen, J. Wendt, M. Nienaber, K.U. Kainer, L. Stutz, D. Letzig, Calcium and zirconium as texture modifiers during rolling and annealing of magnesium-zinc alloys, *Materials Characterization* 101 (2015) 144-152.
- [17] Y. Chino, T. Ueda, Y. Otomatsu, K. Sassa, X. Huang, K. Suzuki, M. Mabuchi, Effects of Ca on Tensile Properties and Stretch Formability at Room Temperature in Mg-Zn and Mg-Al Alloys, *Mater Trans* 52(7) (2011) 1477-1482.
- [18] U. Masood Chaudry, K. Hamad, J.-G. Kim, Ca-induced Plasticity in Magnesium Alloy: EBSD Measurements and VPSC Calculations, *Crystals* 10(2) (2020) 67.
- [19] I. Basu, T. Al-Samman, Triggering rare earth texture modification in magnesium alloys by addition of zinc and zirconium, *Acta Materialia* 67 (2014) 116-133.

- [20] S. Yi, J. Victoria-Hernandez, Y.M. Kim, D. Letzig, B.S. You, Modification of Microstructure and Texture in Highly Non-Flammable Mg-Al-Zn-Y-Ca Alloy Sheets by Controlled Thermomechanical Processes, *Metals-Basel* 9(2) (2019) 181.
- [21] J. Bohlen, M.R. Nürnberg, J.W. Senn, D. Letzig, S.R. Agnew, The texture and anisotropy of magnesium–zinc–rare earth alloy sheets, *Acta Materialia* 55(6) (2007) 2101-2112.
- [22] S.B. Yi, J. Bohlen, F. Heinemann, D. Letzig, Mechanical anisotropy and deep drawing behaviour of AZ31 and ZE10 magnesium alloy sheets, *Acta Materialia* 58(2) (2010) 592-605.
- [23] J.D. Robson, S.J. Haigh, B. Davis, D. Griffiths, Grain Boundary Segregation of Rare-Earth Elements in Magnesium Alloys, *Metallurgical and Materials Transactions A* 47(1) (2015) 522-530.
- [24] Z.R. Zeng, M.Z. Bian, S.W. Xu, C.H.J. Davies, N. Birbilis, J.F. Nie, Texture evolution during cold rolling of dilute Mg alloys, *Scripta Materialia* 108 (2015) 6-10.
- [25] S. Yi, Investigation on the Deformation Behavior and the Texture Evolution in Magnesium Wrought Alloy AZ31, Faculty of Natural and Materials Science, Clausthal University of Technology, 2005.
- [26] M.H. Yoo, J.R. Morris, K.M. Ho, S.R. Agnew, Nonbasal deformation modes of HCP metals and alloys: Role of dislocation source and mobility, *Metall Mater Trans A* 33(3) (2002) 813-822.
- [27] X. Zeng, P. Minárik, P. Dobroň, D. Letzig, K.U. Kainer, S. Yi, Role of deformation mechanisms and grain growth in microstructure evolution during recrystallization of Mg-Nd based alloys, *Scripta Materialia* 166 (2019) 53-57.
- [28] C. Ha, J. Bohlen, S. Yi, X. Zhou, H.-G. Brokmeier, N. Schell, D. Letzig, K.U. Kainer, Influence of Nd or Ca addition on the dislocation activity and texture changes of Mg–Zn alloy sheets under uniaxial tensile loading, *Materials Science and Engineering: A* 761 (2019) 138053.
- [29] S.R. Agnew, O. Duygulu, A mechanistic understanding of the formability of magnesium: Examining the role of temperature on the deformation mechanisms, *Mater Sci Forum* 419-4 (2003) 177-188.
- [30] J. Koike, T. Kobayashi, T. Mukai, H. Watanabe, M. Suzuki, K. Maruyama, K. Higashi, The activity of non-basal slip systems and dynamic recovery at room temperature in fine-grained AZ31B magnesium alloys, *Acta Materialia* 51(7) (2003) 2055-2065.
- [31] L. Mackenzie, M. Pekguleryuz, The recrystallization and texture of magnesium–zinc–cerium alloys, *Scripta Materialia* 59(6) (2008) 665-668.
- [32] I. Basu, T. Al-Samman, G. Gottstein, Shear band-related recrystallization and grain growth in two rolled magnesium-rare earth alloys, *Mat Sci Eng a-Struct* 579 (2013) 50-56.
- [33] E.A. Ball, P.B. Prangnell, Tensile-compressive yield asymmetries in high-strength wrought magnesium alloys, *Scripta Metall Mater* 31(2) (1994) 111-116.
- [34] K. Hantzsche, J. Wendt, K.U. Kainer, J. Bohlen, D. Letzig, Mg Sheet: The Effect of Process Parameters and Alloy Composition on Texture and Mechanical Properties, *Jom-U*s 61(8) (2009) 38-42.
- [35] G. Gottstein, *Physical Foundations of Materials Science*, Springer-Verlag Berlin Heidelberg, Berlin, Heidelberg, 2004.
- [36] P. Krishna, D. Pandey, Close-packed structures, *International Union of Crystallography Commission on Crystallographic Teaching* (5) 19.
- [37] W.D. Callister, *Materials Science and Engineering: An Introduction*, 7th ed., John Wiley and Sons Ltd 2006.

- [38] J.S. Suh, Improvement in Cold Formability of AZ31 Magnesium Alloy Sheets Processed by Equal Channel Angular Pressing (ECAP), Fakultät für Maschinenwesen, Technischen Universität München, 2015.
- [39] E. Schmid, W. Boas, Plasticity of crystals with special reference to metals, F. A. Hughes & Co. Limited, London, 1950.
- [40] A. Akhtar, E. Teghtsoonian, Solid solution strengthening of magnesium crystals-II the effect of solute on the ease of prismatic slip, *Acta Metallurgica* 17 (1969) 1351-1356.
- [41] A. Akhtar, E. Teghtsoonian, Solid solution strengthening of magnesium single crystals. 1. Alloying behaviour in basal slip, *Acta Metallurgica* 17 (1969) 1339-1349.
- [42] M.R. Barnett, A Taylor model based description of the proof stress of magnesium AZ31 during hot working, *Metall Mater Trans A* 34a(9) (2003) 1799-1806.
- [43] L.Y. Wang, Z.H. Huang, H.M. Wang, A. Maldar, S.B. Yi, J.S. Park, P. Kenesei, E. Lilleodden, X.Q. Zeng, Study of slip activity in a Mg-Y alloy by in situ high energy X-ray diffraction microscopy and elastic viscoplastic self-consistent modeling, *Acta Materialia* 155 (2018) 138-152.
- [44] J. Suh, J. Victoria-Hernández, D. Letzig, R. Golle, W. Volk, Enhanced mechanical behavior and reduced mechanical anisotropy of AZ31 Mg alloy sheet processed by ECAP, *Materials Science and Engineering: A* 650 (2016) 523-529.
- [45] J. Victoria-Hernández, J. Suh, S. Yi, J. Bohlen, W. Volk, D. Letzig, Strain-induced selective grain growth in AZ31 Mg alloy sheet deformed by equal channel angular pressing, *Materials Characterization* 113 (2016) 98-107.
- [46] G.I. Taylor, M.A. F.R.S., Plastic strain in metals, May lecture (1938) 307-324.
- [47] M.H. Yoo, Slip, twinning, and fracture in hexagonal close-packed metals, *Metall Trans A* 12(3) (1981) 409-418.
- [48] X.-L. Nan, H.-Y. Wang, L. Zhang, J.-B. Li, Q.-C. Jiang, Calculation of Schmid factors in magnesium: Analysis of deformation behaviors, *Scripta Materialia* 67(5) (2012) 443-446.
- [49] M.R. Barnett, Z. Keshavarz, X. Ma, A semianalytical Sachs model for the flow stress of a magnesium alloy, *Metall Mater Trans A* 37a(7) (2006) 2283-2293.
- [50] J. Čapek, Investigation of basic deformation mechanisms of magnesium alloys by means of advanced in-situ methods and theoretical modeling, *Physics of Materials*, Charles University, 2017.
- [51] S. Sandlöbes, M. Friák, S. Zaeferrer, A. Dick, S. Yi, D. Letzig, Z. Pei, L.F. Zhu, J. Neugebauer, D. Raabe, The relation between ductility and stacking fault energies in Mg and Mg-Y alloys, *Acta Materialia* 60(6-7) (2012) 3011-3021.
- [52] S. Sandlöbes, Z. Pei, M. Friák, L.F. Zhu, F. Wang, S. Zaeferrer, D. Raabe, J. Neugebauer, Ductility improvement of Mg alloys by solid solution: Ab initio modeling, synthesis and mechanical properties, *Acta Materialia* 70 (2014) 92-104.
- [53] A. Styczynski, C. Hartig, J. Bohlen, D. Letzig, Cold rolling textures in AZ31 wrought magnesium alloy, *Scripta Materialia* 50(7) (2004) 943-947.
- [54] K. Mathis, K. Nyilas, A. Axt, I. Dragomir-Cernatescu, T. Ungar, P. Lukac, The evolution of non-basal dislocations as a function of deformation temperature in pure magnesium determined by X-ray diffraction, *Acta Materialia* 52(10) (2004) 2889-2894.
- [55] K. Máthis, J. Gubicza, N.H. Nam, Microstructure and mechanical behavior of AZ91 Mg alloy processed by equal channel angular pressing, *Journal of Alloys and Compounds* 394(1-2) (2005) 194-199.
- [56] C. Ha, Dislocation activities in Mg-Nd and Mg-Ca alloy sheets with Zn as additional alloying element, *Materials Science and Engineering: A* (2020).
- [57] J.W. Christian, S. Mahajan, Deformation twinning, *Prog Mater Sci* 39(1-2) (1995) 1-157.

- [58] S.R. Agnew, Ö. Duygulu, Plastic anisotropy and the role of non-basal slip in magnesium alloy AZ31B, *Int J Plasticity* 21(6) (2005) 1161-1193.
- [59] Z. Zhong, In Situ Tensile Investigations on AA 7020-T6 Using Synchrotron Diffraction for Texture, Lattice Strain and Defect Density Studies, Faculty of Natural and Materials Science, Clausthal University of Technology, 2015.
- [60] H.J. Bunge, *Texture Analysis in Materials Science: Mathematical Methods*, Butterworth & Co, Berlin, 1969.
- [61] N. J. Park, H.T. Jeong, *Texture analysis Program system for Cubic and Hexagonal Crystal symmetry*, Hongreung publishing company 2011.
- [62] O. Engler, R. Valerie, *Introduction to texture analysis*, CRC Press, Taylor & Francis Group, 6000 Broken Sound Parkway NW, Suite 300, Boca Raton, FL 33487-2742, 2010.
- [63] Y.N. Wang, J.C. Huang, *Texture analysis in hexagonal materials*, *Materials Chemistry and Physics* 81(1) (2003) 11-26.
- [64] E. Tenckhoff, *Deformation mechanisms, texture, and anisotropy in zirconium and zircaloy*, ASTM special technical publication STP 966, 1988.
- [65] H.-G. Brokmeier, Hot rectangular extrusion textures of six Mg-Alloys via neutron diffraction, *Advanced Engineering Materials* 20(4) (2018) 1700234.
- [66] S.R. Agnew, C.N. Tomé, D.W. Brown, T.M. Holden, S.C. Vogel, Study of slip mechanisms in a magnesium alloy by neutron diffraction and modeling, *Scripta Materialia* 48(8) (2003) 1003-1008.
- [67] C. Ha, S. Yi, J. Bohlen, X. Zhou, H.-G. Brokmeier, N. Schell, D. Letzig, K.U. Kainer, Deformation and recrystallization mechanisms and their influence on the microstructure development of rare earth containing magnesium sheets, in: M. Technology (Ed.) TMS 2018 147th Annual Meeting and Exhibition, Phoenix, Arizona, 2018, pp. 209-216.
- [68] H.E. Friedrich, *Magnesium Technology*, Springer, 2006.
- [69] J. Gu, Grain refinement of Mg-Zn and Mg-Mn alloys by SiC inoculation, the Faculty of Natural and Materials Science, Clausthal University of Technology, Clausthal-Zellerfeld, 2017.
- [70] Y.M. Kim, C. Mendis, T. Sasaski, D. Letzig, F. Pyczak, K. Hono, S.B. Yi, Static recrystallization behaviour of cold rolled Mg-Zn-Y alloy and role of solute segregation in microstructure evolution, *Scripta Materialia* 136 (2017) 41-45.
- [71] M. Yuasa, M. Hayashi, M. Mabuchi, Y. Chino, Improved plastic anisotropy of Mg-Zn-Ca alloys exhibiting high-stretch formability: A first-principles study, *Acta Materialia* 65 (2014) 207-214.
- [72] D. Drozdenko, Study of novel magnesium alloys with controlled microstructure and texture, Department of Physics of Materials, Charles University, Prague, 2016, p. 84.
- [73] A. Galiyev, R. Kaibyshev, G. Gottstein, Correlation of plastic deformation and dynamic recrystallization in magnesium alloy Zk60, *Acta Materialia* 49(7) (2001) 1199-1207.
- [74] S.R. Agnew, J.A. Horton, M.H. Yoo, Transmission electron microscopy investigation of $\langle c+a \rangle$ dislocations in Mg and alpha-solid solution Mg-Li alloys, *Metall Mater Trans A* 33(3) (2002) 851-858.
- [75] S. Sandlöbes, M. Friák, J. Neugebauer, D. Raabe, Basal and non-basal dislocation slip in Mg-Y, *Materials Science and Engineering: A* 576 (2013) 61-68.
- [76] S. Sandlöbes, S. Zaeferrer, I. Schestakow, S. Yi, R. Gonzalez-Martinez, On the role of non-basal deformation mechanisms for the ductility of Mg and Mg-Y alloys, *Acta Materialia* 59(2) (2011) 429-439.
- [77] I.C. Dragomir, T. Ungar, Contrast factors of dislocations in the hexagonal crystal system, *J Appl Crystallogr* 35 (2002) 556-564.

- [78] G. Ribárik, Modeling of diffraction patterns based on microstructural properties, Materials Physics, Eötvös Loránd University, 2008.
- [79] T. Ungar, J. Gubicza, G. Ribarik, A. Borbely, Crystallite size distribution and dislocation structure determined by diffraction profile analysis: principles and practical application to cubic and hexagonal crystals, *J Appl Crystallogr* 34 (2001) 298-310.
- [80] N. Darowski, I. Zizak, G. Schumacher, H. Klingelhöffer, W. Chen, W. Neumann, Temperature dependence of x-ray intensity profile FWHM of the γ' phase in the creep-deformed single crystal superalloy SC16, *Journal of Physics D: Applied Physics* 38(10A) (2005) A200-A203.
- [81] A. Royer, P. Bastie, M. Veron, Temperature dependence of superstructure and fundamental reflections: study of a creep deformed single crystal nickel base superalloy AM1, *Mat Sci Eng a-Struct* 234 (1997) 1110-1113.
- [82] T. Ungár, A. Borbély, The effect of dislocation contrast on x-ray line broadening: A new approach to line profile analysis, *Applied Physics Letters* 69(21) (1996) 3173-3175.
- [83] R. Kuzel Jr, P. Klimanek, X-ray diffraction line broadening due to dislocations in non-cubic materials. II. The case of elastic anisotropy applied to hexagonal crystals, *J. Appl. Cryst.* 21 (1988) 363-368.
- [84] L. Wcislak, K. H., B.H. J., G. U., T. T., S.J. R., Texture analysis with high-energy synchrotron radiation, *J. Appl. Cryst.* 35 (2002) 82-95.
- [85] K. Máthis, J. Čapek, B. Clausen, T. Krajňák, D. Nagarajan, Investigation of the dependence of deformation mechanisms on solute content in polycrystalline Mg–Al magnesium alloys by neutron diffraction and acoustic emission, *Journal of Alloys and Compounds* 642 (2015) 185-191.
- [86] K. Mathis, G. Csiszar, J. Capek, J. Gubicza, B. Clausen, P. Lukas, A. Vinogradov, S.R. Agnew, Effect of the loading mode on the evolution of the deformation mechanisms in randomly textured magnesium polycrystals - Comparison of experimental and modeling results, *Int J Plasticity* 72 (2015) 127-150.
- [87] Z.Y. Zhong, H.G. Brokmeier, E. Maawad, N. Schell, In-situ investigation of the anisotropic mechanical behavior of rolled AA 7020-T6 alloy through lattice strain evolution during uniaxial tension, *Mat Sci Eng a-Struct* 639 (2015) 519-525.
- [88] T. Ungár, Microstructural parameters from X-ray diffraction peak broadening, *Scripta Materialia* 51(8) (2004) 777-781.
- [89] G.K. Williamson, W.H. Hall, X-Ray Line Broadening from Filed Aluminium and Wolfram, *Acta Metallurgica* 1(1) (1953) 22-31.
- [90] T. Ungar, G. Tichy, The effect of dislocation contrast on X-ray line profiles in untextured polycrystals, *Phys Status Solidi A* 171(2) (1999) 425-434.
- [91] J. Gubicza, S. Nauyoks, L. Balogh, J. Labar, T.W. Zerda, T. Ungar, Influence of sintering temperature and pressure on crystallite size and lattice defect structure in nanocrystalline SiC, *Journal of Materials Research* 22(5) (2007) 1314-1321.
- [92] M. Wilkens, The determination of density and distribution of dislocations in deformed single crystals from broadened X-Ray diffraction profiles, *phys. stat. sol. (a)* (2) (1970) 359-370.
- [93] P. Scardi, M. Leoni, Fourier modelling of the anisotropic line broadening of X-ray diffraction profiles due to line and plane lattice defects, *J Appl Crystallogr* 32(4) (1999) 671-682.
- [94] D. Louer, N. Audebrand, Profile fitting and diffraction line-broadening analysis, *JCPDS International Centre for Diffraction Data*, 1999, pp. 556–565.
- [95] J. Bahrtdt, H.-J. Baecker, W. Frentrup, A. Gaupp, M. Scheer, B. Schulz, U. Englisch, M. Tischer, Apple undulator for PETRA III, *Proceedings of EPAC08*, 2008, pp. 2219-2221.

- [96] K. Balewski, W. Brefeld, W. Decking, H. Franz, R. Rohlsberger, E. Weckert, PETRA III: A Low Emittance Synchrotron Radiation Source, Technical Design Report, 2004.
- [97] A.P. Hammersley, Installation europeene de rayonnement synchrotron, in: E.S.R. FACILITY (Ed.) ESRF Internal Report, 2004.
- [98] F. Bachmann, R. Hielscher, H. Schaeben, Texture Analysis with MTEX – Free and Open Source Software Toolbox, *Solid State Phenomena* 160 (2010) 63-68.
- [99] V. Kree, J. Bohlen, D. Letzig, K.U. Kainer, The metallographical examination of magnesium alloys, *Prakt Metallogr-Pr M* 41(5) (2004) 233-246.
- [100] Y.B. Chun, M. Battaini, C.H.J. Davies, S.K. Hwang, Distribution characteristics of in-grain misorientation axes in cold-rolled commercially pure titanium and their correlation with active slip modes, *Metall Mater Trans A* 41a(13) (2010) 3473-3487.
- [101] J.P. Hadorn, K. Hantzsche, S.B. Yi, J. Bohlen, D. Letzig, J.A. Wollmershauser, S.R. Agnew, Role of Solute in the Texture Modification During Hot Deformation of Mg-Rare Earth Alloys, *Metall Mater Trans A* 43a(4) (2012) 1347-1362.
- [102] Y.Q. Cheng, Z.H. Chen, W.J. Xia, Drawability of AZ31 magnesium alloy sheet produced by equal channel angular rolling at room temperature, *Materials Characterization* 58(7) (2007) 617-622.
- [103] J. Victoria-Hernandez, S. Yi, J. Bohlen, G. Kurz, D. Letzig, The influence of the recrystallization mechanisms and grain growth on the texture of a hot rolled AZ31 sheet during subsequent isochronal annealing, *Journal of Alloys and Compounds* 616 (2014) 189-197.
- [104] D. Guan, W.M. Rainforth, J. Gao, J. Sharp, B. Wynne, L. Ma, Individual effect of recrystallisation nucleation sites on texture weakening in a magnesium alloy: Part 1-double twins, *Acta Materialia* 135 (2017) 14-24.
- [105] J.-Y. Lee, Y.-S. Yun, B.-C. Suh, N.-J. Kim, W.-T. Kim, D.-H. Kim, Comparison of static recrystallization behavior in hot rolled Mg–3Al–1Zn and Mg–3Zn–0.5Ca sheets, *Journal of Alloys and Compounds* 589 (2014) 240-246.
- [106] Q. Zhang, L. Fu, T.-W. Fan, B.-Y. Tang, L.-M. Peng, W.-J. Ding, Ab initio study of the effect of solute atoms Zn and Y on stacking faults in Mg solid solution, *Physica B: Condensed Matter* 416 (2013) 39-44.
- [107] M.H. Yoo, S.R. Agnew, J.R. Morris, K.M. Ho, Non-basal slip systems in HCP metals and alloys: source mechanisms, *Mat Sci Eng a-Struct* 319 (2001) 87-92.
- [108] M. Sanjari, A.R. Farkoosh, B. Shalchi Amirkhiz, Y. He, A. Javid, A.S. Kabir, J. Su, I.-H. Jung, S. Yue, The role of the Zn/Nd ratio in the microstructural evolution of the Mg-Zn-Nd system during static recrystallization: Grain boundary partitioning of solutes, *Scripta Materialia* 134 (2017) 1-5.
- [109] T. Wang, J.J. Jonas, H. Qin, S. Yue, Effect of dynamic strain aging on the deformation and twinning behavior of a Mg–2Zn–2Nd alloy, *Materials Science and Engineering: A* 645 (2015) 126-135.
- [110] T. Wang, L. Jiang, R.K. Mishra, J.J. Jonas, Effect of Ca Addition on the Intensity of the Rare Earth Texture Component in Extruded Magnesium Alloys, *Metallurgical and Materials Transactions A* 45(10) (2014) 4698-4709.
- [111] S.M. Zhu, J.F. Nie, Serrated flow and tensile properties of a Mg–Y–Nd alloy, *Scripta Materialia* 50(1) (2004) 51-55.
- [112] D. Wu, R.S. Chen, E.H. Han, Serrated flow and tensile properties of a Mg–Gd–Zn alloy, *Materials Science and Engineering: A* 532 (2012) 267-274.
- [113] N. Stanford, I. Sabirov, G. Sha, A. La Fontaine, S.P. Ringer, M.R. Barnett, Effect of Al and Gd Solutes on the Strain Rate Sensitivity of Magnesium Alloys, *Metallurgical and Materials Transactions A* 41(3) (2010) 734-743.

-
- [114] F.J. Humphreys, M. Hatherly, Recrystallization and related annealing phenomena, Elsevier Ltd, Kidlington, Oxford OX5 1GB, UK, 2004.
- [115] S.E. Ion, F.J. Humphreys, S.H. White, Dynamic recrystallization and the development of microstructure during the high-temperature deformation of magnesium, *Acta Metallurgica* 30(10) (1982) 11.
- [116] A.K. Mahato, The effect of composition and temperature on the deformation behaviour of magnesium-aluminium binary alloys, Institute of Frontier Materials, Deakin University, Australia, 2016, p. 155.
- [117] P. Lukac, Hardening and Softening during Plastic-Deformation of Hexagonal Metals, *Czech J Phys* 35(3) (1985) 275-285.
- [118] Z.R. Zeng, Y.M. Zhu, S.W. Xu, M.Z. Bian, C.H.J. Davies, N. Birbilis, J.F. Nie, Texture evolution during static recrystallization of cold-rolled magnesium alloys, *Acta Materialia* 105 (2016) 479-494.

Appendix

List of symbols and abbreviations

a	lattice parameter in a hexagonal close-packed structure
AZ31	Mg-Al-Zn alloy
\vec{b} or b	Burgers vector
BE	basal edge dislocation
c	lattice parameter in a hexagonal close-packed structure
Ca	calcium
Ce	cerium
CMWP	convolutional multiple whole profile
CRSS	critical resolved shear stress
DESY	Deutsches Elektronen-Synchrotron
DIN	<i>Deutsches Institut für Normung</i>
DRV	dynamic recovery
DRX	dynamic recrystallization
DSA	dynamic strain aging
d_s	slip direction for given slip, s
EBSA	electron backscattered diffraction
$f(\eta)$	Wilkens function
FCC	face-centered cubic
FE-SEM	field emission gun scanning electron microscope
FS	fracture strain
FWHM	full width at half maximum
g	diffraction vector
Gd	Gadolinium

GOS	grain orientation spread
HCP	hexagonal close-packed
HEMS	High Energy Material Science
h_i	fractions of populated dislocations
IGMA	in-grain misorientation axes
KAM	kernel average misorientation
L	Fourier variable
La	lanthanum
Mg	magnesium
m.r.d.	multiple of a random distribution
N05	Mg-0.61Nd (wt.%)
Nd	neodymium
ND	normal direction
n_s	normal slip plane for given slip, s
ODF	orientation distribution function
OIM	orientation image mapping
OPS	oxide polishing suspension
$P_{hkl}(\alpha, \beta)$	pole figure, measured pole density distribution functions
P_{\max}	maximum intensity of pole figure
PETRA III	beamline in DESY
PrE, Pr2E, and Pr3E	prismatic edge dislocations
PSN	particle-simulated nucleation
PyE, Py2E, Py3E, and Py4E	pyramidal edge dislocations
q_1 or q_2	parameter depending on anisotropic elastic properties

RD	rolling direction
R_e	effective outer cut-off radius
RE	rare earth
RSS (τ)	resolved shear stress
RT	room temperature
S_0	cross sectional area of a single crystalline cylinder
S1, S2, and S3	screw dislocation
SFE	stacking fault energy
TD	transverse direction
TEM	transmission electron microscopy
TRC	twin-roll casting
T_s	Taylor axis
UTM	universal testing machine
UTS	ultimate tensile strength
X05	Mg-0.52Ca (wt.%)
XRD	X-ray diffractometer
Y	Yttrium
YS	yield strength
ZK10	Mg-1.32Zn-0.13Zr (wt.%)
Zn	Zinc
ZN10	Mg-1.03Zn-0.73Nd (wt.%)
Zr	Zirconium
ZX10	Mg-0.91Zn-0.54Ca (wt.%)
\overline{C}_{hkl}	dislocation contrast factor
ρ_{Al}	density of aluminum
ρ_{Mg}	density of magnesium

ρ	dislocation density
σ	Stress
ε	strain
m	Schmid factor
ξ_s	angle between slip direction and loading direction
λ	wavelength of X-ray
θ	diffraction angle
ϕ	angle between normal axis of slip plane and applied load direction
ω	omega angle
γ	azimuth angle along the Debye-Scherrer ring
$\langle \varepsilon_{g,L}^2 \rangle$	mean-squared strain

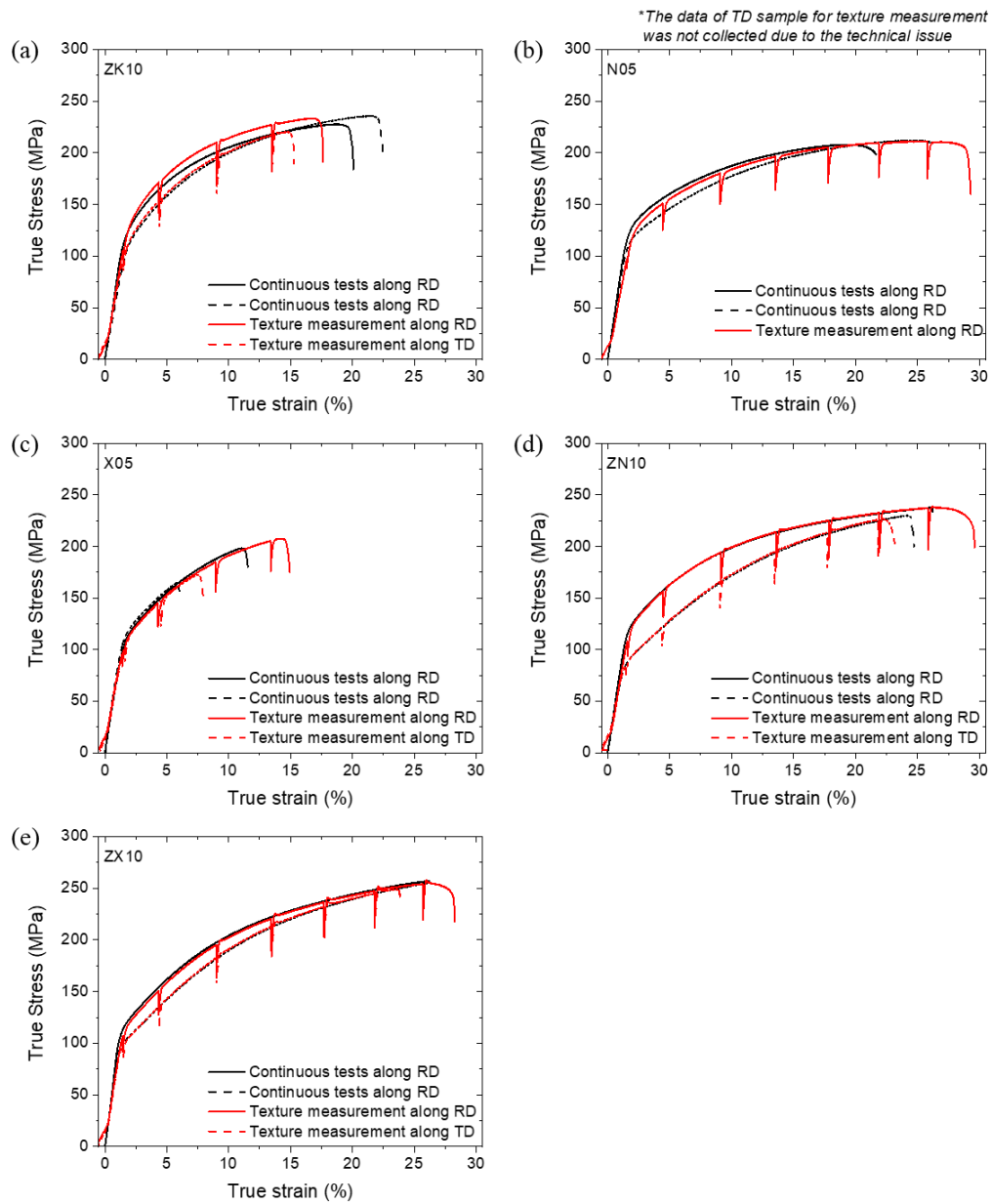
Stress-strain curves acquired from the two *in-situ* experiments at RT

Fig. A.1 True stress-strain curves acquired from the two *in-situ* experiments during the tensile tests along the RD and TD at RT of all examined sheets; (a) ZK10, (b) N05, (c) X05, (d) ZN10, and (e) ZX10.

Phase diagrams

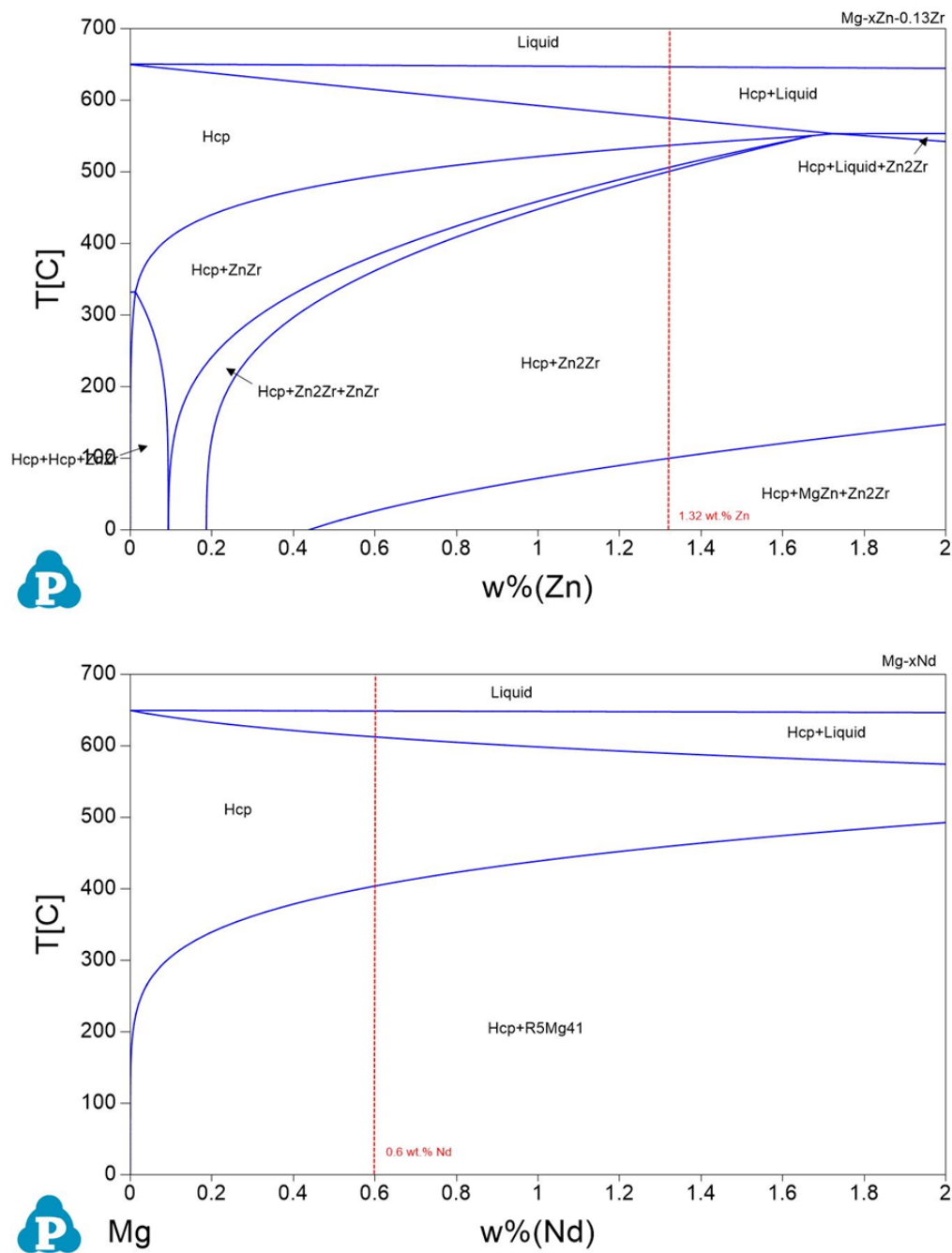


Fig. A.2 Equilibrium binary phase diagram for the examined alloys. The composition of each examined alloy is marked as dash line in the phase diagrams (continue to next page).

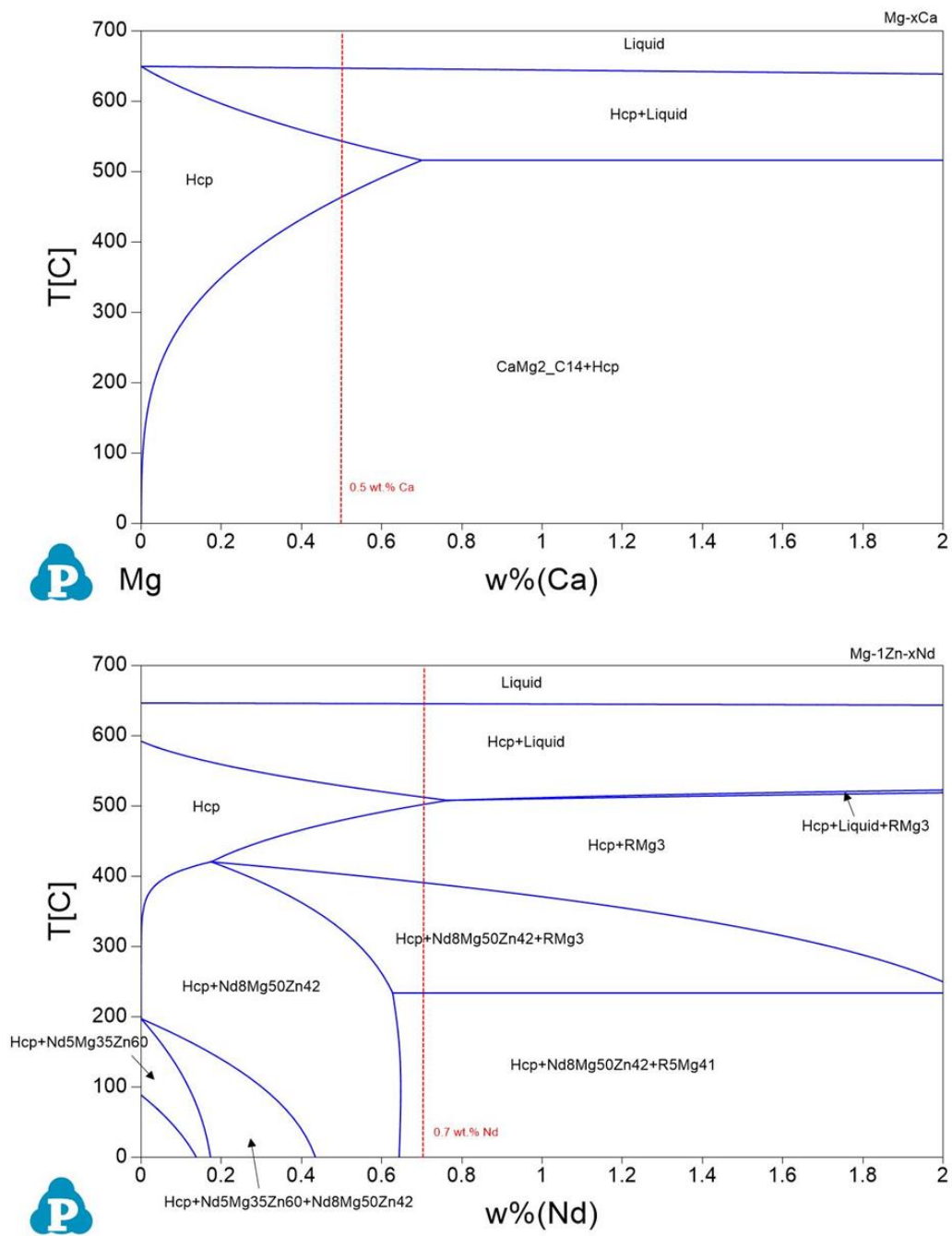


Fig. A.2 continue

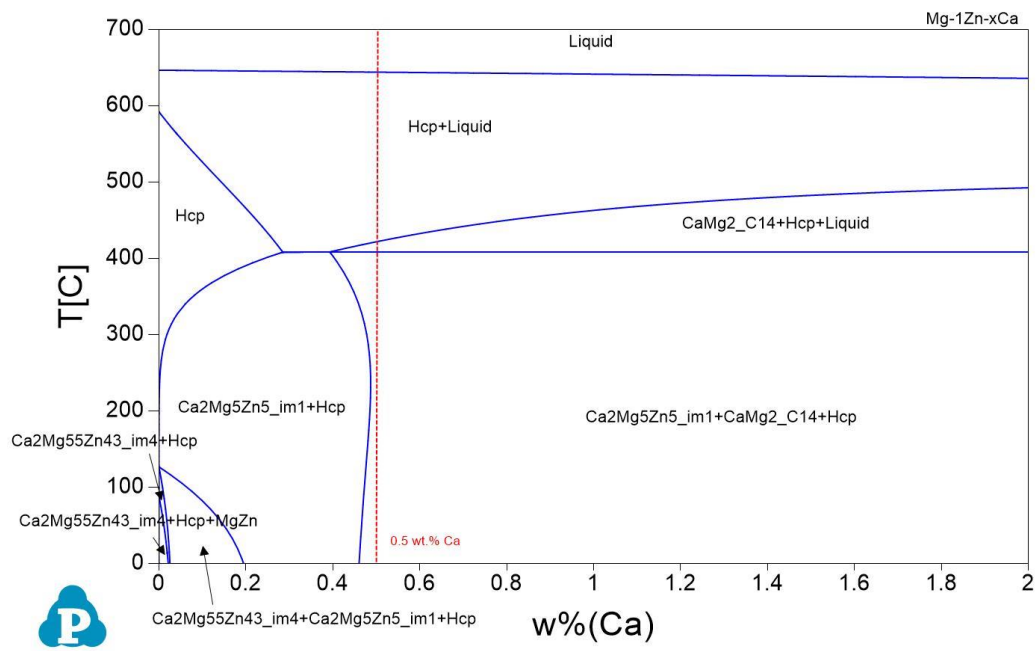


Fig. A.2 continue

Dislocation activities obtained from the CMWP analysis

Table A.1 Overall dislocation densities obtained from CMWP analysis as a function of the strain along the RD and TD in examined sheets (density unit: $1 \times 10^{14} \text{m}^{-2}$)

Alloy	RD Loading					
	0%	2%	5%	10%	15%	20%
ZK10	2.56±0.04	2.84±0.05	3.62±0.04	4.41±0.05	4.84±0.04	4.90±0.04
N05	2.85±0.06	3.18±0.04	4.44±0.06	4.98±0.05	5.28±0.05	5.61±0.05
X05	2.80±0.06	3.37±0.05	4.56±0.04	5.24±0.05	5.91±0.06	-
ZN10	2.54±0.04	3.28±0.05	4.78±0.08	5.70±0.08	6.20±0.10	6.61±0.11
ZX10	2.53±0.04	3.16±0.06	4.71±0.09	5.76±0.09	6.38±0.10	6.84±0.07

Alloy	TD Loading					
	0%	2%	5%	10%	15%	20%
ZK10	2.40±0.04	2.68±0.04	3.77±0.05	4.49±0.05	4.90±0.05	-
N05	2.49±0.04	3.11±0.04	4.42±0.03	4.97±0.04	5.16±0.04	5.57±0.04
X05	2.60±0.07	3.22±0.04	4.20±0.04	-	-	-
ZN10	2.57±2.99	3.20±1.32	4.40±0.88	4.89±1.06	5.65±1.11	5.80±1.05
ZX10	2.33±0.06	3.14±0.04	4.36±0.04	5.19±0.07	5.81±0.07	6.28±0.08

Table A.2 The dislocation densities obtained from the CMWP analysis based on the Burgers vector, $\langle a \rangle$, $\langle c \rangle$, and $\langle c+a \rangle$ types, as a function of the strain along the RD and TD in examined sheets (density unit: $1 \times 10^{14} \text{ m}^{-2}$)

Alloy	Type	RD loading										TD Loading									
		0%	2%	5%	10%	15%	20%	0%	2%	5%	10%	15%	20%								
ZK10	$\langle a \rangle$	1.91±0.15	1.81±0.24	2.38±0.23	3.08±0.20	3.40±0.21	3.33±0.20	1.67±0.19	1.93±0.26	2.51±0.71	2.89±0.19	3.18±0.18	-								
	$\langle c \rangle$	0.26±0.02	0.37±0.02	0.52±0.05	0.44±0.04	0.49±0.04	0.41±0.03	0.48±0.04	0.52±0.05	0.45±0.04	0.30±0.02	0.32±0.02	-								
	$\langle c+a \rangle$	0.38±0.03	0.65±0.09	0.73±0.10	0.89±0.05	0.95±0.06	1.16±0.07	0.25±0.01	0.20±0.02	0.82±0.06	1.30±0.08	1.40±0.08	-								
N05	$\langle a \rangle$	2.06±0.18	2.29±0.22	3.27±0.22	3.57±0.20	3.67±0.19	3.80±0.18	1.75±0.17	2.27±0.18	3.02±0.17	3.41±0.18	3.42±0.17	3.64±0.16								
	$\langle c \rangle$	0.48±0.03	0.41±0.02	0.47±0.04	0.40±0.03	0.34±0.02	0.28±0.01	0.70±0.07	0.60±0.04	0.32±0.02	0.32±0.02	0.32±0.02	0.26±0.01								
	$\langle c+a \rangle$	0.31±0.02	0.48±0.03	0.70±0.05	1.01±0.05	1.27±0.06	1.53±0.07	0.04±0.00	0.24±0.01	1.08±0.06	1.23±0.06	1.42±0.08	1.67±0.07								
X05	$\langle a \rangle$	2.12±0.16	2.51±0.22	3.43±0.19	3.77±0.19	4.22±0.19	-	-	2.49±0.25	3.05±0.22	-	-	-								
	$\langle c \rangle$	0.27±0.01	0.34±0.02	0.39±0.03	0.34±0.02	0.29±0.01	-	-	0.67±0.07	0.48±0.04	-	-	-								
	$\langle c+a \rangle$	0.41±0.03	0.52±0.04	0.74±0.04	1.13±0.05	1.40±0.06	-	-	0.06±0.00	0.67±0.05	-	-	-								
ZN10	$\langle a \rangle$	1.87±0.15	2.42±0.17	3.52±0.16	4.05±0.15	4.40±0.15	4.69±0.15	1.81±0.16	2.36±0.22	3.24±0.24	3.43±0.23	3.98±0.21	3.91±0.20								
	$\langle c \rangle$	0.27±0.02	0.36±0.03	0.24±0.01	0.24±0.01	0.23±0.01	0.22±0.01	0.67±0.05	0.39±0.02	0.51±0.04	0.50±0.04	0.36±0.02	0.38±0.02								
	$\langle c+a \rangle$	0.40±0.04	0.50±0.04	1.01±0.04	1.41±0.05	1.57±0.05	1.70±0.05	0.09±0.00	0.45±0.03	0.65±0.06	0.96±0.06	1.31±0.07	1.51±0.08								
ZX10	$\langle a \rangle$	1.86±0.16	2.27±0.14	3.34±0.15	4.00±0.14	4.44±0.16	4.79±0.17	1.65±0.14	2.36±0.17	3.19±0.17	3.56±0.18	3.96±0.19	4.22±0.20								
	$\langle c \rangle$	0.28±0.02	0.30±0.02	0.22±0.01	0.24±0.01	0.27±0.01	0.30±0.01	0.58±0.05	0.24±0.03	0.35±0.02	0.32±0.02	0.34±0.02	0.34±0.02								
	$\langle c+a \rangle$	0.38±0.04	0.59±0.03	1.15±0.05	1.52±0.05	1.67±0.06	1.75±0.07	0.09±0.00	0.44±0.03	0.82±0.02	1.32±0.02	1.52±0.02	1.71±0.02								

Table A.3 The densities of basal <a> and non-basal <a> dislocations and their ratio to overall dislocation density obtained from the CMWP analysis as a function of the strain along the RD and TD in examined sheets and (density unit: $1 \times 10^{14} \text{ m}^{-2}$ and ratio: $\rho_{basal} <a> / \rho_{total}$ and $\rho_{non-basal} <a> / \rho_{total}$, in brackets respectively)

Alloy	Type	RD loading										TD Loading									
		0%	2%	5%	10%	15%	20%	0%	2%	5%	10%	15%	20%								
ZK10	Basal <a>	0.55	0.53	0.70	0.72	0.79	0.72	0.41	0.36	0.68	0.55	0.61	-								
	(ratio)	(0.21)	(0.19)	(0.19)	(0.16)	(0.16)	(0.15)	(0.17)	(0.13)	(0.18)	(0.12)	(0.12)	-								
N05	Non-basal <a>	0.95	0.84	1.15	1.86	2.07	2.15	0.70	0.87	1.39	2.03	2.23	-								
	(ratio)	(0.37)	(0.30)	(0.32)	(0.42)	(0.43)	(0.44)	(0.29)	(0.33)	(0.37)	(0.45)	(0.46)	-								
X05	Basal <a>	0.60	0.70	0.81	0.75	0.64	0.53	0.11	0.51	0.61	0.61	0.58	0.45								
	(ratio)	(0.21)	(0.22)	(0.18)	(0.15)	(0.12)	(0.09)	(0.05)	(0.16)	(0.14)	(0.12)	(0.11)	(0.08)								
ZN10	Non-basal <a>	1.03	1.06	1.95	2.34	2.71	3.03	1.06	1.24	2.09	2.52	2.57	2.99								
	(ratio)	(0.36)	(0.34)	(0.44)	(0.47)	(0.51)	(0.54)	(0.43)	(0.40)	(0.47)	(0.51)	(0.50)	(0.54)								
ZX10	Basal <a>	0.54	0.69	0.68	0.67	0.56	-	-	0.22	0.80	-	-	-								
	(ratio)	(0.19)	(0.20)	(0.15)	(0.13)	(0.09)	-	-	(0.07)	(0.19)	-	-	-								
ZK10	Non-basal <a>	1.10	1.27	2.28	2.85	3.52	-	-	1.35	1.77	-	-	-								
	(ratio)	(0.39)	(0.38)	(0.50)	(0.54)	(0.59)	-	-	(0.42)	(0.42)	-	-	-								
ZN10	Basal <a>	0.48	0.59	0.53	0.39	0.42	0.35	0.32	0.72	0.86	0.85	0.73	0.69								
	(ratio)	(0.19)	(0.18)	(0.11)	(0.07)	(0.07)	(0.05)	(0.12)	(0.23)	(0.20)	(0.17)	(0.13)	(0.12)								
ZX10	Non-basal <a>	0.95	1.44	2.86	3.61	3.98	4.34	0.98	1.10	1.86	2.01	2.92	2.86								
	(ratio)	(0.37)	(0.44)	(0.60)	(0.63)	(0.64)	(0.66)	(0.38)	(0.34)	(0.42)	(0.41)	(0.52)	(0.49)								
ZK10	Basal <a>	0.49	0.50	0.46	0.34	0.38	0.46	0.29	0.64	0.63	0.63	0.66	0.66								
	(ratio)	(0.19)	(0.16)	(0.10)	(0.06)	(0.06)	(0.07)	(0.12)	(0.20)	(0.15)	(0.12)	(0.11)	(0.11)								
ZX10	Non-basal <a>	0.92	1.44	2.75	3.58	3.98	4.27	0.90	1.30	2.18	2.68	3.06	3.33								
	(ratio)	(0.36)	(0.45)	(0.58)	(0.62)	(0.62)	(0.62)	(0.39)	(0.41)	(0.50)	(0.52)	(0.53)	(0.53)								

Table. A.4 Overall dislocation densities and densities based on the $\langle a \rangle$, $\langle c \rangle$, and $\langle c+a \rangle$ dislocations, obtained from CMWP analysis as a function of the strain along the RD at RT, 100°C, and 200°C in ZK10 (ρ_{total} : overall dislocation, $\rho_{\langle a \rangle}$: $\langle a \rangle$ dislocation, $\rho_{\langle c \rangle}$: $\langle c \rangle$ dislocation, and $\rho_{\langle c+a \rangle}$: $\langle c+a \rangle$ dislocation densities, $\rho_{basal \langle a \rangle}$ and $\rho_{non-basal \langle a \rangle}$: ratio of basal $\langle a \rangle$ and non-basal $\langle a \rangle$ dislocations with unit: $1 \times 10^{14} \text{ m}^{-2}$; ratio: $\rho_{basal \langle a \rangle} / \rho_{total}$ and $\rho_{non-basal \langle a \rangle} / \rho_{total}$, in brackets)

Dislocation density	at RT					
	0%	2%	5%	10%	15%	20%
ρ_{total}	2.56±0.04	2.84±0.05	3.62±0.04	4.41±0.05	4.84±0.04	4.90±0.04
$\rho_{\langle a \rangle}$	1.91±0.15	1.81±0.24	2.38±0.23	3.08±0.20	3.40±0.21	3.33±0.20
$\rho_{\langle c \rangle}$	0.26±0.02	0.37±0.02	0.52±0.05	0.44±0.04	0.49±0.04	0.41±0.03
$\rho_{\langle c+a \rangle}$	0.38±0.03	0.65±0.09	0.73±0.10	0.89±0.05	0.95±0.06	1.16±0.07
$\rho_{basal \langle a \rangle}$ (ratio)	0.55 (0.21)	0.53 (0.19)	0.70 (0.19)	0.72 (0.16)	0.79 (0.16)	0.72 (0.15)
$\rho_{nonbasal \langle a \rangle}$ (ratio)	0.95 (0.37)	0.84 (0.30)	1.15 (0.32)	1.86 (0.42)	2.07 (0.43)	2.15 (0.44)

Dislocation density	at 100°C					
	0%	2%	5%	10%	15%	20%
ρ_{total}	2.91±0.05	3.24±0.04	3.84±0.05	4.42±0.04	4.77±0.04	5.05±0.03
$\rho_{\langle a \rangle}$	2.13±0.16	2.26±0.22	2.68±0.21	3.18±0.16	3.32±0.11	3.51±0.09
$\rho_{\langle c \rangle}$	0.33±0.03	0.40±0.03	0.53±0.05	0.30±0.02	0.20±0.01	0.15±0.00
$\rho_{\langle c+a \rangle}$	0.44±0.04	0.58±0.07	0.63±0.06	0.94±0.05	1.25±0.04	1.39±0.03
$\rho_{basal \langle a \rangle}$ (ratio)	0.59 (0.20)	0.61 (0.19)	0.70 (0.18)	0.59 (0.13)	0.30 (0.06)	0.14 (0.03)
$\rho_{nonbasal \langle a \rangle}$ (ratio)	1.17 (0.40)	1.08 (0.33)	1.54 (0.40)	2.34 (0.53)	3.02 (0.63)	3.37 (0.67)

Dislocation density	at 200°C					
	0%	2%	5%	10%	15%	20%
ρ_{total}	3.22±0.13	2.89±0.10	3.12±0.12	3.28±0.13	3.71±0.10	3.96±0.07
$\rho_{\langle a \rangle}$	2.44±0.47	1.99±0.50	2.22±0.38	2.41±0.36	2.87±0.38	3.07±0.25
$\rho_{\langle c \rangle}$	0.47±0.03	0.50±0.03	0.38±0.03	0.36±0.03	0.38±0.03	0.25±0.01
$\rho_{\langle c+a \rangle}$	0.32±0.02	0.40±0.03	0.52±0.04	0.52±0.04	0.47±0.03	0.63±0.03
$\rho_{basal \langle a \rangle}$	0.70 (0.22)	0.55 (0.19)	0.57 (0.18)	0.59 (0.18)	0.60 (0.16)	0.56 (0.14)
$\rho_{nonbasal \langle a \rangle}$	1.23 (0.38)	0.94 (0.32)	1.28 (0.41)	1.43 (0.44)	1.85 (0.50)	2.38 (0.60)

Table. A.5 Overall dislocation densities and densities based on the $\langle a \rangle$, $\langle c \rangle$, and $\langle c+a \rangle$ dislocations, obtained from CMWP analysis as a function of the strain along the RD at AR, 100°C, and 200°C in N05 (ρ_{total} : overall dislocation, $\rho_{\langle a \rangle}$: $\langle a \rangle$ dislocation, $\rho_{\langle c \rangle}$: $\langle c \rangle$ dislocation, and $\rho_{\langle c+a \rangle}$: $\langle c+a \rangle$ dislocation densities, $\rho_{basal \langle a \rangle}$ and $\rho_{non-basal \langle a \rangle}$: ratio of basal $\langle a \rangle$ and non-basal $\langle a \rangle$ dislocations with unit: $1 \times 10^{14} \text{ m}^{-2}$; ratio: $\rho_{basal \langle a \rangle} / \rho_{total}$ and $\rho_{non-basal \langle a \rangle} / \rho_{total}$, in brackets)

Dislocation density	at RT					
	0%	2%	5%	10%	15%	20%
ρ_{total}	2.85±0.06	3.18±0.04	4.44±0.06	4.98±0.05	5.28±0.05	5.61±0.05
$\rho_{\langle a \rangle}$	2.06±0.18	2.29±0.22	3.27±0.22	3.57±0.20	3.67±0.19	3.80±0.18
$\rho_{\langle c \rangle}$	0.48±0.03	0.41±0.02	0.47±0.02	0.40±0.03	0.34±0.02	0.28±0.01
$\rho_{\langle c+a \rangle}$	0.31±0.02	0.48±0.03	0.70±0.05	1.01±0.05	1.27±0.06	1.61±0.07
$\rho_{basal \langle a \rangle}$ (ratio)	0.60 (0.21)	0.70 (0.22)	0.81 (0.18)	0.75 (0.15)	0.64 (0.12)	0.53 (0.09)
$\rho_{nonbasal \langle a \rangle}$ (ratio)	1.03 (0.36)	1.06 (0.34)	1.95 (0.44)	2.34 (0.47)	2.71 (0.51)	3.03 (0.54)

Dislocation density	at 100°C					
	0%	2%	5%	10%	15%	20%
ρ_{total}	3.18±0.07	3.93±0.08	4.44±0.09	4.85±0.09	5.19±0.11	5.45±0.08
$\rho_{\langle a \rangle}$	2.24±0.20	2.91±0.15	3.14±0.16	3.35±0.15	3.61±0.14	3.82±0.13
$\rho_{\langle c \rangle}$	0.38±0.02	0.31±0.02	0.29±0.02	0.24±0.01	0.23±0.01	0.18±0.01
$\rho_{\langle c+a \rangle}$	0.57±0.06	0.70±0.04	1.02±0.05	1.26±0.06	1.35±0.06	1.45±0.05
$\rho_{basal \langle a \rangle}$ (ratio)	0.60 (0.19)	0.57 (0.14)	0.56 (0.13)	0.47 (0.10)	0.40 (0.08)	0.38 (0.07)
$\rho_{nonbasal \langle a \rangle}$ (ratio)	1.08 (0.34)	1.99 (0.51)	2.34 (0.53)	2.76 (0.57)	3.16 (0.61)	3.44 (0.63)

Dislocation density	at 200°C					
	0%	2%	5%	10%	15%	20%
ρ_{total}	3.57±0.07	3.72±0.10	4.15±0.07	4.74±0.07	-	-
$\rho_{\langle a \rangle}$	2.70±0.20	2.65±0.25	3.03±0.23	3.34±0.15	-	-
$\rho_{\langle c \rangle}$	0.38±0.02	0.44±0.03	0.47±0.04	0.25±0.01	-	-
$\rho_{\langle c+a \rangle}$	0.49±0.04	0.63±0.07	0.65±0.06	1.15±0.05	-	-
$\rho_{basal \langle a \rangle}$	0.77 (0.22)	0.70 (0.19)	0.85 (0.21)	0.49 (0.10)	-	-
$\rho_{nonbasal \langle a \rangle}$	1.34 (0.38)	1.29 (0.35)	1.60 (0.38)	2.72 (0.57)	-	-

Table. A.6 Overall dislocation densities and densities based on the $\langle a \rangle$, $\langle c \rangle$, and $\langle c+a \rangle$ dislocations, obtained from CMWP analysis as a function of the strain along the RD at RT, 100°C, and 200°C in X05 (ρ_{total} : overall dislocation, $\rho_{\langle a \rangle}$: $\langle a \rangle$ dislocation, $\rho_{\langle c \rangle}$: $\langle c \rangle$ dislocation, and $\rho_{\langle c+a \rangle}$: $\langle c+a \rangle$ dislocation densities, $\rho_{basal \langle a \rangle}$ and $\rho_{non-basal \langle a \rangle}$: ratio of basal $\langle a \rangle$ and non-basal $\langle a \rangle$ dislocations with unit: $1 \times 10^{14} \text{ m}^{-2}$; ratio: $\rho_{basal \langle a \rangle} / \rho_{total}$ and $\rho_{non-basal \langle a \rangle} / \rho_{total}$, in brackets)

Dislocation density	at RT					
	0%	2%	5%	10%	15%	20%
ρ_{total}	2.80±0.06	3.37±0.05	4.56±0.04	5.24±0.05	5.91±0.06	-
$\rho_{\langle a \rangle}$	2.12±0.16	2.51±0.22	3.43±0.19	3.77±0.19	4.22±0.19	-
$\rho_{\langle c \rangle}$	0.27±0.01	0.34±0.02	0.39±0.03	0.34±0.02	0.29±0.01	-
$\rho_{\langle c+a \rangle}$	0.41±0.03	0.52±0.04	0.74±0.04	1.13±0.05	1.4±0.06	-
$\rho_{basal \langle a \rangle}$ (ratio)	0.54 (0.19)	0.69 (0.20)	0.68 (0.15)	0.67 (0.13)	0.56 (0.09)	-
$\rho_{nonbasal \langle a \rangle}$ (ratio)	1.10 (0.39)	1.27 (0.38)	2.28 (0.50)	2.85 (0.54)	3.52 (0.59)	-

Dislocation density	at 100°C					
	0%	2%	5%	10%	15%	20%
ρ_{total}	3.00±0.07	3.76±0.07	4.61±0.07	5.24±0.07	5.75±0.06	6.21±0.07
$\rho_{\langle a \rangle}$	2.10±0.21	2.78±0.17	3.38±0.16	3.74±0.17	4.03±0.14	4.36±0.14
$\rho_{\langle c \rangle}$	0.54±0.04	0.35±0.03	0.27±0.01	0.25±0.01	0.25±0.01	0.21±0.01
$\rho_{\langle c+a \rangle}$	0.36±0.02	0.35±0.02	0.96±0.04	1.25±0.06	1.47±0.05	1.64±0.05
$\rho_{basal \langle a \rangle}$ (ratio)	0.58 (0.19)	0.58 (0.15)	0.57 (0.12)	0.51 (0.10)	0.35 (0.06)	0.34 (0.06)
$\rho_{nonbasal \langle a \rangle}$ (ratio)	0.99 (0.33)	1.82 (0.48)	2.62 (0.57)	3.14 (0.60)	3.61 (0.63)	4.01 (0.65)

Dislocation density	at 200°C					
	0%	2%	5%	10%	15%	20%
ρ_{total}	3.14±0.08	2.85±0.07	3.73±0.09	4.16±0.05	4.77±0.05	5.21±0.05
$\rho_{\langle a \rangle}$	2.37±0.24	2.11±0.19	2.88±0.21	3.11±0.16	3.32±0.04	3.67±0.04
$\rho_{\langle c \rangle}$	0.65±0.06	0.30±0.02	0.33±0.02	0.32±0.02	0.15±0.00	0.14±0.00
$\rho_{\langle c+a \rangle}$	0.12±0.00	0.44±0.04	0.52±0.04	0.73±0.03	1.30±0.03	1.40±0.03
$\rho_{basal \langle a \rangle}$	0.38 (0.12)	0.57 (0.20)	0.81 (0.22)	0.60 (0.15)	0.00 (0.00)	0.00 (0.00)
$\rho_{nonbasal \langle a \rangle}$	1.19 (0.38)	1.07 (0.37)	1.47 (0.39)	2.20 (0.53)	3.32 (0.70)	3.67 (0.71)

Table. A.7 Overall dislocation densities and densities based on the $\langle a \rangle$, $\langle c \rangle$, and $\langle c+a \rangle$ dislocations, obtained from CMWP analysis as a function of the strain along the RD at RT, 100°C, and 200°C in ZN10 (ρ_{total} : overall dislocation, $\rho_{\langle a \rangle}$: $\langle a \rangle$ dislocation, $\rho_{\langle c \rangle}$: $\langle c \rangle$ dislocation, and $\rho_{\langle c+a \rangle}$: $\langle c+a \rangle$ dislocation densities, $\rho_{basal \langle a \rangle}$ and $\rho_{non-basal \langle a \rangle}$: ratio of basal $\langle a \rangle$ and non-basal $\langle a \rangle$ dislocations with unit: $1 \times 10^{14} \text{ m}^{-2}$; ratio: $\rho_{basal \langle a \rangle} / \rho_{total}$ and $\rho_{non-basal \langle a \rangle} / \rho_{total}$, in brackets)

Dislocation density	at 100°C					
	0%	2%	5%	10%	15%	20%
ρ_{total}	2.54±0.04	3.28±0.05	4.78±0.08	5.70±0.08	6.20±0.10	6.61±0.11
$\rho_{\langle a \rangle}$	1.87±0.15	2.42±0.17	3.52±0.16	4.05±0.15	4.40±0.15	4.69±0.15
$\rho_{\langle c \rangle}$	0.27±0.02	0.36±0.03	0.24±0.01	0.24±0.01	0.23±0.01	0.22±0.01
$\rho_{\langle c+a \rangle}$	0.40±0.04	0.50±0.04	1.01±0.04	1.41±0.05	1.57±0.05	1.70±0.05
$\rho_{basal \langle a \rangle}$ (ratio)	0.48 (0.19)	0.59 (0.18)	0.53 (0.11)	0.39 (0.07)	0.42 (0.07)	0.35 (0.05)
$\rho_{nonbasal \langle a \rangle}$ (ratio)	0.95 (0.37)	1.44 (0.44)	2.86 (0.60)	3.61 (0.63)	3.98 (0.64)	4.34 (0.06)

Dislocation density	at 100°C					
	0%	2%	5%	10%	15%	20%
ρ_{total}	2.68±0.04	3.42±0.07	4.14±0.10	4.62±0.06	4.99±0.05	5.31±0.05
$\rho_{\langle a \rangle}$	1.83±0.09	2.49±0.14	2.82±0.12	3.19±0.15	3.48±0.15	3.64±0.12
$\rho_{\langle c \rangle}$	0.13±0.01	0.27±0.02	0.18±0.01	0.23±0.01	0.23±0.01	0.21±0.01
$\rho_{\langle c+a \rangle}$	0.72±0.03	0.66±0.03	1.14±0.05	1.20±0.05	1.28±0.05	1.46±0.05
$\rho_{basal \langle a \rangle}$ (ratio)	0.26 (0.10)	0.52 (0.15)	0.36 (0.09)	0.46 (0.10)	0.48 (0.10)	0.33 (0.06)
$\rho_{nonbasal \langle a \rangle}$ (ratio)	1.45 (0.54)	1.68 (0.49)	2.37 (0.57)	2.60 (0.56)	2.90 (0.58)	3.31 (0.62)

Dislocation density	at 200°C					
	0%	2%	5%	10%	15%	20%
ρ_{total}	3.35±0.07	3.38±0.09	3.80±0.08	4.31±0.12	5.03±0.15	4.97±0.11
$\rho_{\langle a \rangle}$	2.49±0.15	2.42±0.13	2.62±0.09	2.84±0.03	3.50±0.00	3.52±0.11
$\rho_{\langle c \rangle}$	0.32±0.03	0.27±0.02	0.15±0.01	0.11±0.00	0.08±0.00	0.17±0.01
$\rho_{\langle c+a \rangle}$	0.53±0.03	0.69±0.04	1.03±0.04	1.36±0.02	1.45±0.01	1.27±0.04
$\rho_{basal \langle a \rangle}$	0.52 (0.16)	0.48 (0.14)	0.24 (0.06)	0.00 (0.00)	0.00 (0.00)	0.21 (0.04)
$\rho_{nonbasal \langle a \rangle}$	1.59 (0.48)	1.65 (0.49)	2.38 (0.63)	2.84 (0.66)	3.50 (0.70)	3.31 (0.67)

Table. A.8 Overall dislocation densities and densities based on the $\langle a \rangle$, $\langle c \rangle$, and $\langle c+a \rangle$ dislocations, obtained from CMWP analysis as a function of the strain along the RD at RT, 100°C, and 200°C in ZX10 (ρ_{total} : overall dislocation, $\rho_{\langle a \rangle}$: $\langle a \rangle$ dislocation, $\rho_{\langle c \rangle}$: $\langle c \rangle$ dislocation, and $\rho_{\langle c+a \rangle}$: $\langle c+a \rangle$ dislocation densities, $\rho_{basal \langle a \rangle}$ and $\rho_{non-basal \langle a \rangle}$: ratio of basal $\langle a \rangle$ and non-basal $\langle a \rangle$ dislocations with unit: $1 \times 10^{14} \text{ m}^{-2}$; ratio: $\rho_{basal \langle a \rangle} / \rho_{total}$ and $\rho_{non-basal \langle a \rangle} / \rho_{total}$, in brackets)

Dislocation density	at RT					
	0%	2%	5%	10%	15%	20%
ρ_{total}	2.53±0.04	3.16±0.06	4.71±0.09	5.76±0.09	6.38±0.10	6.84±0.07
$\rho_{\langle a \rangle}$	1.86±0.16	2.27±0.14	3.34±0.15	4.00±0.14	4.44±0.16	4.79±0.17
$\rho_{\langle c \rangle}$	0.28±0.02	0.30±0.02	0.22±0.01	0.24±0.01	0.27±0.01	0.30±0.01
$\rho_{\langle c+a \rangle}$	0.38±0.04	0.59±0.03	1.15±0.05	1.52±0.05	1.67±0.06	1.75±0.07
$\rho_{basal \langle a \rangle}$ (ratio)	0.49 (0.19)	0.50 (0.16)	0.46 (0.10)	0.34 (0.06)	0.38 (0.06)	0.46 (0.07)
$\rho_{nonbasal \langle a \rangle}$ (ratio)	0.92 (0.36)	1.44 (0.45)	2.75 (0.58)	3.58 (0.62)	3.98 (0.62)	4.27 (0.62)

Dislocation density	at 100°C					
	0%	2%	5%	10%	15%	20%
ρ_{total}	2.45±0.04	3.11±0.09	4.11±0.05	4.99±0.05	5.55±0.07	6.00±0.06
$\rho_{\langle a \rangle}$	1.72±0.09	2.25±0.13	2.90±0.14	3.57±0.17	3.92±0.15	4.18±0.14
$\rho_{\langle c \rangle}$	0.17±0.01	0.26±0.02	0.26±0.01	0.27±0.01	0.24±0.01	0.25±0.01
$\rho_{\langle c+a \rangle}$	0.56±0.03	0.59±0.03	0.95±0.05	1.15±0.05	1.40±0.06	1.57±0.05
$\rho_{basal \langle a \rangle}$ (ratio)	0.33 (0.13)	0.48 (0.15)	0.50 (0.12)	0.56 (0.11)	0.43 (0.08)	0.38 (0.06)
$\rho_{nonbasal \langle a \rangle}$ (ratio)	1.24 (0.50)	1.48 (0.48)	2.19 (0.53)	2.85 (0.57)	3.45 (0.62)	3.80 (0.63)

Dislocation density	at 200°C					
	0%	2%	5%	10%	15%	20%
ρ_{total}	3.08±0.07	3.11±0.08	3.92±0.12	4.66±0.09	5.00±0.07	5.31±0.05
$\rho_{\langle a \rangle}$	2.23±0.11	2.09±0.10	2.70±0.10	3.21±0.11	3.55±0.12	3.67±0.00
$\rho_{\langle c \rangle}$	0.22±0.01	0.14±0.01	0.18±0.01	0.18±0.01	0.21±0.01	0.10±0.00
$\rho_{\langle c+a \rangle}$	0.62±0.03	0.87±0.04	1.05±0.04	1.27±0.05	1.24±0.05	1.59±0.01
$\rho_{basal \langle a \rangle}$	0.42 (0.13)	0.31 (0.10)	0.32 (0.08)	0.28 (0.06)	0.35 (0.07)	0.00 (0.00)
$\rho_{nonbasal \langle a \rangle}$	1.62 (0.53)	1.70 (0.55)	2.34 (0.60)	2.88 (0.62)	3.20 (0.64)	3.67 (0.69)

Curriculum Vitae

Personal information

Surname, name: Ha, Changwan
Date of birth: 24. Nov. 1987
Place of birth: Daegu, Republic of Korea
Marital status: Matrimony since 23. Feb. 2014, 1 Kind
Nationality: Republic of Korea
Address: Hansastr. 1,
21502 Geesthacht
E-mail: chagwan.ha@hereon.de / hacwan@naver.com /
hacwan@gmail.com

Academic Qualifications

03/2006 – 02/2012 Bachelor of Science (Bachelor degree)
Advanced Materials and system engineering
Kumoh National Institute of Technology
02/2007 – 01/2009 Military service in the Republic of Korea as a soldier
03/2012 – 02/2014 Master of Engineering (Master degree)
Advanced Materials Science and Engineering
Kumoh National Institute of Technology
Since 06/2015 Ph.D. student
Wrought Magnesium Alloys, Helmholtz-Zentrum Geesthacht,
registered in 2018 at the Institute of Materials Science and
Engineering, Clausthal University of Technology, Germany

Work experiences

03/2012 – 02/2014 Assistant lecture at Advanced Materials and system
engineering, Kumoh National Institute of Technology
- Mechanical testing
- Microstructure characterization
- X-ray diffractometer analysis
07/2013 – 08/2013 Internship at Wrought Magnesium Alloys, Helmholtz-Zentrum
Geesthacht, Germany
Since 06/2015 Research assistant at Wrought Magnesium Alloys, Helmholtz-
Zentrum Geesthacht, Germany

Publication list during doctoral study

Publications

- C. Ha, S. Yi, J. Bohlen, X. Zhou, H.-G. Brokmeier, N. Schell, and D. Letzig, Influence of deformation and recrystallization mechanisms on the microstructure and texture development of new magnesium sheet alloys, **Annual DESY report**, 2015.
- C. Ha, S. Yi, J. Bohlen, X. Zhou, H.-G. Brokmeier, N. Schell, and D. Letzig, Elastic lattice strain investigation of Magnesium alloy by in situ tensile loading, **Annual DESY report**, 2015.
- C. Ha, S. Yi, J. Bohlen, X. Zhou, H.-G. Brokmeier, N. Schell, and D. Letzig, Alloying influence on the activity of deformation mechanisms on the texture development of rolled Mg sheets at elevated temperatures, **Annual DESY report**, 2016.
- C. Ha, S. Yi, J. Bohlen, X. Zhou, H.-G. Brokmeier, N. Schell, and D. Letzig, Recrystallization effects on the microstructure and texture development of magnesium alloys with rare-earth elements or calcium, **Annual DESY report**, 2017.
- C. Ha, S. Yi, J. Bohlen, X. Zhou, H.-G. Brokmeier, N. Schell, D. Letzig, and K. U. Kainer, Deformation and Recrystallization Mechanisms and Their Influence on the Microstructure Development of Rare Earth Containing Magnesium Sheets, **Magnesium Technology 2018, The minerals, Metals & Materials Series**, 2018, 209-216
- C. Ha, S. Yi, J. Bohlen, X. Zhou, H.-G. Brokmeier, N. Schell, D. Letzig, and K. U. Kainer, Study of deformation mechanisms in Mg-Zn-Nd alloys by using *in-situ* synchrotron diffraction, **Magnesium 2018, Proceedings of the 11th International Conference on Magnesium Alloys and Their Applications**, 2018, 214-219
- Changwan Ha, Jan Bohlen, Sangbong Yi, Xiaohua Zhou, Heinz-Günter Brokmeier, Norbert Schell, Dietmar Letzig, Karl Ulrich Kainer, Influence of Nd or Ca addition on the dislocation activity and texture changes of Mg-Zn alloy sheets under uniaxial tensile loading, **Materials Science & Engineering A 761**, 2019, 138053
- Xiaohua Zhou, Changwan Ha, Sangbong Yi, Jan Bohlen, Norbert Schell, Yuanqing Chi, Mingyi Zheng, and Heinz-Günter Brokmeier, Texture and Lattice Strain Evolution during Tensile Loading of Mg-Zn Alloys Measured by Synchrotron Diffraction, **Metals**, 2020, 10, 124, 1-15

- C. Ha, J. Bohlen, X. Zhou, H.-G. Brokmeier, K. U. Kainer, N. Schell, D. Letzig, and S. Yi, Texture development and dislocation activities in Mg-Nd and Mg-Ca alloy sheets, **Materials Characterization** **175**, 2021, 111044

Oral presentations

- C. Ha, S. Yi, J. Bohlen, D. Letzig, K. U. Kainer, X. Zhou, H.-G. Brokmeier, Effect of Microstructure, Texture and Dislocation Density on the Deformation and Recrystallization behavior of Mg-RE alloys, **Summer School “Utilization of advanced characterization methods of tailoring the properties of lightweight materials”**, Mar. 28–29, 2017, Charles University, Prague (Oral presentation, speaker)
- X. Zhou, C. Ha, S. Yi, J. Bohlen, B. Schwebke, Z. Zhong, N. Schell, and H.-G. Brokmeier, Texture and lattice strain evolution of Mg ZN202 during tension at RT, 100°C and 200°C by *in-situ* synchrotron diffraction, **6th International Conference on Magnesium**, Sep. 23–26, 2017, Shenyang, China (Oral presented by colleague)
- C. Ha, S. Yi, J. Bohlen, X. Zhou, H.-G. Brokmeier, N. Schell, D. Letzig, and K. U. Kainer, Deformation and Recrystallization Mechanisms and their Influence on the Microstructure Development of Rare Earth Containing Magnesium Sheets, **TMS 2018 147th Annual Meeting & Exhibition**, Mar. 11–15, 2018, Phoenix Convention Center, Arizona, USA (Oral presentation, speaker)
- C. Ha, S. Yi, J. Bohlen, X. Zhou, H.-G. Brokmeier, N. Schell, D. Letzig, K. U. Kainer, Study of deformation mechanisms in Mg-Zn-Nd alloys by using *in-situ* synchrotron diffraction method, **Mg 2018 the 11th International Conference on Magnesium Alloys and Their Applications**, Jul. 24–27, 2018, Beaumont Estate, Old Windsor, UK (Oral presentation, speaker)
- C. Ha, S. Yi, J. Bohlen, X. Zhou, H.-G. Brokmeier, N. Schell, D. Letzig, K. U. Kainer, The effect of Nd and Ca addition on dislocation activity and texture development in Mg-Zn alloy sheets, **Annual Texture Symposium of DGM-SF2M**, Mar. 28–29, 2019, Heinz Maier-Leibnitz Zentrum, Garching, Germany (Oral presentation, speaker)
- X. Zhou, C. Ha, S. Yi, J. Bohlen, N. Schell, H.-G. Brokmeier, Texture and lattice strain development of ZK10 and ZN10 studied by *in-situ* synchrotron diffraction at RT,

100°C and 200°C, **Annual Texture Symposium of DGM-SF2M**, Mar. 28–29, 2019, Heinz Maier-Leibnitz Zentrum, Garching, Germany (Oral presented by a colleague)

- S. Yi, X. Zeng, C. Ha, S. Jo, J. Bohlen, K.U. Kainer, D. Letzig, Deformation mechanisms and grain growth during recrystallization of Mg sheet alloys containing rare earth elements, **9th International Light Metals Technology Conference**, October, 15–18, 2019, Shanghai, China (Oral presented by a colleague)
- C. Ha, J. Bohlen, X. Zhou, H.-G. Brokmeier, K. U. Kainer, N. Schell, D. Letzig, S. Yi, Texture developments and dislocation activities in rolled Mg sheet alloys containing Zn and Nd, **Mg 2021 the 12th International Conference on Magnesium Alloys and Their Applications**, Jun. 15–18, 2021, Virtual Event (due to COVID-19)

Poster presentations

- C. Ha, S. Yi, J. Bohlen, X. Zhou, H.-G. Brokmeier, B. Schwebke, Z. Zhong, and N. Schell, Texture and lattice strain development during tensile testing of a ZE20 Mg alloy plate, **DESY Photon Science Users' Meeting 2016**, Jan. 27–29, 2016, DESY at Hamburg, Germany (Poster presentation, speaker)
- X. Zhou, C. Ha, S. Yi, J. Bohlen, B. Schwebke, Z. Zhong, N. Schell, and H.-G. Brokmeier, *In-situ* investigation of texture and dislocation evolution of magnesium alloy ZE21 under tensile load, **DESY Photon Science Users' Meeting 2016**, Jan. 27–29, 2016, DESY at Hamburg, Germany (Poster presented by a colleague)
- C. Ha, S. Yi, J. Bohlen, D. Letzig, K.U. Kainer, X. Zhou, and H.-G. Brokmeier, The Influence of deformation and recrystallization mechanisms on the development of microstructure and mechanical properties during rolling of Mg-RE alloys, **1st Symposium of Zentrum für Hochleistungsmaterialien (ZHM) Graduate School**, Nov. 17–18, 2016, Hamburg University of Technology, Germany (Poster presentation, speaker)
- C. Ha, S. Yi, J. Bohlen, D. Letzig, K. U. Kainer, X. Zhou, and H.-G. Brokmeier, N. Schell, The Influence of Deformation and Recrystallization Mechanisms on the Development of Microstructure and Mechanical Properties during Rolling of Mg- RE Alloys, **DESY Photon Science Users' Meeting 2017**, Jan. 26–27, 2017, DESY at Hamburg, Germany (Poster presentation, speaker)

- X. Zhou, C. Ha, S. Yi, J. Bohlen, B. Schwebke, Z. Zhong, N. Schell, and H.-G. Brokmeier, Texture and defect density evolution of Mg-ZN202 during high temperature deformation by *in-situ* synchrotron diffraction, **DESY Photon Science Users' Meeting 2017**, Jan. 26–27, 2017, DESY at Hamburg, Germany (Poster presented by colleague)
- C. Ha, S. Yi, J. Bohlen, X. Zhou, H.-G. Brokmeier, N. Schell, D. Letzig, and K. U. Kainer, Deformation and Recrystallization Mechanisms of Mg-RE alloy, **2nd Symposium of Zentrum für Hochleistungsmaterialien (ZHM) Graduate School**, Nov. 30–Dec. 1, 2017, Hamburg University of Technology, Germany (Poster presentation, speaker)
- C. Ha, S. Yi, J. Bohlen, X. Zhou, H.-G. Brokmeier, N. Schell, D. Letzig, and K.U. Kainer, Influence of the addition of Nd and Ca on deformation mechanisms in Mg-Zn alloys, **XXVII International Materials Research Congress (IMRC 2018)**, Aug. 19–24, 2018, Cancun, Mexico (Poster presented by colleague)

